High Pressure Isotropic Compression and Grain Crushing of Coarse Granular Materials

by

JOON SOO PARK

B.S., Inha University, 2015

A thesis submitted to the
Faculty of the Graduate School of the
University of Colorado in partial fulfillment
of the requirement for the degree of
Master of Science
Department of Civil, Environmental and Architectural Engineering
2018

This thesis entitled:

High Pressure Isotropic Compression and

Grain Crushing of Coarse Granular Materials

Written by Joon Soo Park

Has been approved for the Civil, Environmental, and Architectural Engineering

_____

Assistant Professor Yida Zhang (committee chair)

_____

Assistant Professor Shideh Dashti

_____

Professor Dobroslav Znidarcic

Date _____

The final copy of this thesis has been examined by the signatories, and we find that both the content and the form meet the acceptable presentation standards of scholarly work in the above mentioned discipline.

Park, Joon Soo (M.S., Civil Engineering, Department of Civil, Environmental and Architectural Engineering)

High Pressure Isotropic Compression and Grain Crushing of Coarse Granular Materials

Thesis directed by Professor Yida Zhang

ABSTRACT

The effect of grain crushing and grain size on the evolution of water retention curve is investigated based on the framework of Unsaturated Breakage Mechanics (UBM) (Buscarnera & Einav, 2012). The previous study by Gao et al. (2016) have been complemented by additional compression and soil water retention data on two types of granular soils with coarser and finer initial gradings than the ones presented in Gao et al. (2016). The model satisfactorily captures the co-evolution of suction air-entry value (s_{AEV}) and the degree of grain breakage during compression. In addition, this study revealed that the effect of grain shape and pre-yielding void collapse are necessary components for future enhancement of the breakage mechanics model.

The compressive and breakage response of coarse granular materials are further investigated using the High Pressure Isotropic Compression (HPIC) device (Mun & McCartney., 2017). This thesis introduces several troubleshooting attempts of the HPIC device and the developed protocols to conduct high-pressure crushing tests. Coarse quartz sand and crushed shale sand are subjected to the high pressure isotropic compression test under dry and saturated states. Differences between the two materials in the compression curve are observed and the possible reasons are discussed. The compression tests are stopped at various stress levels to allow for inspections on the grain size distribution (GSD). Based on these measures, the degree of grain breakage is quantified via Einav's breakage index (Einav, 2007). A clear increase on

grain breakage at elevated stress states and the evolution towards an ultimate fractal state is clearly observed. The obtained results are interpreted using a new 1D breakage model to serve as the basis of the next-generation breakage mechanics models.

ACKNOWLEDGEMENTS

I would like to express my sincere gratitude to my advisor, professor Yida Zhang, throughout my MS studies. He has been always willing to support and guide me for this accomplishment, and I am grateful for all his contribution to my academic performance. I feel many improvements thanks to his advising in experimental matters, research ideas, presentation skills, and thesis writing. I want to express appreciation to Dr. Dobroslav Znidarcic and Dr. Shideh Dashiti, for serving as my committee members. I am also grateful to Dr. Woongju Mun for all his recommendations and advising in High Pressure Isotropic Compression. I respect him in that designing such precious device. I acknowledge Dragan Mejic and Derek Carpenter for their assist in troubleshooting and developing protocols against technical issues. Many thanks to my lab colleagues and classmates.

I would like to appreciate my father, mother and sister who have always been there for me during all of my life struggles. I cannot imagine me without their devotion in a life of studying abroad. I am grateful to my Korean friends at Boulder Korean Church. I could adapt myself to Boulder thanks to their help and I will never forget everything with them. I also thank my hang out friends. I have released my stress as having fun with them.

Finally, a big thanks to my lovely girlfriend Yunmi Gu for her endless love and encouragement. This thesis will not exist, without her support and trust to me. She is the real home of me.

TABLE OF CONTENTS

CHAPTER 1: INTRODCUCTION 1

1.1. Research Objectives 1

1.1.1. Objective 1 1

1.1.2. Objective 2 1

1.1.3. Objective 3 2

1.2. Motivation 2

1.3. Arrangement of the thesis 7

CHAPTER 2: BACKGROUND 8

2.1. Breakage Mechanics (Einav, 2007) 8

2.2. Unsaturated Breakage Mechanics (G. Buscarnera & I. Einav, 2012) 9

2.2.1. The Helmholtz free energy for unsaturated granular materials 10

2.2.2. Dissipation rate function, yield surface and inelastic flow rules 12

2.2.3. Elastic and SWRC relations 13

2.2.4. The hydromechanics of breakage 15

2.3. Grainsize dependence of clastic yielding (Zhang and Buscarnera, 2014) 15

2.4. Evolution of the SWRC Subjected to Grain Crushing (Gao et al. 2016) 17

2.5. Compression of Unsaturated Clay under High Stresses (Mun and McCartney, 2015) .. 19

2.6. Roles of Particle Breakage on the Isotropic Compression of Sand (Mun and McCartney, 2017) 21

2.6.1. Isotropic Compression Response of Dry and Saturated Sand 22

2.6.2. Particle Breakage during Isotropic Compression 22

2.7. Summary 24

CHAPTER 3: VALIDATION OF UBM USING ADDITIONAL DATA 26

3.1. Experimental Program 26
3.1.1. Testing materials 26
3.1.2. Testing Program 27
3.1.3. Testing results 28
3.2. UBM Interpretation 31
3.3. Grainsize effect on hydromechanical coupling 36
CHAPTER 4: EXPERIMENTAL SETUP AND TESTING APPROACH 38
4.1. High Pressure Isotropic Compression Device 38
4.2. System Calibration 42
CHAPTER 5: TROUBLESHOOTING AND PROTOCOL DEVELOPMENT 44
5.1. Attempts for coupled HPIC and SWRC tests 44
5.1.1. Original plan of the experimental study 44
5.1.2. Limitations of SWRC test using HPIC 44
5.2. New plan of the study 47
5.3. Troubleshooting on DPT and DAQ system for measuring water outflow 51
5.4. Failure of the bolts connecting the isotropic cell and its top plate 53
CHAPTER 6: EXPERIMENTAL RESULTS 56
6.1. Details of specimens and experimental works 56
6.2. Compression curve 58
6.2.1. Compression curve for dry quartz sand under the different stress 58
6.2.2. Comparison between quartz sand and shale under dry and saturated condition 60
6.3. The grain size distribution of crushed specimens 63
CHAPTER 7: 1D BREAKAGE MODEL USING THE NEW BREAKAGE EVOLUTION LAW 67

7.1. The modified breakage evolution law 67
7.2. Parametric study 68
7.3. A linear elastic 1D compression model based on the new breakage law 69
7.4. Breakage evolution law in pressure-dependent (PD) elasticity 73
CHAPTER 8: CONCLUSION 76
REFERENCE 78

LIST OF TABLES

Table 3.1: Characteristic values of GSD and SWRC.....30
Table 3.2: Parameters of UBM.....32
Table 4.1: Details of the syringe pump.....41
Table 5.1: Mechanical properties of the screws by composition.....54
Table 6.1: Index properties of specimens 57
Table 6.2: Parameters of grain size distribution.....64
Table 7.1: Parameters for best-matched prediction with linear elasticity model.....72
Table 7.2: Parameters for best-matched prediction with PD model.....75

LIST OF FIGURES

Figure 1.1: Industry application in the research topic:(a) Pile installation on sand; (b) Enhanced oil recovery system; (c) Railway Ballast; (d) Landslide; (e) Extraction of shale gas and oil; (f) Enhanced Geothermal System 3

Figure 1.2: Particle breakage during installation of displacement piles (figures modified from Yang et al., 2010) 4

Figure 1.3: Schematics of the working mechanism of proppants 6

Figure 1.4: Schematics of the occurrence of sliding surface liquefaction [Wang et al., 2003] 6

Figure 2.1: (a) Definition of Einav's breakage index B; (b) Integrate the area associated with $Bp, Bt, and\ B$ 8

Figure 2.2: The grainsize dependence on the two model parameters: (a) The grainsize dependence on K_w; (b) The grainsize dependence on E_c 16

Figure 2.3: Predicted dependence of capillary toughness number on mean grainsize 16

Figure 2.4: Comparison between experimental data and UBM prediction data for sand typed soil and glass beads: (a and b) compression curve; (d and e) GSD; (f and g) SWRC. After Gao et al. (2016) 18

Figure 2.5: Undrained compression curves of clay specimens with different initial degrees of saturation 19

Figure 2.6: Change of mean effective stress and water outflow in time of clay specimen with different initial degree of saturation during drained compression: (a) $S_r = 1.0$; (b) $S_r = 0.9$; (c) $S_r = 0.8$ 20

Figure 2.7: Comparison of changes between total volume of specimen and water outflow according to mean effective stress for the specimens with different initial degrees of saturation: (a) $S_r = 1$; (b) $S_r = 0.9$; (c) $S_r = 0.8$ 21

Figure 2.8: Compression curves of clay specimen: (a) $e - logp'$; (b) $e - p'$ 21

Figure 2.9: Isotropic compression curves of the sand specimen with different drainage condition: (a) $e - logp'$ (Dry sand in drainage); (b) $e - p'$ (Dry sand in drainage); (c) $e - logp'$ (Dry sand in no drainage); (d) $e - p'$ (Dry sand in no drainage); (e) $e - logp'$ (Saturated sand in no drainage); (f) $e - p'$ (Saturated sand in no drainage) 23

Figure 2.10: Particle size distribution of Mason sand for all the stress levels: (a) drained dry sand; (b) undrained dry sand; (c) undrained saturated sand 23

Figure 2.11: Dependence of initial relative density: (a) compression curves; (b) particle size distribution after isotropic drained compression test under 160 MPa 24

Figure 3.1: GSD of the tested sand and glass bead specimens 26

Figure 3.2: Images of the particles of the testing materials: (a)-(c) sand, (d)-(f) glass beads 27

Figure 3.3: Compression curves for (a) sand and (b) glass beads 28

Figure 3.4: GSDs for (a) coarse sand; (b) fine sand; (c) large GB; (d) small GB 29

Figure 3.5: SWRCs for (a) coarse sand; (b) fine sand; (c) large GB; (d) small GB. The dashed line and open square in (a) and (c) indicate an extrapolation of the curve within a suction rage beyond the resolution of the equipment 30

Figure 3.6: Comparison between measured data and UBM predictions for (a) coarse sand; (b) fine sand; (c) large GB; (d) small GB 33

Figure 3.7: Performance of UBM after adjusting the mechanical parameters to match the GSD data of coarse sand 35

Figure 3.8: Grain size effect on the value of (a) air-entry parameter Kw and (b) critical breakage energy Ec. 36

Figure 3.9: Grain size effect on the intensity of hydromechanical coupling. 37

Figure 4.1: Picture view of HPIC 39

Figure 4.2: Schematic view of HPIC 39

Figure 4.3: Picture view of syringe pump 40

Figure 4.4: Picture of pressure control panel 40

Figure 4.5: Toolkit 40

Figure 4.6: (a) Inside view of isotropic cell; (b) Outside view of isotropic cell 41

Figure 4.7: (a) View of the bottom plate; (b) Inside view of the bottom plate 42

Figure 4.8: Aluminum specimen 43

Figure 4.9: Machine compliance curve 43

Figure 5.1: Experimental setup for SWRC test with HPIC: (a) Sketch of the test; (b) picture of the bottom plate 45

Figure 5.2: (a) View of Tempe cell; (b) Operation of Tempe cell test 45

Figure 5.3: SWRC test results by (a) Tempe cell; (b) HPIC 46

Figure 5.4: A schematic view of flow direction of air pressure and water drainage: (a) HPIC; (b) Tempe cell 47

Figure 5.5: (a) Initial setting of bottom plate; (b) Current setting of bottom plate 48

Figure 5.6: Initial sample setting 49

Figure 5.7: Setting with neoprene membrane 49

Figure 5.8: Procedure of sample preparation in order from left to right 50

Figure 5.9: Determined setting for sample preparation: (a) View from side; (b) View from above 51

Figure 5.10: DPT debugging 52

Figure 5.11: Composition of DAQ system 52

Figure 5.12: Data acquisition system troubleshooting: (a) connected with DPT; (b) disconnected with DPT 53

Figure 5.13: Composition of the HPIC cover: (a) Load Frame; (b) Top plate; (c) Isotropic cell. 53
Figure 5.14: Socket head screws for load frame (above) and for isotropic cell (below) 54
Figure 5.15: Schematic view of load transition for screw failure 55
Figure 6.1: Microscopic view of the (a) quartz sand; (b) shale sand 56
Figure 6.2: Pictures of the (a) quartz sand; (b) shale sand 56
Figure 6.3: Compression curve for dry quartz sand at the different stress levels: (a) 20 MPa; (b) 80 MPa; (c) 160 MPa; (d) Integrated plot of the curves 59
Figure 6.4: The compression curves of shale sand and quartz sand with the different saturated condition: (a) quartz sand; (b) shale sand 61
Figure 6.5: Comparison of normalized relaxation on the saturated shale sand and dry shale sand: (a) at the 1st refill time along with the one of dry quartz sand and machine compliance test; (b) at the 2nd refill time; (c) at the 3rd refill time 62
Figure 6.6: Grain size distribution of the quartz sand specimens after compression test under the different stress: (a) Dried quartz sand under 20, 40, 80, and 160 MPa; (b) Dried and saturated quartz sand under 160 MPa 64
Figure 6.7: Initial, ultimate, and current grain size distribution for the specimens under different crushing stress: (a) 20 MPa; (b) 40 MPa; (c) 80 MPa; (d) 160 MPa 65
Figure 6.8: (a) GSD by calibration; (b) Breakage evolution curve by experiment 65
Figure 6.9: Picture of shale sand specimen after high pressure compression under 160 MPa: (a) Dried specimen; (b) Saturated specimen 66
Figure 7.1: Parametric study: (a) shape factor n; (b) critical breakage energy Ec 69
Figure 7.2: Prediction by linear elasticity model: (a) Compression curve; (b) Breakage evolution curve; (c) Total strain – Breakage degree; (d) Stress – strain (Total, Elastic and plastic strain).. 72
Figure 7.3: Parametric study of linear elasticity model:(a) for critical breakage energy; (b) for stiffness 73
Figure 7.4: Prediction results by PD model: (a) compression curve; (b) Breakage evolution curve; (c) Total strain – Breakage degree; (d) Stress – strain (Total, Elastic and plastic strain).. 75

LIST OF NOTATIONS AND ABBREVIATIONS

LATIN SYMBOLS

a: constant for controlling the slope of the SWRC

B: breakage index

B_p, B_t: potential breakage and total breakage

C, A, P: circularity index, area and perimeter of sand particles

C_u, C_c: coefficient of uniformity and curvature on the GSD, respectively

D_{10}, D_{50}, D_{60}: grain sizes correspond to 10%, 50%, 60% pass by mass on the GSD, respectively

D_m, D_M: minimum and maximum grain size

D_r: reference grain size

e: void ratio

E_B: breakage energy

E_c: critical breakage energy

E_c^*: critical breakage energy for the breakage evolution law

F, F_0, F_u: current, initial and ultimate cumulative GSD

$\mathrm{g}, \mathrm{g}_0, \mathrm{g}_u$: current, initial and ultimate probability GSD

G: shear modulus

G_s: specific gravity

K: bulk modulus

K_w: retention curve parameter associated with the suction air entry value

$\bar{K}$, $\bar{G}$: non-dimensional bulk and shear elastic constants

m: pressure dependence coefficient for elastic modulus

M: the slope of critical state line in p-q space

n: shape factor

N_r: normalized relaxation

p: stress or pressure

p_r: reference stress

$\bar{p}$: pressure in dissipative space

q: shear stress

s: suction

s_{AEV}: suction air entry value

S_r: degree of saturation

S_{re}: residual degree of saturation

u_a, u_w: air and water pressure

W: rate of work input

$y, \bar{y}$: breakage yield function in true stress and dissipative stress space, respectively

GREEK SYMBOLS

α, β: fractal dimensions

d: particle size

ε: rate of total strain

ω: plastic-breakage coupling angle

Φ: rate of energy dissipation

ψ, ψ_r: specific grain size Helmholtz free energy and a reference value

Ψ: total Helmholtz free energy

σ': effective stress

ϑ_M, ϑ_H: mechanical and hydraulic grading indices

ξ_{CT}: capillary toughness number

ABBREVIATIONS

AP: Arya Paris model

DAQ: data acquisition system

DEM: Discrete Element Method

DPT: differential pressure transducer

GB: glass beads

GSD: grain size distribution

HPIC: High Pressure Isotropic Compression device

LCC: limiting compression curve

MK: modified Kovacs model

PD: pressure-dependent

SWRC: soil water retention curve

UBM: unsaturated breakage mechanics

CHAPTER 1: INTRODCUCTION

1.1. Research Objectives

This thesis presents the experimental preparation and theoretical investigation of the compressive response of coarse granular materials in high pressure regime. The goal of this project is to: a) investigate the evolution of soil water retention curves of granular soils during grain breakage; b) troubleshoot the High Pressure Isotropic Compression device (HPIC) in controlling suction and develop testing protocols for crushable granular materials; c) study the coupling between compression and grain breakage at various stress levels and saturation conditions for different types of sand. The specific objectives are summarized below.

1.1.1. Objective 1

Objective 1 is to review and validate a constitutive model named unsaturated breakage mechanics (UBM) to investigate the effect of grain crushing and grain size on the apparent soil water retention curves. The model is capable of capturing the coupled mechanical and hydraulic properties of brittle granular soils. The predictive performance of this model will be assessed using a previously produced experimental dataset.

1.1.2. Objective 2

Objective 2 is to study and summarize the experimental setup of with the High Pressure Isotropic Compression device. The detailed properties, functions and compositions of the device will be introduced. The existing problems of the device will be identified and documented. Troubleshooting will be attempted.

1.1.3. Objective 3

Objective 3 aims to produce a series of compression, grain size distribution, and breakage evolution curves of the tested materials at the different saturation conditions. For this purpose, high pressure isotropic compression tests and sieve analysis will be conducted. The results will be interpreted using a new one-dimensional (1D) breakage mechanics model to serve as the basis of a new breakage mechanics theory.

1.2. Motivation

Granular soils are ubiquitous in civil engineering projects, e.g. foundations on sands or gravels, rockfills embankments and railway ballasts (Oldecop and Alonso 2001; Indraratna et al., 2010; Yang et al., 2010). Continuous research effort has been made over the past century in characterizing and modeling their deformation behaviors to better engineer civil infrastructures. Recent research focuses on linking the macroscopic properties of granular soils, such as packing condition, critical state, failure, and deformability, with the microscale properties of their constituting grains, including their size, shape, mineralogy and crushability (Tapias et al., 2015; Ovalle et al., 2014; Cil and Alshibli, 2014; Hall et al., 2010; Andò et al., 2013; Zhang et al., 2016).

Under high pressures, grain crushing is the dominating micromechanism that controls the macroscopic mechanical response of granular soils. Such process alters the overall gradation and correspondingly changes the shear and volumetric behavior of the material (Lade et al., 1996; Nakata et al., 2001; Mcdowell, 2002). Grain breakage further changes the hydraulic properties of the soil matrix. As the gradation and porosity evolve during breakage-enhanced compaction, the soil water retention capacity of the soil skeleton is enhanced and its permeability is dramatically reduced (Gao et al., 2016; Esna Ashari et al., 2018). The coupling between the hydraulic-

mechanical-breakage processes is of great relevance to a wide range of geotechnical and geo-energy engineering problems involved in pile driving, railway construction, landslide, enhanced oil and gas recovery, and geothermal energy harvesting (Figure 1.1).

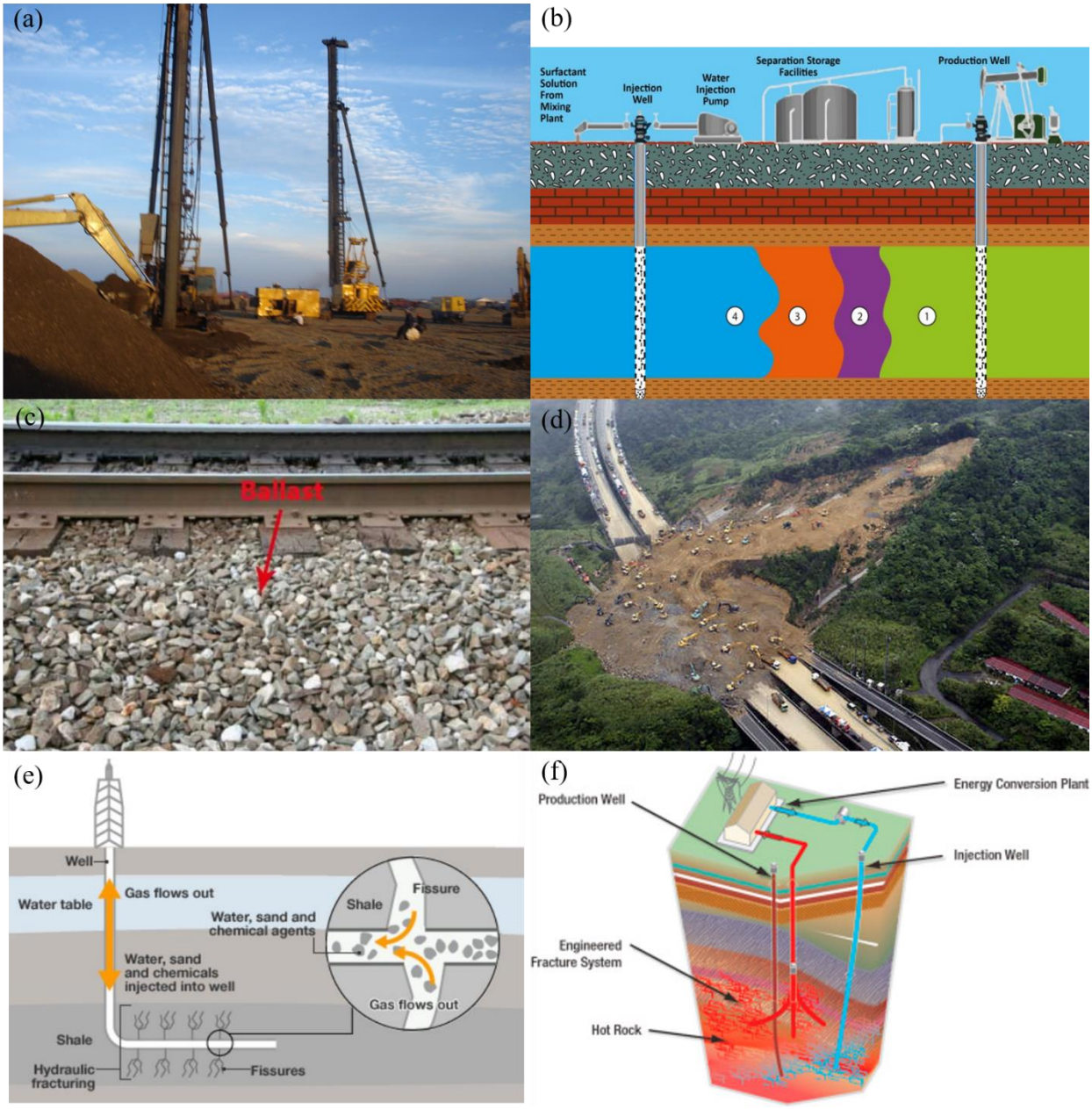

Figure 1.1: Industry application in the research topic:(a) Pile installation on sand; (b) Enhanced oil recovery system; (c) Railway Ballast; (d) Landslide; (e) Extraction of shale gas and oil; (f) Enhanced Geothermal System

For example, the capacity of driven pile in sand is developed as the pile displaces into the soils, which is governed by the mobilization of interfacial friction, localization of shear strain near the side of the pile, and grain fragmentation near the tip of the pile. Model experiment on displacement pile installation in quartz sand confirmed that significant particle breakage takes place surrounding the pile due to extreme normal and shear stresses (Yang et al. (2010) (Figure 1.2). The accumulation of grain crushing can fundamentally alter the pile axial capacity as well as its load-displacement behaviors. For instance, the resistance to penetration of well graded soils is higher than that of uniformly poorly graded soils due to its lower susceptibility to grain crushing, as observed from geotechnical centrifuge tests (McDowell and Bolton, 2000). Pile driving in highly crushable soils (e.g. carbonate sands) also requires much higher axial strain level to mobilize the same end bearing capacity compared to less crushable soils (e.g. silica Toyoura sand) (Kuwajima et al., 2009).

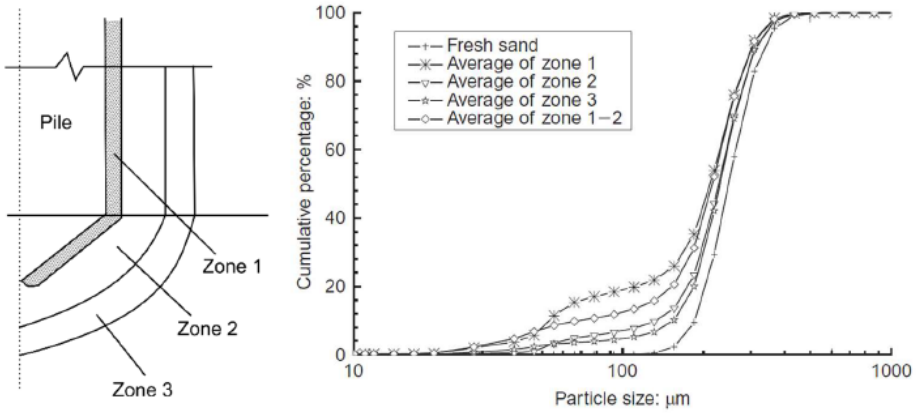

Figure 1.2: Particle breakage during installation of displacement piles (figures modified from Yang et al., 2010)

Particle breakage also occurs in the ballast layers of railway tracks. The layer consisted of large and angular particles is used to control stress distribution on subgrade, decrease vibration that causes the deterioration of track, and drain water during flooding. The wheel-load-developed cyclic vertical loading causes particle rearrangement, subsequent ballast degradation, and thus

track displacement (B. Indraratna et al., 2005; Lackenby et al., 2007). Additionally, the cyclic loading causes the accumulation of permanent volumetric strain which is highly affected by particle breakage. The induced track settlement and displacement have led to increasingly frequent maintenance cycle and this has been motivated to study particle breakage of ballast in the railway industry.

Another important application of this study is to assess the change of hydraulic conductivity of fractured rock formations encountered in shale gas and geothermal energy extractions. During fracking, proppants are delivered and installed into cracks by fracking fluid to hold the fracture network open after withdrawal of fluid pressure (Figure 1.3). Crushing of proppants can cause fracture closure and clogging of the pore spaces from the generated fines, undermine the overall conductivity of the fracture network, and eventually deteriorate the productivity of the wells. For these reasons, the crushing resistance is one of the key factors in optimizing proppant performance. Many studies have been conducted to assess the crushability of proppants under room temperature and notionally 'dry' conditions (Gaurav et al., 2012; Ingraham et al., 2015) and some procedures have been standardized (ISO13503-2, 2006). However, in-situ condition of proppants often involves elevated temperatures (typically 250-300 °F and can be as high as 550 °F, Raysoni and Weaver, 2013) and multiphase fluid flow (i.e. fluid mixtures of gas, water and oil). Many recent studies have highlighted the effect of diagenesis of proppant under such multiphysics perturbations (Raysoni and Weaver 2013; Ghosh et al. 2014.; Bremer et al. 2010). Similar applications can be also found in enhanced oil recovery projects, where the replacement of the in-situ fluid from oil to water may promote compaction and crushing of the granular rocks.

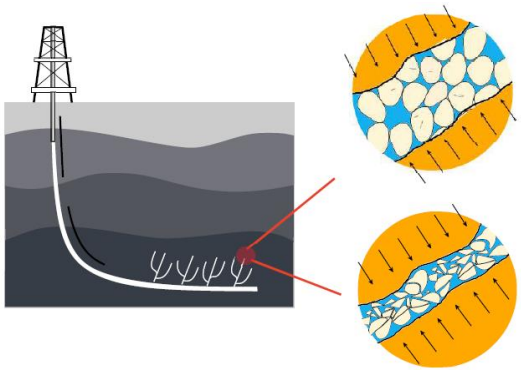

Figure 1.3: Schematics of the working mechanism of proppants

Finally, grain breakage can facilitate the development of excess pore-pressure at slip surface of landslides and modify the traveling characteristics of the mobilized mass. For instance, high mobility of the mobilized mass is observed in the Heigasei Landslide that took place in 1998 in the Fukushima Prefecture, Japan. Wang et al. (2003) attributed such phenomenon to the excess pore-pressure generated by grain crushing during landslide motion, based on the observation that the grain size distribution of soil specimens taken from the deposited debris contains much finer grains compared to those from source area. Further experimental studies on undrained ring-shear tests replicating the stress path of sliding surface showed that sliding motion (under normal stresses as low as 40 kPa) can lead to grain crushing along the surface, followed by liquefaction along the surface and finally to rapid movement accompanied by long runout distance (Wang et al., 2003; Sadrekarimi and Olson, 2010).

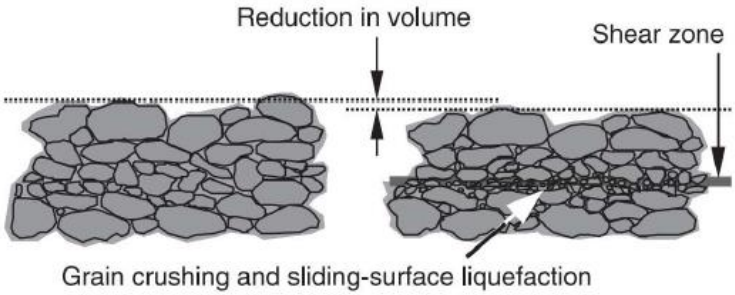

Figure 1.4: Schematics of the occurrence of sliding surface liquefaction [Wang et al., 2003]

1.3. Arrangement of the thesis

The thesis is organized into eight chapters. Chapter 1 states goals of the study and explains the motivations and potential applications of this research. Chapter 2 presents the literature review where the latest theoretical and experimental ideas on this topic are summarized. Chapter 3 validates an unsaturated breakage model against a set of unpublished experimental data. Chapter 4 introduces the High Pressure Isotropic Compression (HPIC) device, which is the major tool used in this study. Chapter 5 describes the encountered experimental issues with the HPIC. It summarizes the attempts of troubleshooting and describes the developed protocols for crushing test on coarse-grained sand. Chapter 6 collects the experimental results produced in this study, including the compression curves, grain size distributions, and breakage evolution curves of two types of materials. Chapter 7 introduces a 1D breakage model based on a new breakage mechanics theory to interpret the breakage evolution. Chapter 8 summarizes the main findings of this study.

CHAPTER 2: BACKGROUND

2.1. Breakage Mechanics (Einav, 2007)

Both strength and compressibility of granular soils are influenced by the process of grain crushing during uniform and deviatoric loading (Hardin, 1985). Many efforts have been devoted to quantifying the degree of particle breakage and link it with the stress-strain behaviors of granular soils (Lee and Farhoomand, 1967; Marsal, 1973; Hardin, 1985; Lade et al., 1996; Einav, 2007). The breakage theory (Einav, 2007) introduces a concept of relative breakage to evaluate the degree of particle breakage during the course of loading. The relative breakage is obtained by evaluating relative proximity of the current cumulative distribution from (a) initial cumulative distribution and (b) an ultimate cumulative distribution as shown in the Figure 2.1 (a). Consequently, the relative breakage is defined by three cumulative grain size distributions (GSD) functions: the current GSD 'F', the initial GSD 'F_0', and the ultimate GSD 'F_u'.

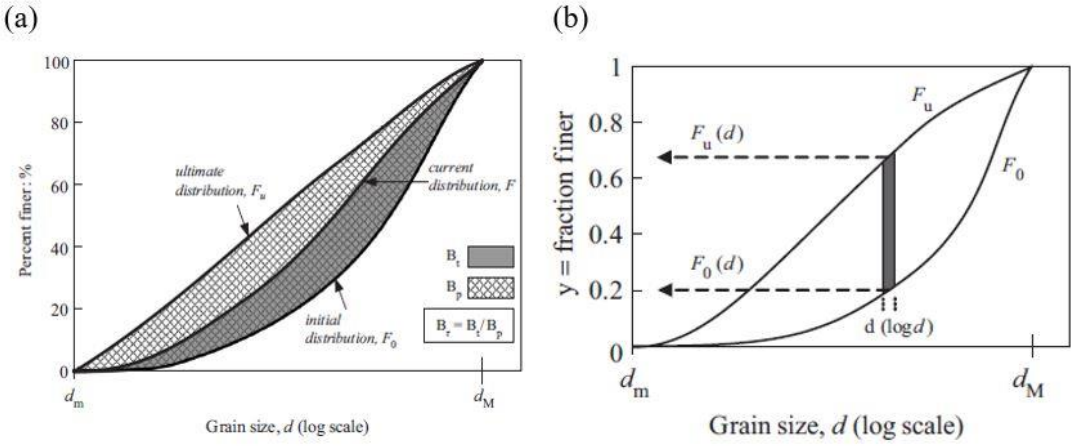

Figure 2.1: (a) Definition of Einav's breakage index B; (b) Integrate the area associated with $B_p, B_t, and\ B$

The relative breakage is defined as an area ratio, referred in Figure 2.1:

$$B = \frac{B_t}{B_p} = \frac{F_0(x) - F(x)}{F_0(x) - F_u(x)} = \frac{g_0(x) - g(x)}{g_0(x) - g_u(x)} \tag{2.1}$$

where g_0, g_u, and g are initial, ultimate and current probability GSDs. F and g are related by:

$$F(d) \equiv F(\Delta < d) = \int_{d_m}^{d} g(\Delta)\, \mathrm{d}\Delta \tag{2.2}$$

where Δ indicates the particles of size less than d; d_m is the smallest particle size. Eq. (2.1) can be rewritten as:

$$g(B, x) = (1 - B) g_0(x) + B g_u(x) \tag{2.3}$$

The relative breakage is limited by $0 \leq B \leq 1$, where $B = 0$ indicates unbroken material and $B = 1$ represents complete breakage.

2.2. Unsaturated Breakage Mechanics (G. Buscarnera & I. Einav, 2012)

The hydromechanical response of granular soils also depends on suction and saturation (Alonso et al., 1990; Fredlund and Rahardjo, 1993; Gens, 2010). Many constitutive theories have been developed for modeling such dependence in the field of unsaturated soil mechanics (Alonso et al., 1990; Wheeler and Sivakumar, 1995). Some constitutive models incorporate hydromechanical coupling by having stiffness, shearing resistance and volumetric compressibility linked with the soil water retention curves (Gallipoli et al., 2003; Wheeler et al., 2003; Sun et al., 2007; Buscarnera and Nova, 2009). The unsaturated breakage mechanics (UBM) is a thermomechanical approach to explain the dependence of yielding on the degree of saturation in crushable granular assemblies. The model has been implemented by numerically implemented using different algorithms (Zhang and Buscarnera, 2015) to simulate the interplay between grain crushing and soil water retention curve (Gao et al., 2016; Zhang et al., 2017).

2.2.1. The Helmholtz free energy for unsaturated granular materials

Clastic yielding of granular soils occurs once the accumulated energy potential reaches to its critical value (Buscarnera and Einav, 2012). Based on this hypothesis, the constitutive model is developed starting with the thermodynamics of elasticity in unsaturated soil. The work input in unsaturated soil is defined as

$$W = \sigma'_{ij}\dot{\varepsilon}_{ij} - ns\dot{S}_r \tag{2.4}$$

where n is the porosity, $s = u_a - u_w$ is suction, $\dot{S}_r$ is the rate of degree of saturation, σ'_{ij} is a generalized effective stress and $\dot{\varepsilon}_{ij}$ is rate of the total strain. It is shown that the work input is decomposed into mechanically developed work input in the grain skeleton and hydraulically evolved work input in the water interfaces. The first law of thermodynamics under isothermal condition can be stated as

$$\mathrm{W} = \dot{\Psi} + \Phi \tag{2.5}$$

where Ψ is the total Helmholtz free energy and Φ is the rate of energy dissipation ($\Phi \geq 0$). It is hypothesized that the total Helmholtz free energy is a function of three variables $\varepsilon^{\mathrm{e}}_{ij}$, S_r, and B and obeys the following additive decomposition:

$$\Psi\left(\varepsilon^e_{ij}, S_r, B\right) = \Psi^M\left(\varepsilon^e_{ij}, B\right) + \Psi^H(S_r, B) \tag{2.6}$$

To further relate the Helmholtz free energy with grain size distribution (GSD), it was hypothesized that energy stored in a grain size fraction between x and $x + dx$ is a function of the grain size, i.e. the mechanical and hydraulic energy stored in this fraction can be denoted by $\psi^M\left(\varepsilon^e_{ij}, x\right)dx$ and $\psi^H\left(\varepsilon^e_{ij}, x\right)dx$, respectively, where ψ is the specific grain size Helmholtz free

energy. Based on discrete element method (DEM) simulation results and capillary force considerations, ψ^M and ψ^H are proposed to scale with x in the following way:

$$\psi^M\left(\varepsilon_{ij}^e, x\right) = \psi_r^M\left(\varepsilon_{ij}^e\right)\left(\frac{x}{D_{rM}}\right)^2 \tag{2.7a}$$

$$\psi^H\left(\varepsilon_{ij}^e, x\right) = \psi_r^H\left(\varepsilon_{ij}^e\right)\left(\frac{x}{D_{rH}}\right)^{-1} \tag{2.7b}$$

where D_{rM} and D_{rH} are reference grain sizes; ψ_r^M and ψ_r^H are reference mechanical and hydraulic free energies. Integrating Eq. (2.7) by the current GSD $\mathrm{g}(B, x)$, the total Helmholtz free energy can be derived as:

$$\Psi^M\left(\varepsilon_{ij}^e, B\right) = \int_{D_m}^{D_M} \mathrm{g}(B, x)\psi_r^M\left(\varepsilon_{ij}^e\right)\left(\frac{x}{D_{rM}}\right)^2 dx \tag{2.8a}$$

$$\Psi^H\left(\varepsilon_{ij}^e, B\right) = \int_{D_m}^{D_M} \mathrm{g}(B, x)\psi_r^H\left(\varepsilon_{ij}^e\right)\left(\frac{x}{D_{rH}}\right)^{-1} dx \tag{2.8b}$$

where D_m and D_M are the minimum and maximum grain diameter respectively. Substituting Eqs. (2.3) and (2.8) into Eq. (2.6), one obtains:

$$\Psi\left(\varepsilon_{ij}^e, S_r, B\right) = (1 - \vartheta_M B)\psi_r^M\left(\varepsilon_{ij}^e\right) + (1 + \vartheta_H B)\psi_r^H(S_r) \tag{2.9}$$

where ϑ_M and ϑ_H are grading indices with expressions:

$$\vartheta_M = 1 - \frac{\int_{D_m}^{D_M} \mathrm{g}_u(x)x^2 dx}{\int_{D_m}^{D_M} \mathrm{g}_0(x)x^2 dx} \tag{2.10a}$$

$$\vartheta_H = \frac{\int_{D_m}^{D_M} \mathrm{g}_u(x)x^{-1} dx}{\int_{D_m}^{D_M} \mathrm{g}_0(x)x^{-1} dx} - 1 \tag{2.10b}$$

They can be determined once the expressions of the initial and ultimate GSDs are specified. In this thesis, the following generic expression is used:

$$\mathrm{g}_0(x) = \frac{(3-\beta)x^{2-\beta}}{D_M^{3-\beta} - D_m^{3-\beta}} \text{ and } \mathrm{g}_\mathrm{u}(x) = \frac{(3-\alpha)x^{2-\alpha}}{D_M^{3-\alpha} - D_m^{3-\alpha}} \tag{2.11a}$$

$$F_0(x) = \frac{x^{3-\beta} - D_m^{3-\beta}}{D_M^{3-\beta} - D_m^{3-\beta}} \text{ and } F_u(x) = \frac{x^{3-\alpha} - D_m^{3-\alpha}}{D_M^{3-\alpha} - D_m^{3-\alpha}} \tag{2.11b}$$

Where β and α determine uniformity of the initial GSD and ultimate GSD respectively. Inserting (2.11a) to (2.10), the grading indices can be calculated by:

$$\vartheta_M = 1 - \left(\frac{5-\beta}{3-\beta}\right)\left(\frac{3-\alpha}{5-\alpha}\right)\frac{\left(D_M^{5-\alpha} - D_m^{5-\alpha}\right)}{\left(D_M^{3-\alpha} - D_m^{3-\alpha}\right)}\frac{\left(D_M^{3-\beta} - D_m^{3-\beta}\right)}{\left(D_M^{5-\beta} - D_m^{5-\beta}\right)} \tag{2.12a}$$

$$\vartheta_H = \left(\frac{2-\beta}{3-\beta}\right)\left(\frac{3-\alpha}{2-\alpha}\right)\frac{\left(D_M^{2-\alpha} - D_m^{2-\alpha}\right)}{\left(D_M^{3-\alpha} - D_m^{3-\alpha}\right)}\frac{\left(D_M^{3-\beta} - D_m^{3-\beta}\right)}{\left(D_M^{2-\beta} - D_m^{2-\beta}\right)} - 1 \tag{2.12b}$$

Through hyperelastic relations, the elastic stress-strain relations can be defined:

$$\sigma' = \frac{\partial \Psi}{\partial \varepsilon^e} = (1 - \vartheta_M B)\frac{\partial \psi_r^M}{\partial \varepsilon^e} \tag{2.13}$$

$$ns = \frac{\partial \Psi}{\partial S_r} = -(1 + \vartheta_H B)\frac{\partial \psi_r^H}{\partial S_r} \tag{2.14}$$

$$E_B = -\frac{\partial \Psi}{\partial B} = \vartheta_M \psi_r^M\left(\varepsilon_{ij}^e\right) - \vartheta_H \psi_r^H(S_r) \tag{2.15}$$

where E_B is the breakage energy that defines the energy release rate upon an infinitesimal shifting of GSD.

2.2.2. Dissipation rate function, yield surface and inelastic flow rules

In triaxial stress space, the dissipation rate function is postulated as:

$$\Phi\left(\dot{B}, \dot{\varepsilon}_v^p, \dot{\varepsilon}_s^p\right) = \sqrt{\Phi_B\left(\dot{B}\right)^2 + \Phi_p^v\left(\dot{\varepsilon}_v^p\right)^2 + \Phi_p^s\left(\dot{\varepsilon}_s^p\right)^2} \tag{2.16}$$

with

$$\Phi_B = \frac{1}{(1-B)cos\omega}\sqrt{E_B E_C}\dot{B} \tag{2.17a}$$

$$\Phi_p^v = \frac{p'}{(1-B)sin\omega}\sqrt{\frac{E_c}{E_B}}\dot{\varepsilon}_v^p \tag{2.17b}$$

$$\Phi_p^s = Mp'\dot{\varepsilon}_v^p \tag{2.17c}$$

$\dot{\varepsilon}_v^p$ and $\dot{\varepsilon}_s^p$ are plastic volumetric and deviatoric strains; E_c is the critical breakage energy controlling yielding strength; ω is 'plastic-breakage coupling angle' to distribute the energy dissipation by breakage and friction; and M is the critical stress ratio between shear stress q and pressure p. Following the standard hyperplasticity procedure (Houlsby and Puzrin, 2007), the yield function and flow rules can be derived:

$$y = \frac{E_B}{E_C}(1-B)^2 + \left(\frac{q}{Mp'}\right)^2 - 1 = 0 \tag{2.18}$$

and

$$\dot{B} = \lambda\frac{\partial\bar{y}}{\partial\bar{E}_B} = 2\lambda\frac{(1-B)^2\cos^2\omega}{E_c} \tag{2.19a}$$

$$\dot{\varepsilon}_v^p = \lambda\frac{\partial\bar{y}}{\partial\bar{p}'} = 2\lambda\frac{(1-B)^2E_B\sin^2\omega}{p'E_c} \tag{2.19b}$$

$$\dot{\varepsilon}_s^p = \lambda\frac{\partial\bar{y}}{\partial\bar{q}} = 2\lambda\frac{q}{M^2p'^2} \tag{2.19c}$$

2.2.3. Elastic and SWRC relations

Substituting the following potential

$$\psi_r^M(\varepsilon_v^e, \varepsilon_s^e) = \frac{1}{2}K\varepsilon_v^{e\,2} + \frac{3}{2}G\varepsilon_s^{e\,2} \tag{2.20}$$

into the reversible constitutive relation (2.13), one obtains the classical linear elasticity

$$p' = (1 - \vartheta_M B) K \varepsilon_v^e \tag{2.21a}$$

$$q = 3(1 - \vartheta_M B) G \varepsilon_e^s \tag{2.21b}$$

where K is the bulk modulus and G is the shear modulus.

The following pressure-dependent elasticity model (Einav and Puzrin, 2004) can provide better description of the compressive behavior of granular materials:

$$\Psi_r^M(\varepsilon_v^e, \varepsilon_s^e) = \frac{P_r}{\bar{K}(2-m)} A^{\frac{2-m}{1-m}} + \frac{3}{2} P_r \bar{G} A^{\frac{m}{1-m}} {\varepsilon_s^e}^2 \tag{2.22}$$

where $A = \bar{\mathrm{K}}(1-m)\varepsilon_v^e + 1$, p_r is a reference pressure, $m = 0.5$ for typic granular material. $\bar{K}$ and $\bar{G}$ are non-nondimensional elastic constants. Based on the pressure-dependent model, the elastic relation is given by:

$$p' = (1 - \vartheta_M B) p_r \bar{K} A^{\frac{1}{m-1}} \left(\frac{1}{\bar{K}} + \frac{3}{2} m \bar{G} A^{-2} {\varepsilon_s^e}^2 \right) \tag{2.23a}$$

$$q = (1 - \vartheta_{\mathrm{M}} B) 3 p_r \bar{G} A^{\frac{1}{m-1}} \varepsilon_s^e \tag{2.23b}$$

A variety of hydraulic potential $\psi_r^H(S_r)$ can be specified to define the shapes of SWRC equations. In this thesis, we use

$$(ns)_{B=0} = -\frac{\partial \psi_r^H}{\partial S_r} = K_w \left(\frac{1}{S_e} - 1 \right)^a \tag{2.24}$$

where $S_e = (S_r - S_{re}) / (1 - S_{re})$ is the effective degree of saturation, while S_{re} and a are two further constants controlling the residual degree of saturation and the slope of the SWRC, respectively.

2.2.4. The hydromechanics of breakage

An index, so-called capillary toughness number, to estimate the intensity of hydromechanical coupling is proposed as:

$$\xi_{CT} = \vartheta_H \frac{K_w}{E_c} \tag{2.25}$$

This index appears in the expression of the yield stress by combining the SWRC equation with the breakage yield surface, and serves as the single factor determines the ratio between yield stress at $S_r = 0$ and $S_r = 1$. This dimensionless index combines the information of initial grading (via ϑ_M), water retention capability (via K_w) and crushing resistance (via E_c). Parametric studies revealed that higher values of ξ_{CT} implies stronger hydromechanical coupling and thus stronger suction-hardening effect.

2.3. Grainsize dependence of clastic yielding (Zhang and Buscarnera, 2014)

This paper explores how grain size characteristics influence the link of grain crushing to suction and degree of saturation based on the constitutive model of UBM. By calibrating model parameters for sand type material, the hydromechanical energy potential is specifically chosen to study the relation. The analysis predicted the dependence of yielding on the elastic characteristics and water retention properties and their grain size dependence. The suggested factor of capillary toughness number in the UBM model was employed to find the grain size effect on the intensity of hydromechanical coupling. The datasets of K_w and E_c, which are model parameters representing water retention and yielding properties, are developed from existing literatures. The collected data have been plotted against a grain size descriptor D_{50} as shown in Figure 2.2. The figure clearly shows that the both constants are inversely proportional to the average grainsize.

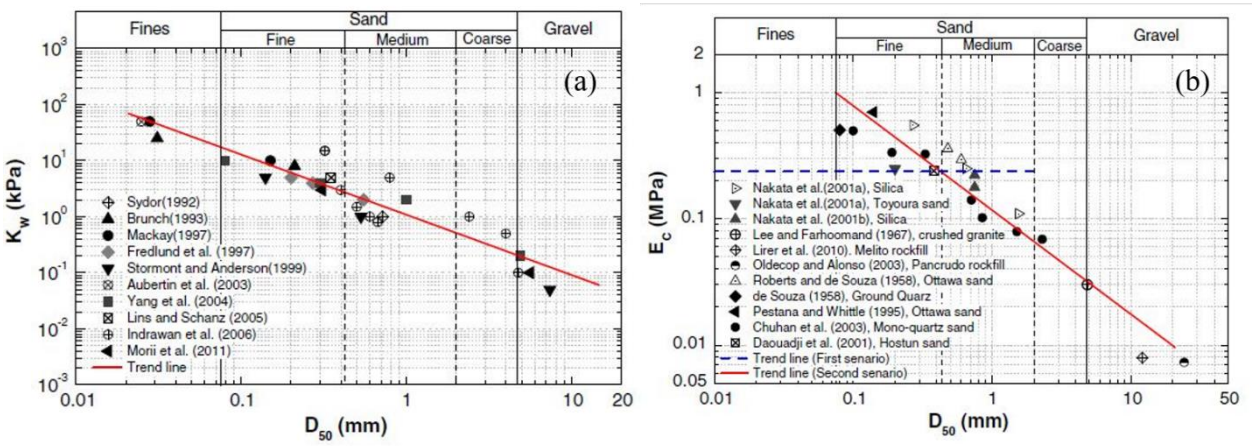

Figure 2.2: The grainsize dependence on the two model parameters: (a) The grainsize dependence on K_w; (b) The grainsize dependence on E_c

The collected value of K_w and E_c along with ϑ_H are used to compute the capillary toughness number ξ_{CT} [Eq. (2.25)]. Two trendlines are obtained and plotted in Figure 2.3 assuming (a) E_c is constant (plotted as dotted line) (b) E_c is dependent on grainsize (plotted as solid line). While the grainsize dependence on the coupling extent is controlled with only capillary effect in the first case, the two factors of water retention capability and yielding properties are engaged in quantifying the dependence in the second case. The first scenario

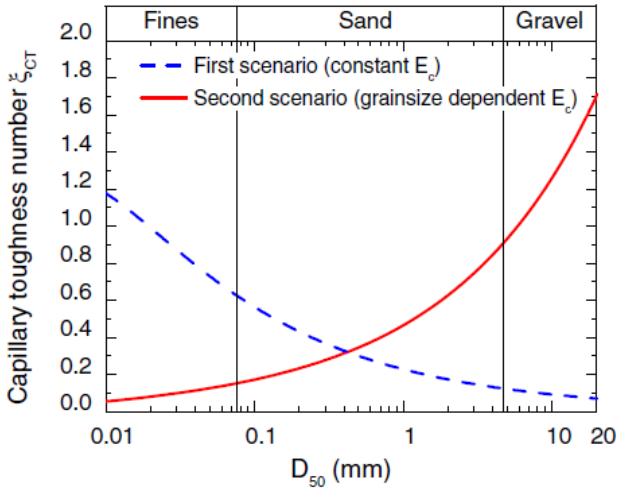

Figure 2.3: Predicted dependence of capillary toughness number on mean grainsize

shows that finer gradings are predicted to have lower values of ξ_{CT}, meaning less suction-hardening and stronger hydromechanical coupling effect. However, having grain size dependent E_c gives a reversed trend. This implies that the breakage energy threshold E_c decreases faster than the capillary effects for larger grading of granular materials.

2.4. Evolution of the SWRC Subjected to Grain Crushing (Gao et al. 2016)

The study explores the interplay between soil water retention curve and grain crushing. Specimens of sand and glass beads were subjected to oedometric compression test with different stress levels. SWRC tests are conducted for the crushed specimens. Sieve analysis is also carried out to obtain grain size distribution for evaluating the degree of breakage defined by Einav (2007). The produced data suggests water retention capability strongly depends on the level of grain breakage. The coevolution of soil water retention curve and grain crushing are interpreted by the Arya and Paris model (Arya and Paris, 1981), the Modified Kovacs model (Aubertin, Mbonimpa, Bussière, & Chapuis, 2003) and UBM. In the Arya Paris (AP) model, a selection of scaling parameter α plays an important role in determining suction air entry value, which is difficult to determine a priori given its dependency on the gradation of the specimen. The prediction of SWRC using the MK model for crushed soil has reasonable matches with the measured data, although it overpredicts the suction air entry value for uncrushed soils. In the case of UBM, model parameters are firstly calibrated to match the experimentally produced compression curve and the SWRC of the uncrushed specimen. The model then naturally predicts the coevolution of SWRC and grain crushing. Figure 2.4 presents comparison between UBM prediction and experimental data for sand and glass beads.

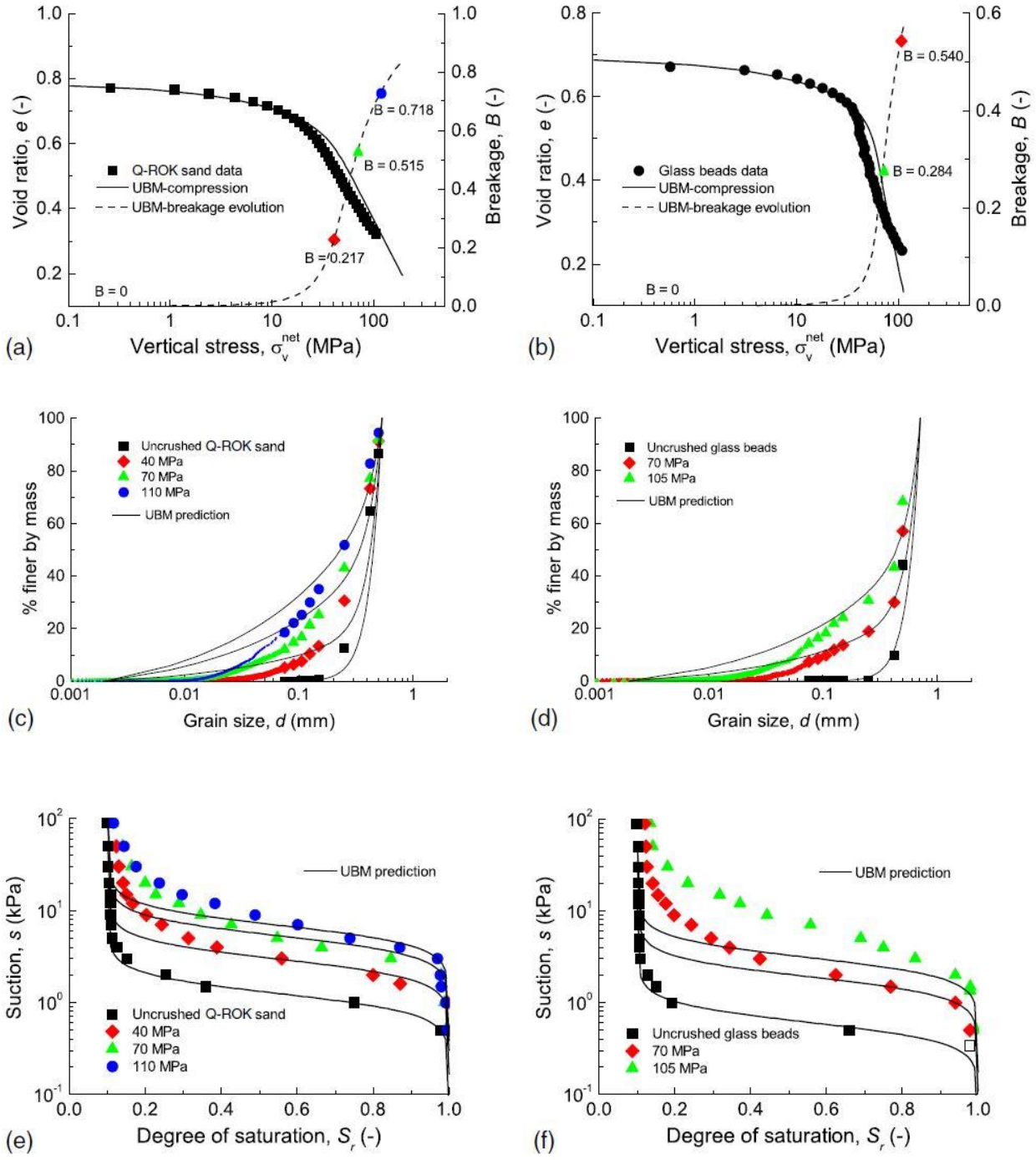

Figure 2.4: Comparison between experimental data and UBM prediction data for sand typed soil and glass beads: (a and b) compression curve; (d and e) GSD; (f and g) SWRC. After Gao et al. (2016)

2.5. Compression of Unsaturated Clay under High Stresses (Mun and McCartney, 2015)

This study investigated the isotropic compression behavior of unsaturated clay under high pressure to 160 MPa and drainage condition. This work is conducted on the High Pressure Isotropic Compression device, which is also the primary experimental equipment used in this thesis. The study compares the compression behaviors of compacted clay in between undrained and drained conditions, and evaluates the difference of deformation properties between fully saturated and partially saturated clay in the both conditions.

A series of undrained isotropic compression tests for clay specimen were performed under mean stress up to 160 MPa with several initial degrees of saturation (Sr = 1.0, 0.9, 0.8). The obtained results are shown in Figure 2.5. It is clearly shown that the curve moves downwards as the initial degree of saturation decreases. It represents that drier soil has lower initial undrained bulk modulus due to the high compressibility of air.

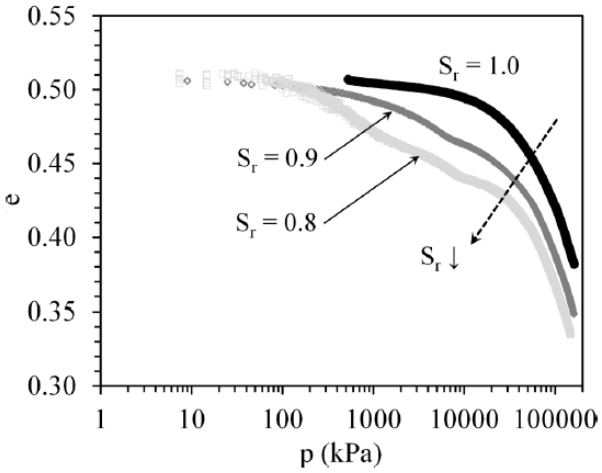

Figure 2.5: Undrained compression curves of clay specimens with different initial degrees of saturation

The isotropic compression tests in the drained condition were conducted for the saturated and unsaturated clay under high pressures up to 160 MPa. In the tests, more increase in amount of outflow water is found in higher initial degree of saturation with the same mean effective

stress (Figure 2.6). Water outflow is instantly increased from beginning of the compression in saturated clay, while a delay of water outflow is observed for partially saturated clay (S_r = 0.9 and 0.8).

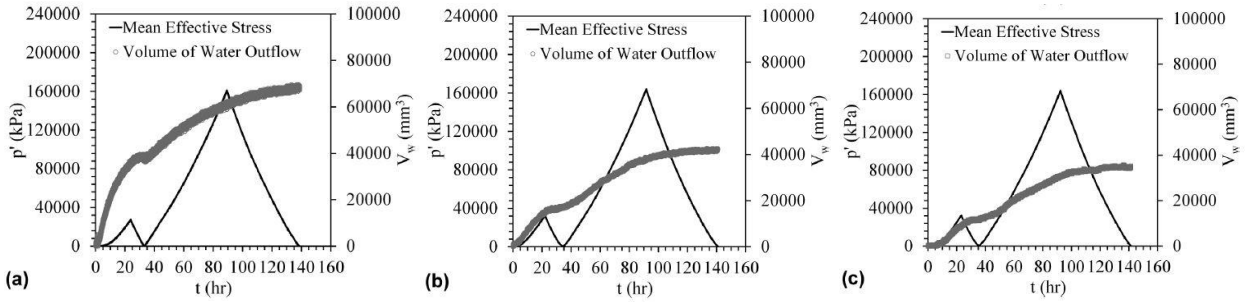

Figure 2.6: Change of mean effective stress and water outflow in time of clay specimen with different initial degree of saturation during drained compression: (a) S_r = 1.0; (b) S_r = 0.9; (c) S_r = 0.8

Furthermore, a difference between the total volume change and the outflow of water for the specimens with different initial degrees of saturation is observed in Figure 2.7. For the saturated specimen, the total volume of the specimen is identically changed as the amount of water flowed out, up to a specific stress level where the specimen becomes dense, as shown in Figure 2.7 (a). The difference between the volume of outflow and the void increases in specimen with higher initial degree of saturation. The volume trend of water outflow becomes close to the volume change of specimen after a certain stress around 4 MPa, as presented in Figure 2.7 (b) and (c). This means compression behavior of unsaturated clay become similar to the one of saturated clay, after approaching a certain stress making pressurized saturation.

The phenomenon is emphasized in Figure 2.8 (a) where the drained $e - log\, p'$ compression curves for the specimens are plotted. The compression lines of unsaturated clay become overlapped with the one for saturated clay at the virgin compression behavior, although they are differently started with higher pre-consolidation stress for lower initial degree of saturation. The results are coincided with the hypothesis that pressurized saturation is occurred in

unsaturated soil after effects of suction is marginalized. In Figure 2.8 (b) with the logarithmic scale for p', suction hardening effect on the deformation behavior is clearly shown. The saturated clay deforms more than the unsaturated clay at the low mean effective stress. However, all the compression curves converge to one line after certain stress level has been reached.

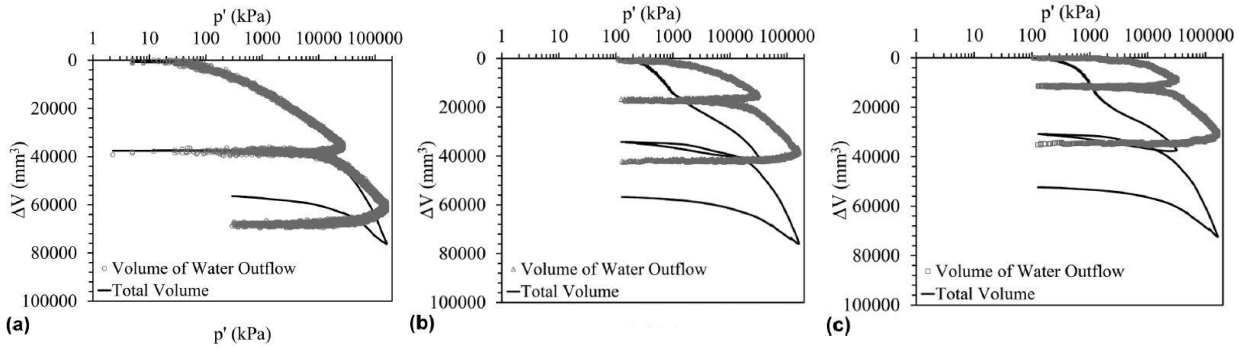

Figure 2.7: Comparison of changes between total volume of specimen and water outflow according to mean effective stress for the specimens with different initial degrees of saturation: (a) $S_r = 1$; (b) $S_r = 0.9$; (c) $S_r = 0.8$

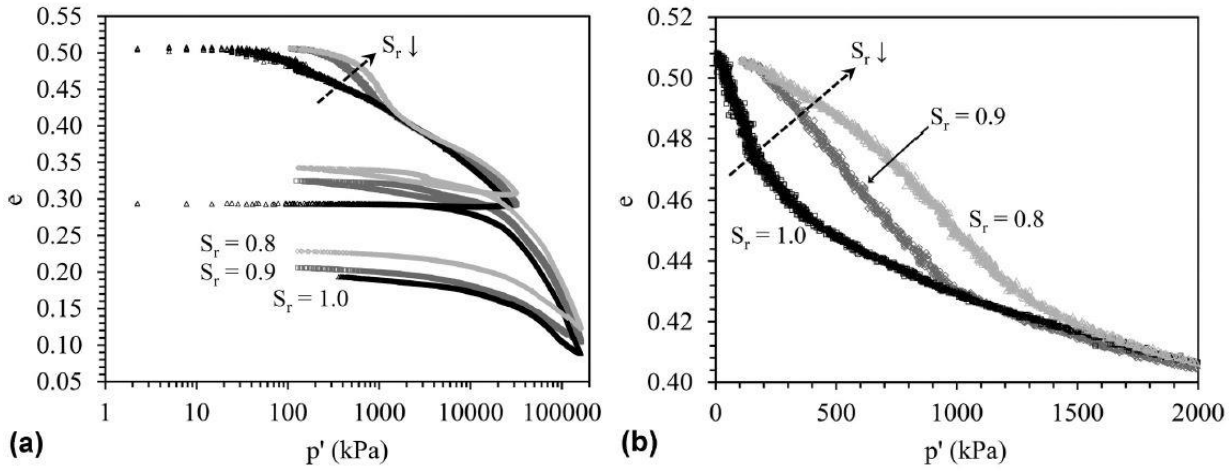

Figure 2.8: Compression curves of clay specimen: (a) $e - log\ p'$; (b) $e - p'$

2.6. Roles of Particle Breakage on the Isotropic Compression of Sand (Mun and McCartney, 2017)

This paper presents another study conducted on the HPIC device. Saturated and dried Mason sand were subjected to compression test under high pressure up to 160 MPa with drained and undrained condition. The results are compared to evaluate a role of drainage in compression

behavior of sand for the different saturated condition. The effects of drainage and saturation condition on the particle breakage are investigated by produced particle size distribution after compression tests with different stress level. Furthermore, this paper analyzes a dependence of initial relative density on compression behavior of sand and degree of particle breakage.

2.6.1. Isotropic Compression Response of Dry and Saturated Sand

The dry Mason sand was subjected to the compression test under both of drained and undrained condition but only drained condition is applied to the test for saturated Mason sand. A series of test results are presented in Figure 2.9. The deformation behavior of dry sand is accordance with an accepted response for the loading curves [Figure 2.9 (a)]. The compression curve for dry sand in undrained condition is plotted in Figure 2.9 (c) and (d). The figures present similar result to the behavior of dry sand in drained condition. This means that pore air does not have a significant role in the compressive deformation of dry sand due to its high compressibility. Compression curve of saturated sand in undrained condition is obtained in Figure 2.9 (e) and (f) and they show small deformation of the specimen.

2.6.2. Particle Breakage during Isotropic Compression

To quantify particle breakage of the specimens, particle size distributions were produced before and after the compression test (Figure 2.10). Comparing the particle breakage distribution for dry sand with the different drainage condition, undrained specimen have a just greater breakage than undrained specimen. Whereas particle breakage is gradually developed in undrained and drained dry sand as stress level increases, it is hardly occurred in undrained saturated sand and the breakage is marginally evolved between the stresses.

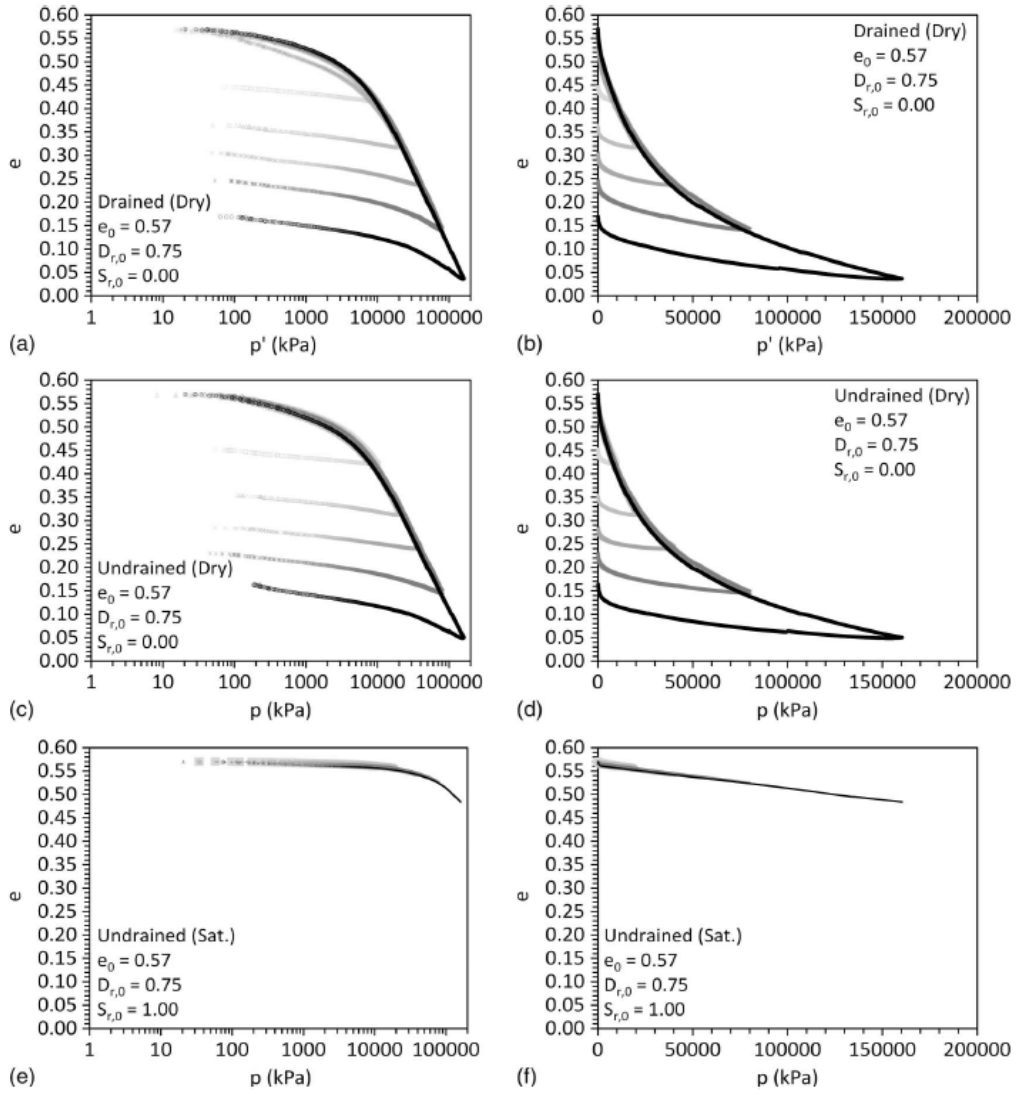

Figure 2.9: Isotropic compression curves of the sand specimen with different drainage condition: (a) $e - log\, p'$ (Dry sand in drainage); (b) $e - p'$ (Dry sand in drainage); (c) $e - log\, p'$ (Dry sand in no drainage); (d) $e - p'$ (Dry sand in no drainage); (e) $e - log\, p'$ (Saturated sand in no drainage); (f) $e - p'$ (Saturated sand in no drainage)

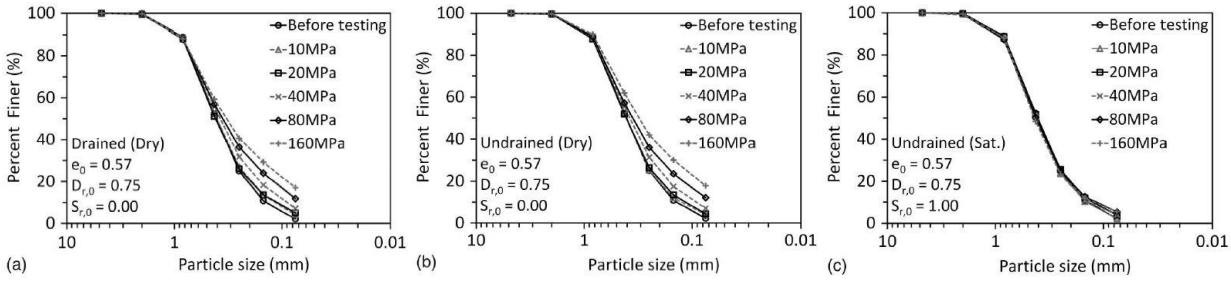

Figure 2.10: Particle size distribution of Mason sand for all the stress levels: (a) drained dry sand; (b) undrained dry sand; (c) undrained saturated sand

To investigate a role of initial relative density in compression behavior and particle breakage of dry sand, the compression tests were conducted under 160 MPa and drained condition. The following compression curves and particle size distributions are shown in Figure 2.11. In the compression curves, although the behavior is divergently developed as different initial relative density at the pre-consolidation state, however, they converged to a distinctive virgin compression line at approximately 20 MPa. In the comparison of the particle size distribution, it is found that the dependence of initial relative density is negligible for particle breakage in this paper, as shown that all the distribution curves are overlapped in Figure 2.11 (b).

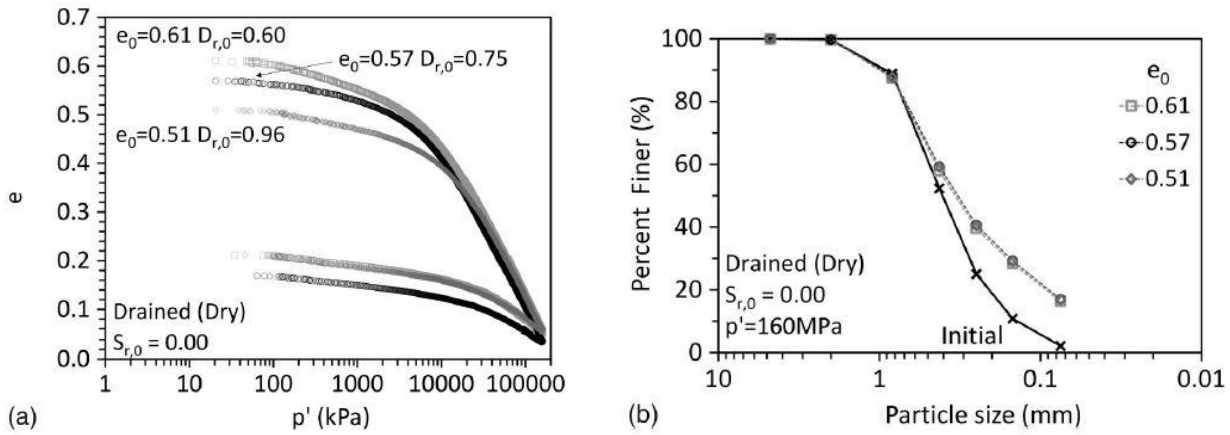

Figure 2.11: Dependence of initial relative density: (a) compression curves; (b) particle size distribution after isotropic drained compression test under 160 MPa

2.7. Summary

UBM seems to be a versatile tool to interpret the coevolution of grain breakage and SWRC in an integrated manner. The current results by Gao et al. (2016), however, is only limited to two granular samples with specific grain sizes. It is desirable to enrich the dataset by validating UBM against other types of granular materials characterized by coarser and finer initial GSD compared to those studied in previous investigations. This will allow us to investigate the grain size effect on the crushing resistance and water retention capacity, as well as estimate the intensity of hydromechanical coupling as a function of D_{50}.

To test the performance of the HPIC device, high pressure isotropic compression test will be performed similar to the work of Mun and McCartney (2017). To amplify the breakage effect, it is desirable to use sand with more uniform gradings and larger grains than Mason sand. It is expected that such sand will exhibit higher crushability and more prominent GSD evolution during loading. While the two breakage theories by Marsal (1967) and Hardin (1985) were used by Mun and McCartney's study for quantifying breakage degree, this study will rely on the breakage mechanics theory and consequently the breakage index defined by Einav (2007) to interpret the results.

CHAPTER 3: VALIDATION OF UBM USING ADDITIONAL DATA

3.1. Experimental Program

3.1.1. Testing materials

To complement previous findings for Q-ROK#1 sand (D_{50}=0.36 mm) and soda-lime glass beads (D_{50}=0.55 mm) used by Gao et al. (2016), two more materials each for natural granular material (sand) and idealized granular material (glass beads) respectively are adopted, with drastic difference of their mean grain size. For natural sand, Q-ROK#4 sand with D_{50}=1.1 mm and CFS sand with D_{50}=0.12 mm (Producer: U.S. Silica, Plant: Berkeley Springs, West Virginia) are used in this study. Both sands are made of >99% SiO_2, characterized by highly angular geometries and are consistent with the Q-ROK#1 sand used in the previous study. For convenience, the CFS, Q-ROK#1 and ROK#4 sand will be hereafter referred to as fine sand, medium sand and coarse sand respectively. For idealized granular materials, two soda-lime glass bead assemblies with D_{50}=0.12 mm and D_{50}=1.2 mm are adopted, which will be referred to as small GB and large GB respectively. The glass bead samples used in the previous study (D_{50}=0.55 mm) are thus re-named as medium GB for consistency. The initial grain size distributions (GSD) for the 4 new materials and the 2 previously tested materials are presented in Figure 3.1.

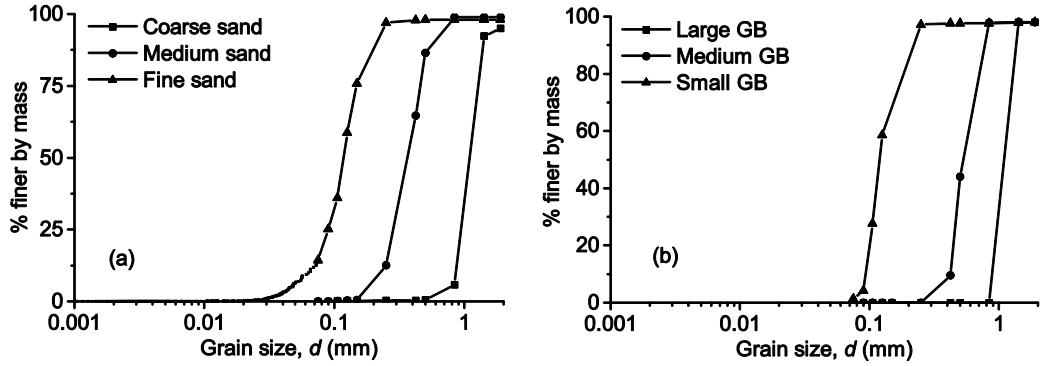

Figure 3.1: GSD of the tested sand and glass bead specimens

The representative microscopic photos of their grains are shown in Figure 3.2. It is observed that Q-ROK sand particles are highly angular and contains many irregular asperities, whereas glass beads are almost perfect sphere with smooth surface texture.

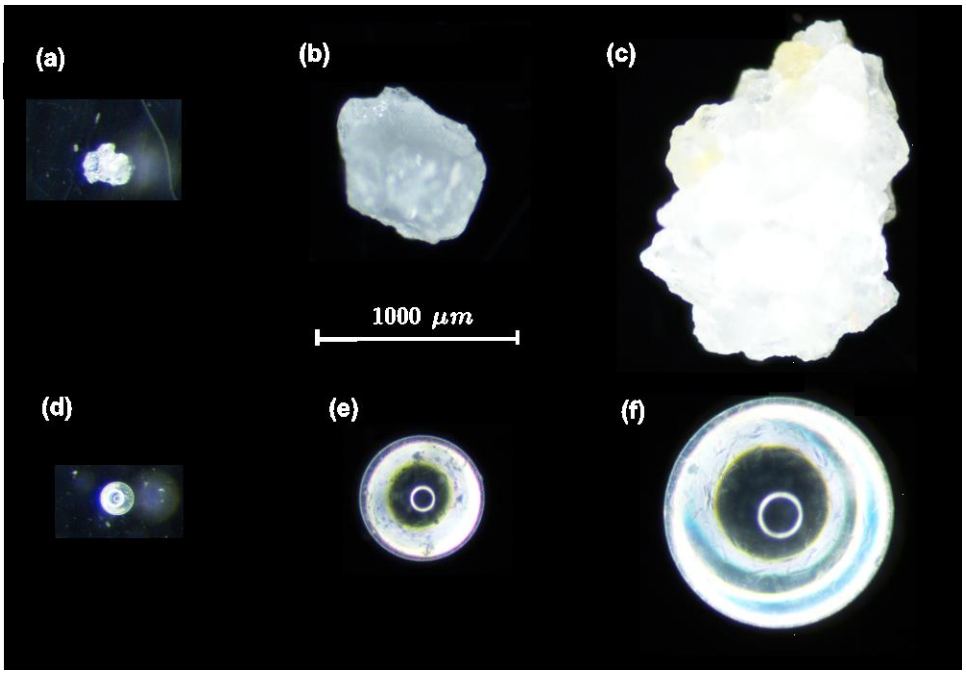

Figure 3.2: Images of the particles of the testing materials: (a)-(c) sand, (d)-(f) glass beads

3.1.2. Testing Program

All specimens for one-dimensional compression tests are prepared via a dry pluviation procedure to ensure the same input energy for packing. Then each specimen is subjected to strain-controlled (0.4%/min) 1D compression until the target vertical stress is achieved. For sand specimens, compressions are terminated at three stress levels to create specimens with different level of crushing. Only one stress level σ_v=110 MPa is inspected for glass beads due to the limited material available in the lab. After compression, the crushed specimens are reassembled in a Temp Cell (Soilmoisture Equipment, Goleta, California) for SWRC measurement. As observed in the previous study, it is not possible to re-constitute the crushed specimens to the same void ratio of the initial oedometer specimens due to the severe change in GSD and

production of fines. Thus, all specimens subjected to water retention testing have been reconstituted through the same procedure, which involved wet pluviation guaranteeing the same input energy for packing, as well as an initially saturated state. The SWRC curves have been measured by controlling the air pressure up to desired levels and monitoring the weight loss of the Tempe Cell at equilibrium conditions. After SWRC measurements, wet sieve analyses have been carried out to define the GSD curve for grain-size fractions greater than 0.075 mm. The portions of the GSD curves finer than 0.075 mm are characterized through image analysis as described in (Gao et al., 2016).

3.1.3. Testing results

The compression curves for the four materials, together with the previous result of medium sand and medium GBs are presented in Figure 3.3. Despite the different initial void ratio prepared under same packing energy, a consistent trend is observed on the location of the limiting compression curve (LCC) (Pestana & Whittle, 1995). It is observed that for both materials, the smaller the mean grain size the higher range of pressure LCC locates.

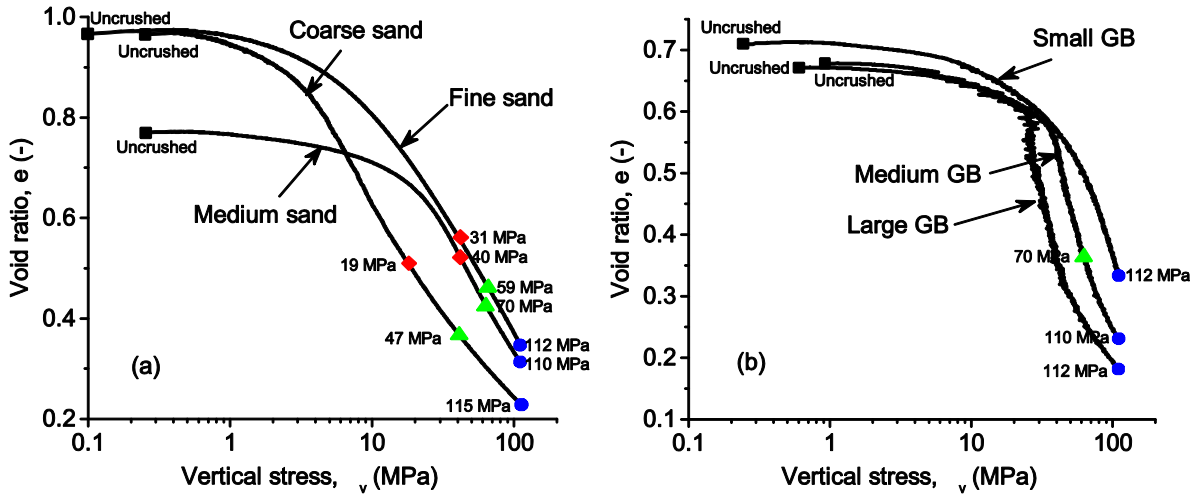

Figure 3.3: Compression curves for (a) sand and (b) glass beads

The GSDs of the crushed specimens are plotted together with that of the uncrushed ones in Figure 3.4. A common trend observed from these curves is that crushing under monotonic loading does not alter the maximum grain size while the amount of fines is rapidly accumulated. Such observation corroborates other findings from numerical simulations (Tsoungui et al., 1999; Ben-Nun and Einav, 2010), in that large particles get cushioned by surrounding smaller particles during fragmentation, thus prohibiting them from breakage. Another observation is that all the GSD curves appears to evolve, at different rates, towards a final self-similar distribution. Such evidence together with many others from lab tests (Coop, Sorensen, Bodas Freitas, & Georgoutsos, 2004) and geological fault gouges (Sammis et al., 1987) justifies the assumption of an ultimate fractal GSD that attracts all the GSD curves during comminution. This assumption enables the use of breakage index defined by Einav (2007) for continuum description of crushable granular materials.

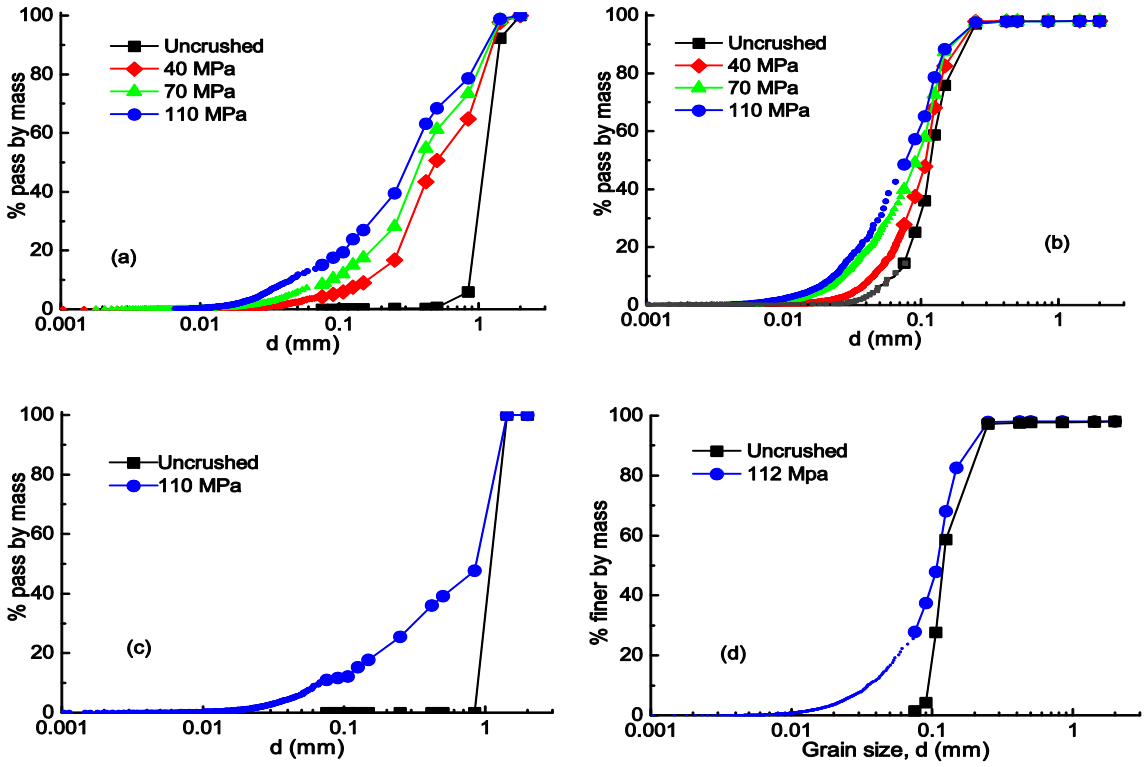

Figure 3.4: GSDs for (a) coarse sand; (b) fine sand; (c) large GB; (d) small GB

The SWRCs of the original and crushed specimens are shown in Figure 3.5. All materials display a significant increase in s_{AEV} and a slight increase on the slope of the middle portion of the SWRCs as comminution progresses. Such result is expected considering that the increased percentage of fines (reflected by increase in D_{10}) and the transition towards a well-graded soil (reflected by increase in C_u) will decrease the peak values of pore size and broaden up the overall pore size distribution curves.

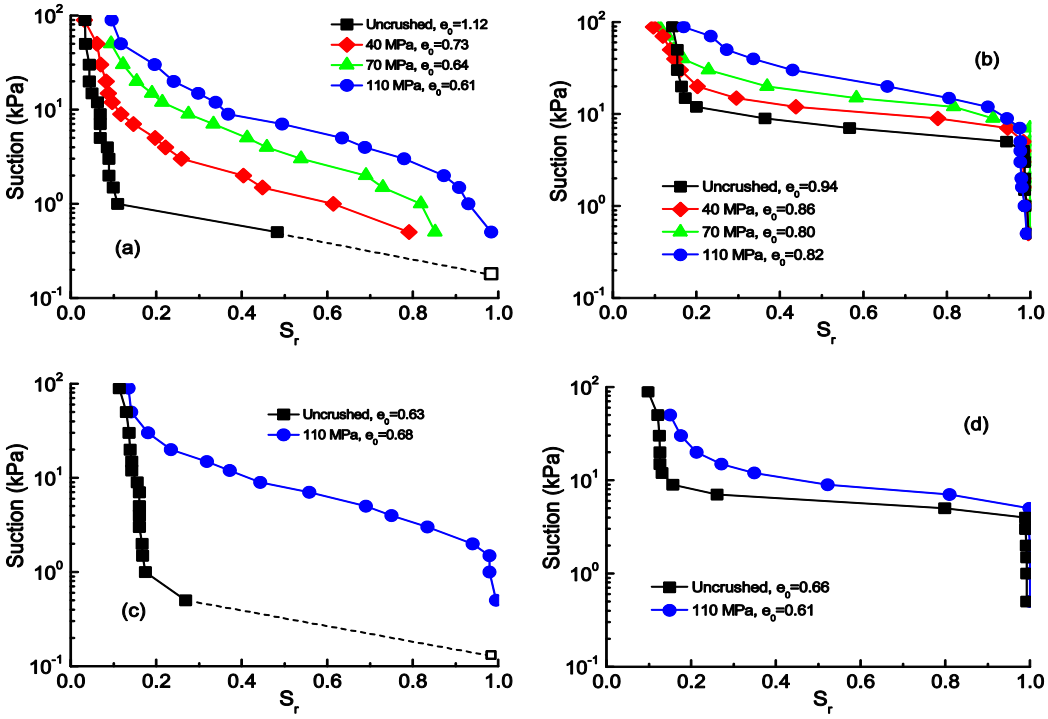

Figure 3.5: SWRCs for (a) coarse sand; (b) fine sand; (c) large GB; (d) small GB. The dashed line and open square in (a) and (c) indicate an extrapolation of the curve within a suction rage beyond the resolution of the equipment

Table 3.1: Characteristic values of GSD and SWRC

Material	Extent of crushing	*e*	s_{AEV} (kPa)	D_{10} (mm)	D_{50} (mm)	C_u
Coarse sand	Uncrushed	1.12	0.08	0.882	1.132	1.23
	Crushed at 19 MPa	0.73	0.26	0.153	0.512	2.40
	Crushed at 47 MPa	0.64	0.68	0.089	0.393	1.83
	Crushed at 115 MPa	0.61	1.42	0.045	0.335	2.55
Medium sand	Uncrushed	0.8	0.78	0.227	0.364	1.77
	Crushed at 40 MPa	0.73	1.45	0.125	0.362	2.85
	Crushed at 70 MPa	0.75	2.35	0.058	0.274	5.50

	Crushed at 110 MPa	0.65	3.18	0.04	0.234	7.18
Fine sand	Uncrushed	0.94	3.43	0.063	0.121	1.29
	Crushed at 31 MPa	0.86	6.45	0.045	0.111	1.48
	Crushed at 59 MPa	0.8	7.88	0.027	0.091	1.85
	Crushed at 112 MPa	0.82	8.43	0.023	0.078	2.00
Large GB	Uncrushed	0.63	0.08	0.930	1.210	1.22
	Crushed at 112 MPa	0.68	1.67	0.068	0.082	3.48
Medium GB	Uncrushed	0.62	0.32	0.425	0.551	1.38
	Crushed at 70 MPa	0.59	0.59	0.108	0.497	4.85
	Crushed at 105 MPa	0.57	0.57	0.059	0.444	8.07
Small GB	Uncrushed	0.66	3.89	0.093	0.124	1.34
	Crushed at 112 MPa	0.61	4.12	0.035	0.103	1.51

3.2. UBM Interpretation

For each type of material, model parameters are determined based on the following procedure.

Step 1: determine the grading descriptors for the cumulative GSD Eqs. (2.11) based on initial GSD data. In the equation, the minimum grain size D_m is adjusted here to best match the GSDs at lower ranges (i.e. d=0.01mm ~ 0.1mm). Based on the descriptors, the grading indices ϑ_M and ϑ_H can be computed using the Eqs. (2.10).

Step 2: determine the mechanical parameters (E_c, M, ω, $\bar{K}$, ν) using the compression data. Among them, E_c and $\bar{K}$ controls the yielding and stiffness of the material under isotropic compression, while M and ν controls those subjected to shearing stress path. Since 1D compression responses are governed mainly by E_c and $\bar{K}$, the value of M and ν are fixed as 1.3 and 0.1 for all samples, respectively. The value of ω controls the compressibility in the post-yielding regime.

Step 3: determine the hydraulic parameters for the SWRC equation Eq. (2.24) based on initial SWRC data.

The determined parameters to make best-matched prediction are presented in the Table 3.2.

Table 3.2: Parameters of UBM

	Initial GSD			Initial SWRC			Mechanics					Computed grading indices	
Materials	D_m (mm)	D_M (mm)	β	K_w (kPa)	a	S_r^{res}	$\bar{K}$	ν	ω	M	E_c (MPa)	ϑ_H	ϑ_M
Coarse sand (Calibrated based on Compression)	0.006	1.427	-1	0.2	0.5	0.05	1800	0.1	55	1.3	0.035	13.4463	0.7184
Coarse sand (Calibrated based on GSD)	0.006	1.427	-1	0.2	0.5	0.05	5000	0.1	45	1.3	0.7	13.4463	0.7184
Fine sand	0.004	0.167	1.3	3.55	0.2	0.15	1400	0.1	20	1.3	2.8	2.4167	0.5396
Large GB	0.005	1.427	-1	0.15	0.5	0.15	3500	0.1	72	1.3	0.64	15.39	0.7209
Small GB	0.012	0.143	-1	2.2	0.2	0.12	3100	0.1	60	1.3	2.6	1.7198	0.6033

Figure 3.6 compares the UBM simulations with the data measured for the four materials. The compression responses of all specimens are well captured since the mechanical parameters have been calibrated based on the compression data. The predicted breakage evolution curves are plotted together with the experimentally determined *B* values (using the area-based definition by Einav (2007)) in Figure 3.6. At each stress level, the predicted *B* values can be further used to locate the GSD and SWRC via Eqs. (2.3) and (2.14). It is observed that, except for coarse sand (the case of which will be discussed later), the predicted GSDs match reasonably well with the experimental data at all stress levels. Similarly, the predicted SWRCs using the same set of *B* values well captures the SWRCs of crushed specimens for fine sand, small GB and large GB. Note the slight change of the shape of the SWRCs as comminution progresses is not captured, since the current UBM model can only predict the shifting of s_{AEV} via the term $\left(1+\vartheta_H B\right)$ in the Eq. (2.14). This limitation results in an underestimation of the suction values of severely crushed samples at high suction regime. A more accurate model would have the baseline SWRC Eq. (2.24) depends on the breakage *B*, which will require substantial change of the total Helmholtz free energy Eq. (2.9) and demands further micromechanical and experimental justifications.

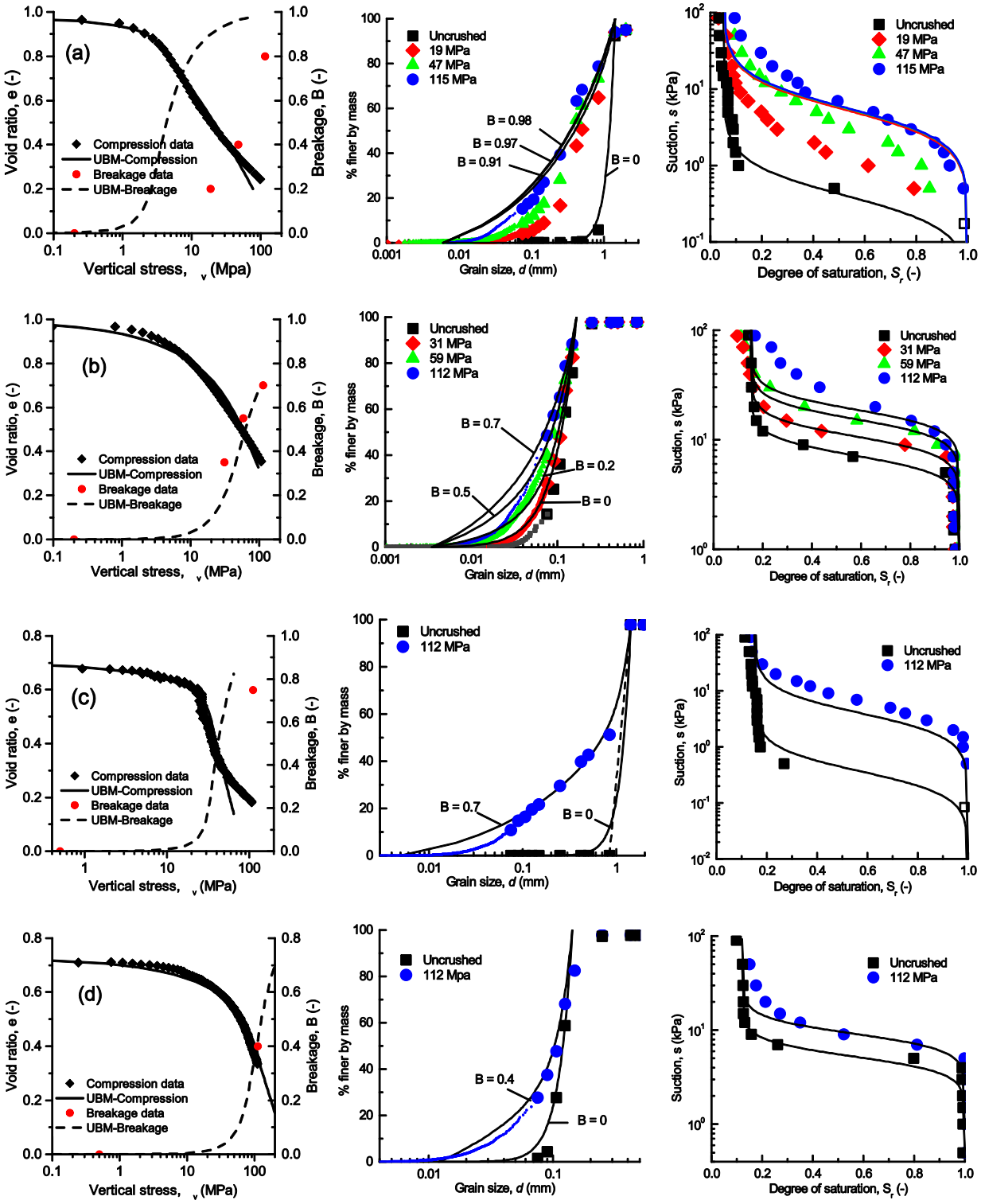

Figure 3.6: Comparison between measured data and UBM predictions for (a) coarse sand; (b) fine sand; (c) large GB; (d) small GB

For the coarse sand, it is found that the degree of comminution is severely overpredicted at all stress levels. Such over prediction is reflected in the breakage evolution, GSD and SWRC curves simultaneously. There are possibly two reasons for such result: **1)** From microscopic images (Figure 3.2), it is observed that the coarse sand particles contain more asperities comparing to the medium and fine sands. Calculations of the circularity index (Ham et al., 2011) $C = 4\pi A / P^2$, where A is the particle area and P its perimeter , of all sand particles have indeed revealed that the coarse sand tested in this study has much rougher surface texture than the other two sands (Sohn et al., 2017). In other words, there is a lack of geometrical similarity among the particles of the three sands. The current version of UBM does not explicitly consider the effect of grain shape and thus cannot distinguish grain breakage due to dominantly asperity abrasion or particle crushing. Therefore, the model cannot predict the apparent yielding caused by breakage of the asperities where massive grain crushing has not occurred yet. Therefore, the mechanical parameters calibrated to match the apparently yielding can significantly underestimate the crushing resistance of the granular matrix and further accelerate the growth of breakage, as observed in Figure 3.6. **2)** The aforementioned grain shape effect can be exacerbated by the fact that coarse sand specimens are all loosely packed (i.e. e_0=1). Particularly, a slight change of the grain geometry (i.e. asperity breakage) can lead to large irreversible volume strains. Such mechanism may further promote an apparent yielding at macroscale without the occurrence of massive grain crushing. The current model contains only one yield surface which is associated with grain breakage. As a result, yielding caused by pore collapse or grain rearrangement without crushing may not be fully captured. To provide further evidence for the above-mentioned arguments, the critical breakage energy E_c and the nonlinear bulk modulus $\bar{K}$ are increased to much higher values to match the breakage evolution data. The computation result is shown in

Figure 3.7. This time, the GSDs and SWRCs are well captured at all stress levels, while the yield stress is over predicted since the model cannot reflect the 'apparent yielding' caused by asperity breakage and void collapse.

These results point out potential directions for future improvement of breakage mechanics models. Particularly, the effect of grain shape should be correctly reflected in the model via additional parameters or new internal variables. The recent work by Zhang et al. (2016) has taken the first step towards such direction by including various contact and failure models in calculating the critical breakage energy E_c. This micromechanical approach has successfully explained the effect of grain size on characteristic strength and fracture energy of individual particles and the yield stress of granular assemblies. The insight gained from such study, however, is only applicable to the onset of breakage on brittle granular materials. Hence, the effect of the grain shape on the evolution of the system after yielding demands further theoretical and experimental studies. In particular, enhanced breakage evolution laws accounting for the shape of the grain could be formulated in order to enable breakage mechanics models to capture more accurately the inelastic behavior of a wider range of granular soils.

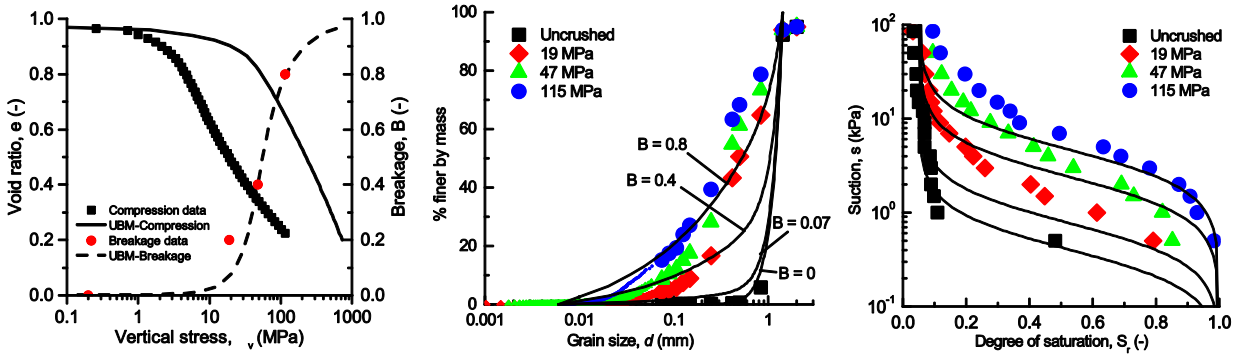

Figure 3.7: Performance of UBM after adjusting the mechanical parameters to match the GSD data of coarse sand

3.3. Grainsize effect on hydromechanical coupling

The effect of grain size on the hydraulic and mechanical behaviors of unsaturated crushable soils can be readily visualized by plotting K_w and E_c, i.e. the two central parameters that reflect the water retention capability and the crushing resistance of the granular matrix, against the mean gran size D_{50}. Figure 3.8 (a) presents the values of K_w obtained in this study. The trend is consistent with the previous dataset collected by Zhang and Buscarnera (2014), in that soils with larger mean grain size are characterized by lower values of K_w and hence lower suction air entry value. The slope of the power law trendline for the new data is approximately -1 which is consistent with the former trendline. Such slope can be explained by the capillary theory, by which the height of capillary rise is inversely proportional to the size of the capillary tube (or the mean pore size in this case). Figure 3.8 (b) plots the calibrated values of E_c for Q-ROK sand and glass beads. For coarse sand, the value of E_c that provides the best match of the GSD evolution curves from Figure 3.8 is shown here, in that it reflects more directly the energy threshold associated with major particle breakage and GSD alteration. It is observed that the grain size dependency for both materials display similar slope on the log E_c-log D_{50} plot, in consistent with the previous findings (Zhang and Buscarnera, 2014).

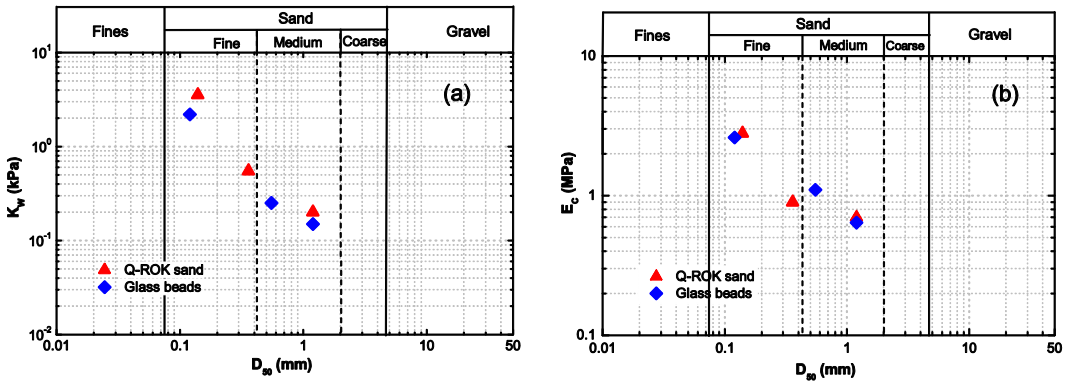

Figure 3.8: Grain size effect on the value of (a) air-entry parameter Kw and (b) critical breakage energy Ec.

The capillary toughness number ξ_{CT} [Eq. (2.25)] is computed with the determined parameters E_c and K for Q-ROK sand and glass beads in Figure 3.9. Both materials are predicted to have stronger hydromechanical coupling effect at larger grain sizes. This result, as discussed in Zhang and Buscarnera (2014), is a consequence of the competition between the deterioration of crushing resistance and water retention capacity as D_{50} increases. For the present case, the decrease of breakage threshold dominates such competition and thus the coupling is predicted stronger in soils with larger grains. It should be noted that such prediction is made for soils with grain size between 0.1 – 2 mm. For finer soils (D_{50} < 0.075mm), this conclusion is no longer valid since grain breakage plays a less important role in dissipating energy and other intergranular forces become important (e.g. electrical force). Similarly, this prediction cannot be extrapolated for gravels and boulders (D_{50} > 10mm) where interparticle capillary forces reduces to a negligible level. Lastly, it should be noted that regardless of the increasing trend of ξ_{CT}, the magnitude of ξ_{CT} for all the six materials is very low, thus confirming that sands are characterized by weak values of water sensitivity compared to other geomaterials such as clays and rockfill.

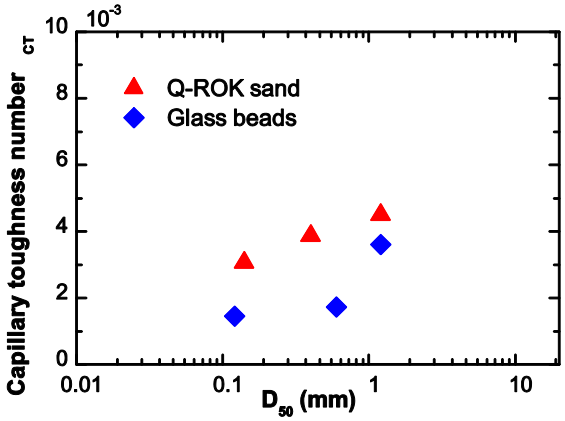

Figure 3.9: Grain size effect on the intensity of hydromechanical coupling.

CHAPTER 4: EXPERIMENTAL SETUP AND TESTING APPROACH

4.1. High Pressure Isotropic Compression Device

The High Pressure Isotropic Compression Device was designed to hold confining pressure up to 160MPa and thus is able to crush different types of granular soils. Figures 4.1 and 4.2 show the picture and the schematic of the device, respectively. The experimental setup consists of four major components: high-pressure syringe pump, pressure control panel, data acquisition system (DAQ) and high pressure isotropic cell. The high-pressure syringe pressure pump (Figure 4.3), manufactured by Teledyne Isco, is capable of applying 0.07 - 165 MPa pressure to the isotropic cell at injection rate of 0.00001 - 25 mL/min and tracking the volume change of the specimen. Details of the syringe pump are presented in Table 4.1. The pressure control panel (Figure 4.4) controls suction, tracks the change of degree of saturation during the tests for partially saturated soil specimen, and controls the cell pressure at low pressure ranges. The panel consists of three tubes and two pressure gauges. Two tubes control pore air pressure (u_a) and pore water pressure (u_w) of the specimen, respectively. The other tube is used to provide pressure fluid to the cell before the high-pressure test and collect the pressure fluid after the test. The maximum pressure that can be provided by the three tubes is 850kPa. A differential pressure transducer (DPT), which is connected to water burette, monitors the volume of water outflow from the specimen. The DPT used for the test is a Model P300D produced by Validyne and has a capacity of 55 kPa with a 3-34 diaphragm. The pressure difference signal is amplified and modulated through DAQ system in an electric unit (mV) and then visualized in the desktop with using a NI-DAQmx program. This data can be converted to volume change through calibration, from which the change of degree of saturation can be computed. In the dry specimen, a package of Labview tool kit (Figure 4.5) provided by Teledyne Isco is used to measure the change of soil

volume and export the data. The data acquisition system along with the DPT and the Labview tool kit enables a compact control and DAQ environment for the experiment.

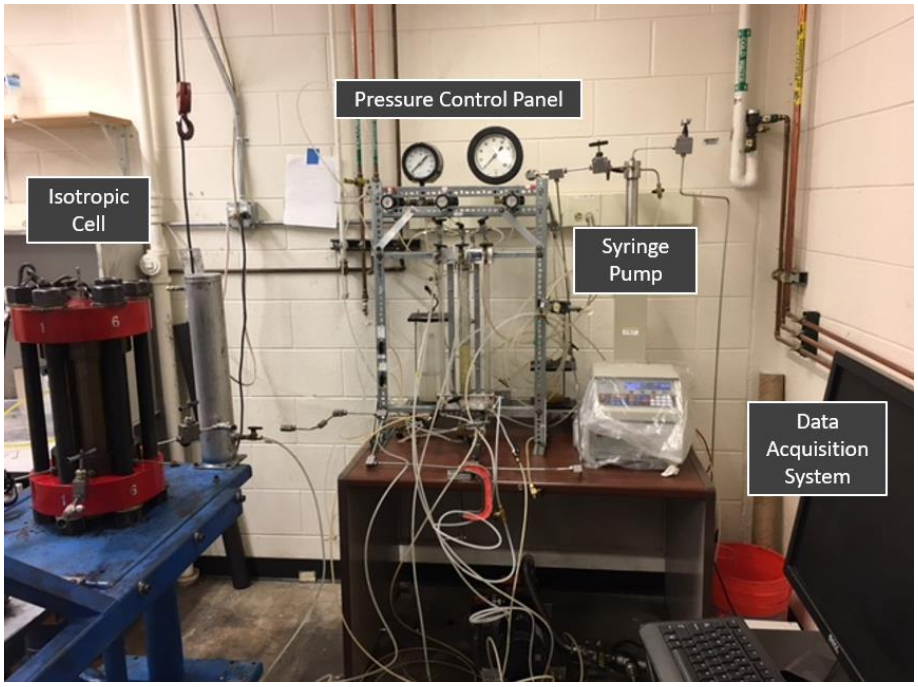

Figure 4.1: Picture view of HPIC

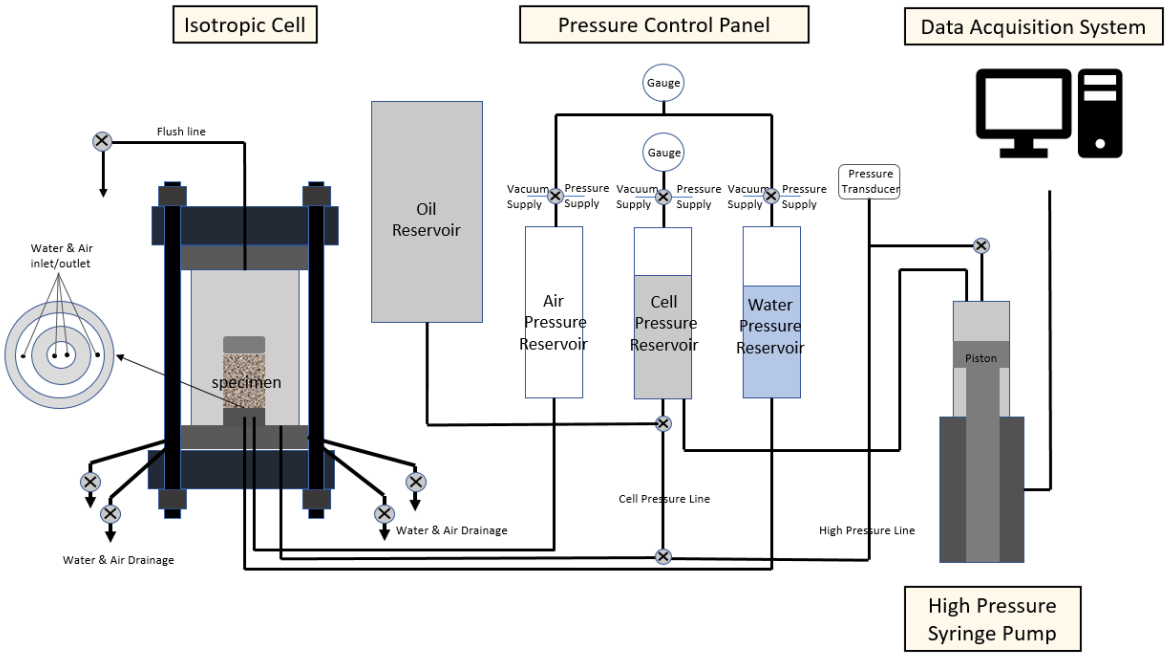

Figure 4.2: Schematic view of HPIC

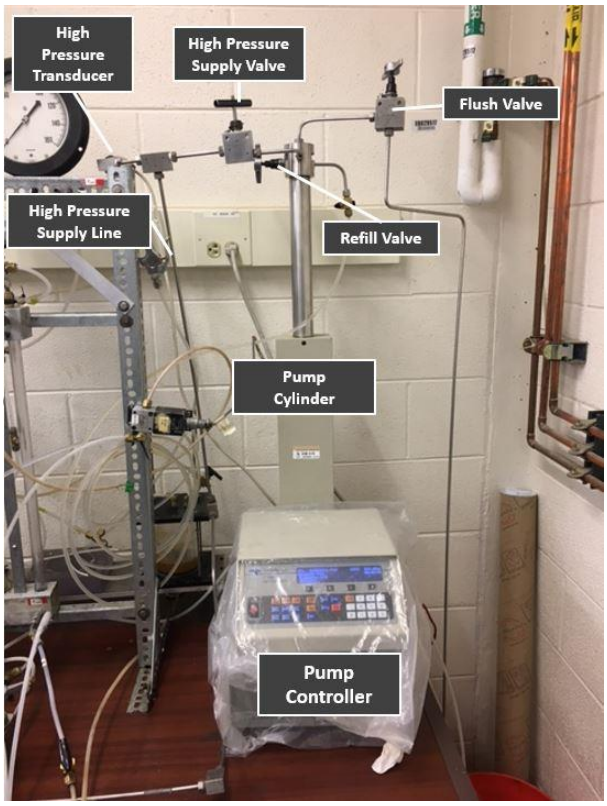

Figure 4.3: Picture view of syringe pump

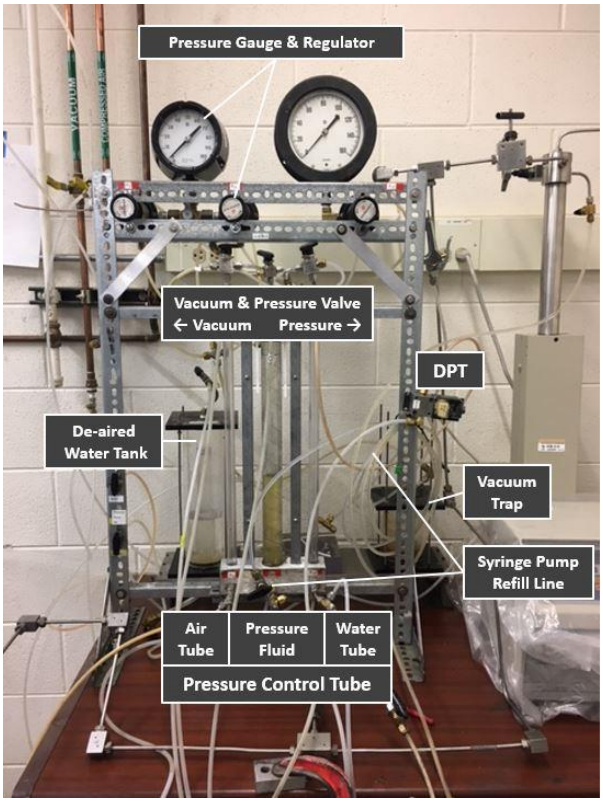

Figure 4.4: Picture of pressure control panel

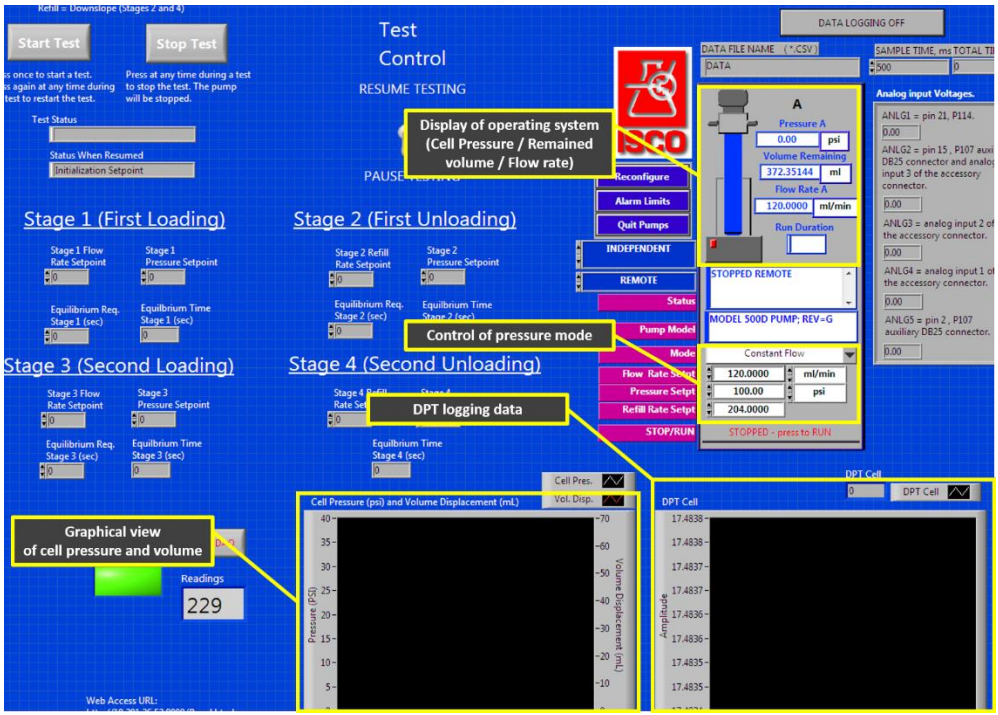

Figure 4.5: Toolkit

Table 4.1: Details of the syringe pump

Pressure range	0.07 ~ 165 MPa
Cylinder capacity	68 mL
Flow rate	0.00001 ~ 25 mL/min
Flow accuracy	± 0.3% of set point
Dimensions	103 × 27 × 45 (cm)

The isotropic cell is made of a 254mm tall, 180.34mm OD and 112.78mm ID stainless-steel cylinder sandwiched by two 50.8mm-thick plates. A bottom plate with a thickness of 38.1mm and a diameter of 71.1mm for placing specimen is integrated with the bottom part of the cell. Figure 4.6 shows inside and outside view of the isotropic cell. A load frame with 76.2mm thickness of stainless steel plate and six steel alloy rods was installed to resist high pressure within the cell. A torque of 2,983 N·m is applied to the rods of the load frame to avoid leakage by high pressure. In the top plate, a flush valve is connected to allow air to be evacuated when pressurizing fluid is being filled. The cell has four ports in use of inlet and outlet for both drainage of water and air. A fifth port is used to supply the pressurizing fluid into the cell.

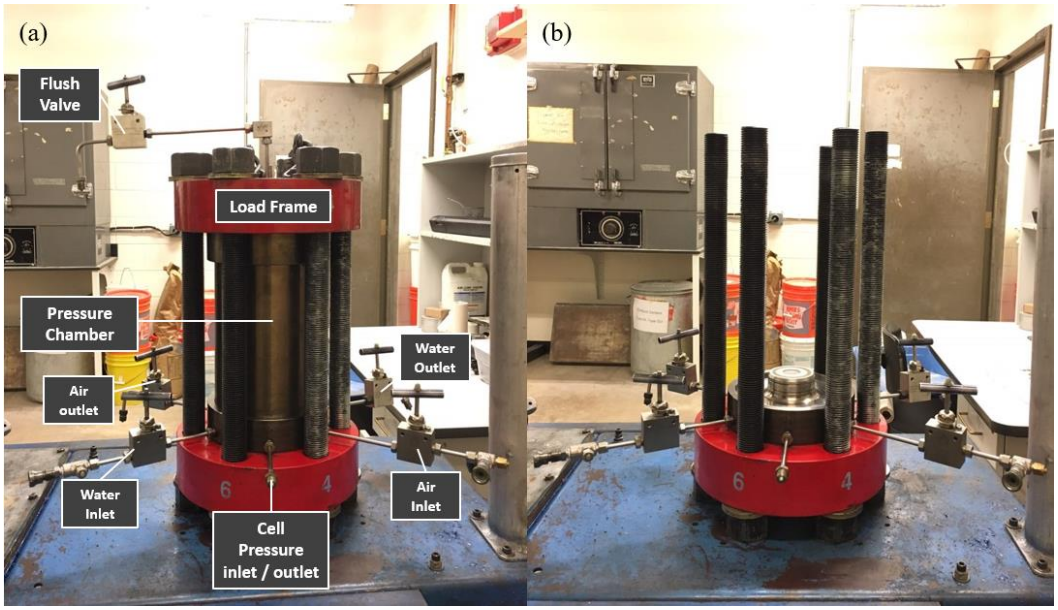

Figure 4.6: (a) Inside view of isotropic cell; (b) Outside view of isotropic cell

Figure 4.7 (a) shows the bottom platen of the cell. The specimen exchanges air and water with the external burette via a porous sintered stainless ring at the center and edge of the plate. There are 4 holes with diameter of 1.59mm hidden beneath the ring [Figure 4.7 (b)]. At the center of the bottom plate, either a ceramic disk or a sintered porous disk can be placed, to make this part drains water only or both water and air. Cell pressure is applied on the pressure fluid through a hole near the bottom plate.

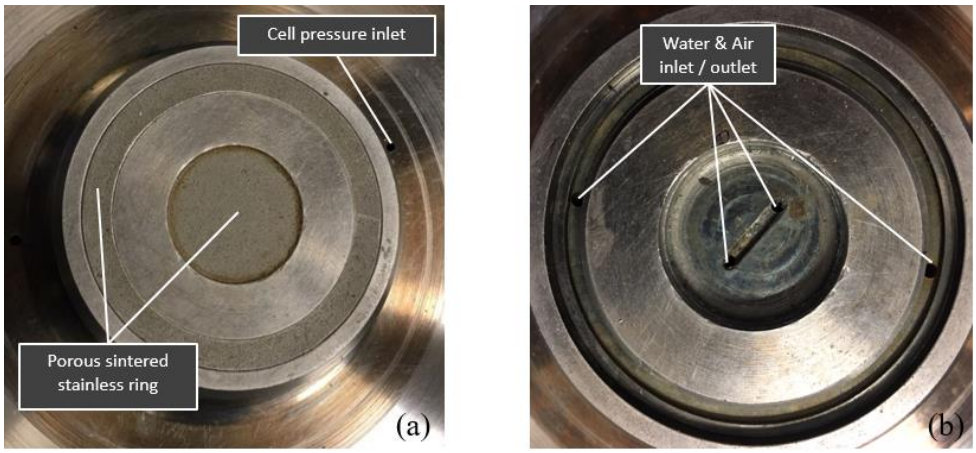

Figure 4.7: (a) View of the bottom plate; (b) Inside view of the bottom plate

4.2. System Calibration

To measure volumetric strain of the specimen during compression through the syringe pump reading, the machine compliance was measured using an aluminum specimen with Young's modulus of 69 GPa and Poisson's ratio of 0.334 as shown in Figure 4.8. The aluminum specimen was machined to diameter of 70mm and height of 71.4mm, which matches with the dimensions of the soil specimens. To replicate the exact testing conditions, the cylindrical aluminum was wrapped with all the sealing materials in the same way at the actual testing. The prepared aluminum specimen was subjected to an isotropic loading and unloading cycle from 0 to 160 MPa under flow rate of 5mL/min. Three times of machine compliance test were conducted and their average has been adopted for calculating the volumetric change due to

machine compliance. The averaged curve is plotted in Figure 4.9. The real volumetric strain of a soil specimen can be computed by subtracting the measured volume change by the machine compliance curve.

Figure 4.8: Aluminum specimen

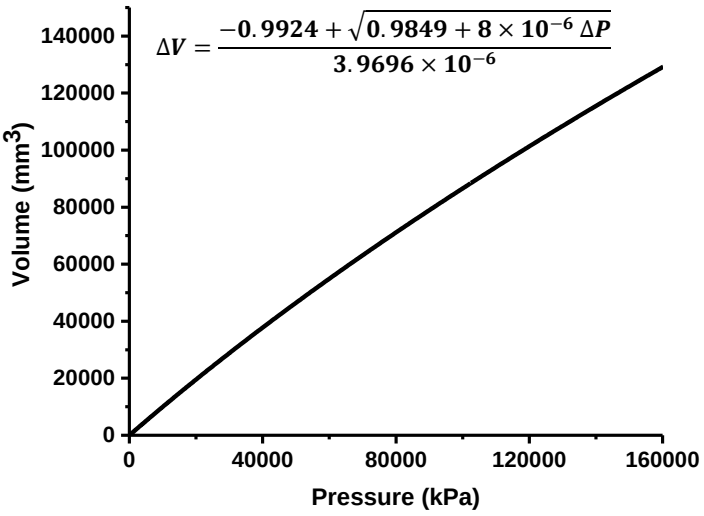

Figure 4.9: Machine compliance curve

CHAPTER 5: TROUBLESHOOTING AND PROTOCOL DEVELOPMENT

5.1. Attempts for coupled HPIC and SWRC tests

5.1.1. Original plan of the experimental study

The original goal of this study is to analyze the hydromechanical properties of granular soils by obtaining their water retention curves and compression response simultaneously using the HPIC. This was motivated by the fact that the HPIC device has the potential to fragment the soil specimen and impose suction control at the same time. If successful, this is a significant step forward compared to the study by Gao et al. (2016), where the compression and SWRC experiments have been conducted in separate devices. During this process, the samples has been reconstituted, thus the in-situ fabric structures of loaded specimens are invariably lost during the measurements of SWRC. Moreover, since the soil water retention test were performed after the 1-D compression, the impact of desaturation or re-saturation on the possible collapse behavior of soils cannot be studied. In this study, attempts have been made to address the issues in Gao's study using the HPIC device.

5.1.2. Limitations of SWRC test using HPIC

To check the feasibility of HPIC for measuring the SWRC of stressed soil specimen, a trial test was conducted. Low isotropic pressure was applied by pressure panel and suction is applied by pressurizing the air through the porous ring. Water in the specimen was allowed to be drained through the porous ceramic disk with air entry value of 300kPa. Figure 5.1 presents the setting of the trial test. At the same time, independent SWRC tests were conducted using the Tempe cell setup (Soilmoisture, Goleta, CA) which is widely used for studying the retention properties of coarse granular materials (Figure 5.2). Two tests were carried out using uniform quartz sand and the degree of saturation was measured every 4 hours to allow for equilibrium.

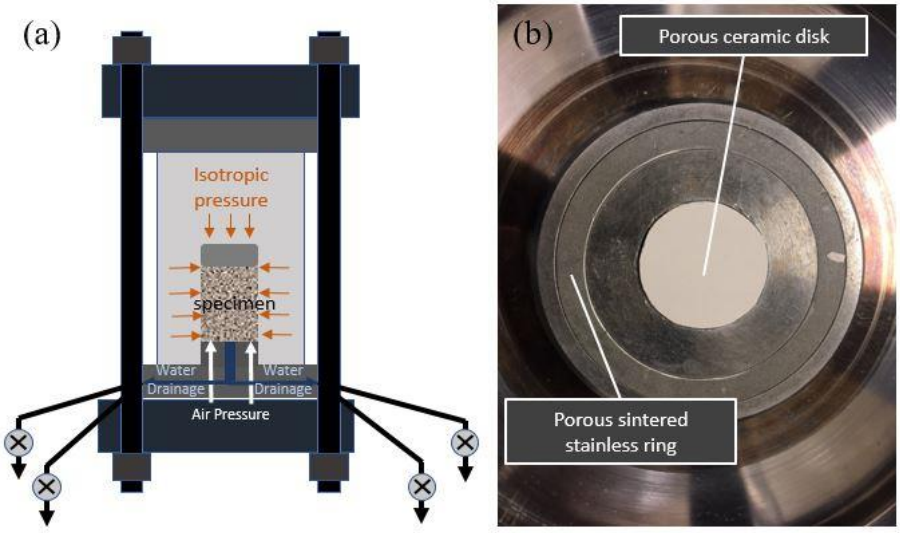

Figure 5.1: Experimental setup for SWRC test with HPIC: (a) Sketch of the test; (b) picture of the bottom plate

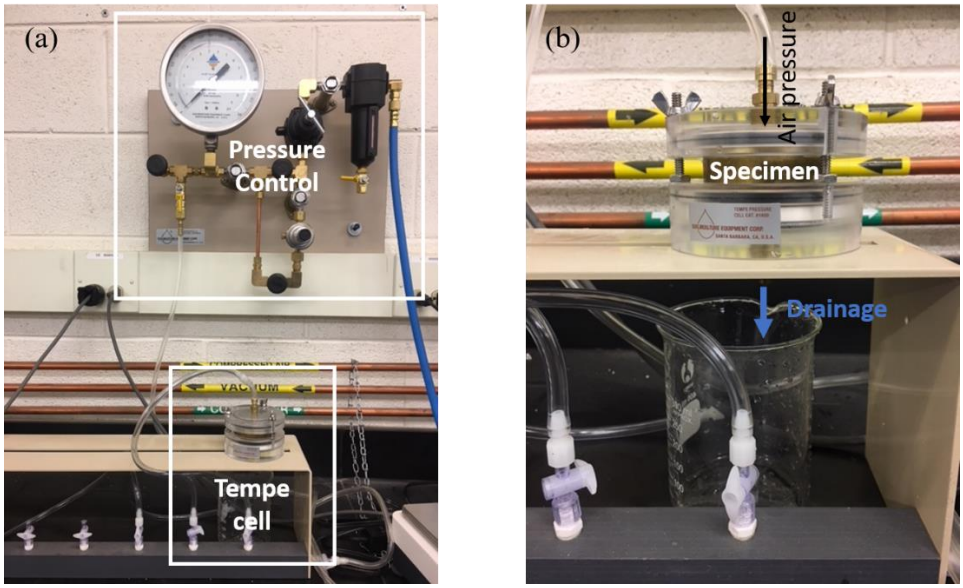

Figure 5.2: (a) View of Tempe cell; (b) Operation of Tempe cell test

As shown in the plot with Tempe cell test [Figure 5.3 (a)], the tested sand has extremely low water retaining capability which approaches to the lower limitation of the measurement range of the Tempe cell system. The SWRC measured by the HPIC [Figure 5.3 (b)], however, is located at much higher suction ranges. Even with such a high pressure of 100kPa, just approximately 20% amount of water was drained out. This massive disagreement indicates that

the HPIC device is not suitable for SWRC measurements and further implies its inefficiency in controlling suction during the mechanical test.

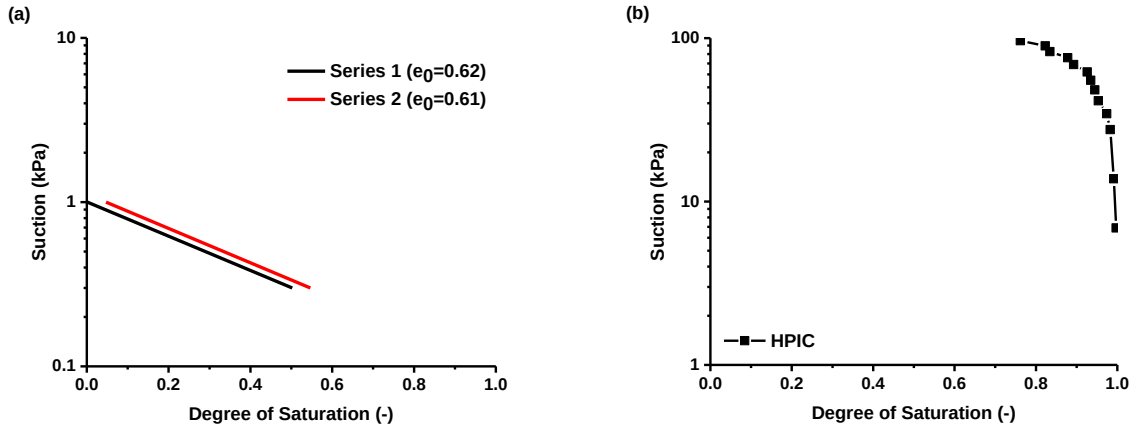

Figure 5.3: SWRC test results by (a) Tempe cell; (b) HPIC

The reason for such mismatch of the SWRC obtained from HPIC and Tempe cell is that the HPIC does not have an optimal drainage flow configuration for equilibrium. The air pressure is applied upward through bottom of the cell but the HPIC let water drain out downward [Figure 5.4 (a)]. This pressure applying and drainage flow direction is not the same as the Tempe cell, where water is drained from the bottom and air pressure comes from the top of the cell [Figure 5.4 (b)]. Another reason is in the time duration between each measurement. Since the sample volume for the HPIC test is greater than that for the Tempe cell, equilibrium time for the HPIC specimen need much longer time than 4 hours which is considered enough for the Tempe cell test. The last reason for the inapplicability of HPIC for SWRC measurement is that, after each high-pressure compression test, the porous ceramic is severely compacted and indented by the soil particles. This can cause void closure, damaging, and cracking of the ceramic and make it lose functionality.

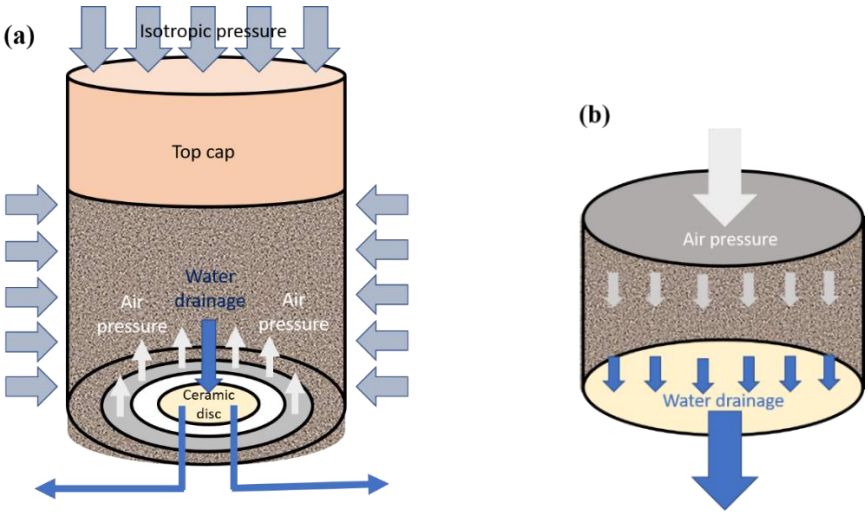

Figure 5.4: A schematic view of flow direction of air pressure and water drainage: (a) HPIC; (b) Tempe cell

There are several possible solutions to reconfigure the HPIC device suitable for the SWRC test: 1) Design air pressure line that goes through the top of the HPIC and replace the porous steel with the ceramic can establish similar air pressure and water drainage system as the Tempe cell; 2) Use porous ceramics that are characterized by low suction air entry values to enhance the water flow rate and reduce the time required for equilibrium; 3) To prevent damage and contamination of the porous ceramic disc, it is possible to place a porous steel disc on top of the ceramic disc, which is supported by the surrounding walls rather than the ceramic directly. In this way, the ceramic does not contact with the soil nor take the confining pressure from the soil specimen. Thus, both indentation and compaction can be prevented.

5.2. New plan of the study

Knowing the above experimental limitations, the direction of this study has been modified to focus more on the mechanical properties of coarse granular materials. Since the HPIC is still fully adequate in supplying high pressures and causing particle breakage, a study of the co-evolution of compressibility and gradation can be carried out using the device. This study will compare the compressive curve, grain size distribution and breakage evolution curve for

four different crushing stress level at 20, 40, 80, and 160MPa, to explore how particle breakage is developed through the course of isotropic compression. The extent of breakage at each crushing stress will be evaluated based on the Einav's breakage index. Furthermore, the effect of saturation on compressive behavior in quartz sands will be investigated.

The HPIC device has to be adapted for the new purpose. The porous ceramic disk, used for suction control in the previous plan, is replaced with porous metal to guarantee more effective drainage during compression and better mechanical support to the soil specimen. The modified system allows the measurement of the compressive deformation immediately by getting rid of the equilibrium time imposed by the ceramic disk. The modified porous system is presented in Figure 5.5.

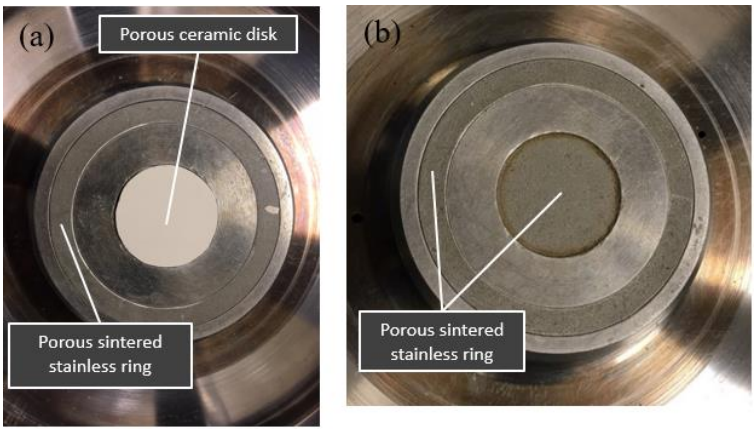

Figure 5.5: (a) Initial setting of bottom plate; (b) Current setting of bottom plate

During the HPIC test on quartz sands, difficulty raises in sealing to prevent leakage of the pressure fluid into soil specimen. There has been a lot of trials and troubleshooting for finding a way of sample preparation without leakage. In the early trials, samples were prepared using one piece of latex membrane (thickness: 0.635mm) for confinement of the specimen, two o-rings on grooved bottom plate and top cap for fixing the membrane, and vacuum grease on top cap and bottom plate to provide extra sealing. To make the initial sample perfectly cylindrical for precise

measurement of initial void ratio, a vacuum is applied after the membrane is wrapped inside of a cylindrical PVC mold. A picture view of the sample of the first setting is presented in Figure 5.6. This setting, however, does not provide a sealing strong enough to endure the high pressure during the test. The first problem was that pressure fluid seep into the specimen through the small gap between membrane and top cap or bottom plate. The second problem was that the latex membrane is easily punctured by asperities of the quartz sand, permitting fluid exchange between the cell and inside the specimen. To settle these issues, the latex membrane was replaced by the neoprene membrane (thickness: 0.635mm), customized by Geotac in Houston, TX to provide higher rupture resistance. Besides, o-rings with smaller diameter were used to provide stronger sealing at the top and bottom as shown in Figure 5.7.

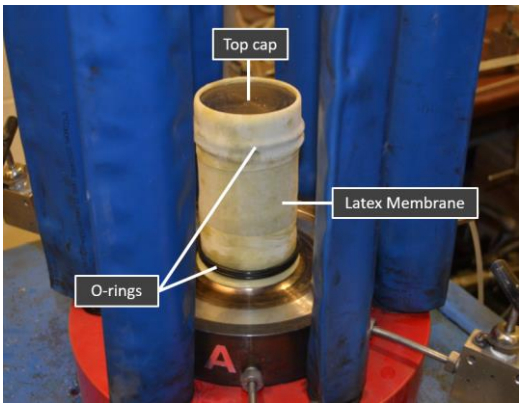

Figure 5.6: Initial sample setting

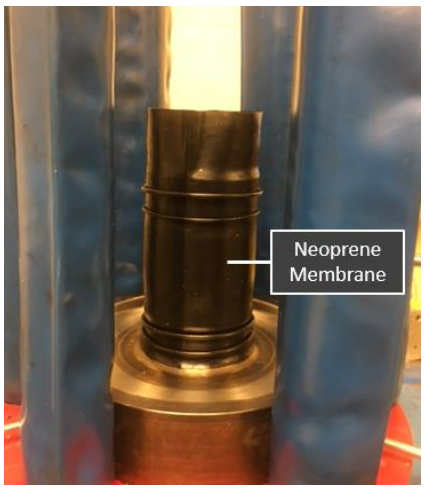

Figure 5.7: Setting with neoprene membrane

The new configuration still did not completely prevent the leakage. Even though smaller o-rings can keep the pressure fluid from seeping into the specimen, the neoprene membrane was penetrated again at pressure higher than 50 MPa. Some brief literature review soon revealed that similar failure has occurred in other experimental studies with high confining pressures (Vesic and Clough, 1968; J. Colliat-Dangus et al., 1988; Yamamuro and Lade, 1996). Yamamuro and Lade (1996) used five pieces of latex membrane with 0.64mm thickness for avoiding

penetration, Vesic and Clough (1968) employed plasticized polyvinyl chloride membrane of 1.3mm thickness for testing sand typed soil at high pressure up to 63 MPa, and Colliat-Dangus et al. (1988) used two pieces of neoprene membrane having 0.5mm thickness for higher than pressure of 5 MPa.

To exercise similar methods, we have used 3 pieces of latex membrane (thickness: 0.635mm) and one piece of neoprene membrane (thickness: 0.635mm) to prepare the specimen. Directly attaching the membranes to the mold can make it difficult to have a cylindrical sample, which is important to measure the initial void ratio. The multiple layered membranes were hardly attached to the wall of mold when subjected to vacuum suction. To solve the problem, the aluminum specimen, which had been used for work of machine compliance, was used as a guide of pushing the membrane to the wall. After piling the metal specimen with all the membranes, the aluminum cylinder is pushed into the mold and the membranes are left at the end of two sides to the mold. Then the vacuum suction is applied and the aluminum cylinder is gently removed. Finally, an ideal cylindrical inner wall is formed. Figure 5.8 describes the procedure. After the

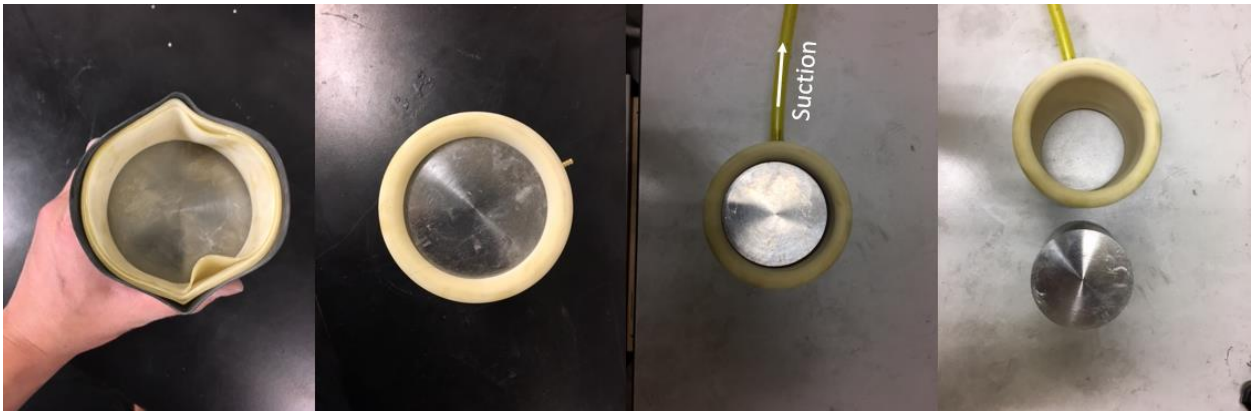

Figure 5.8: Procedure of sample preparation in order from left to right

sample is filled, three and two o-rings (O.D.: 61.91mm and I.D.: 57.15mm) are installed on the top and bottom cap, respectively (Figure 5.9). The three latex membranes have the role in

cushioning the sharp sand grains and prevent the penetration of neoprene membrane during high pressure tests. Finally, this sealing method is successful in preventing leakage and all the experimental results presented in this thesis are obtained using this method.

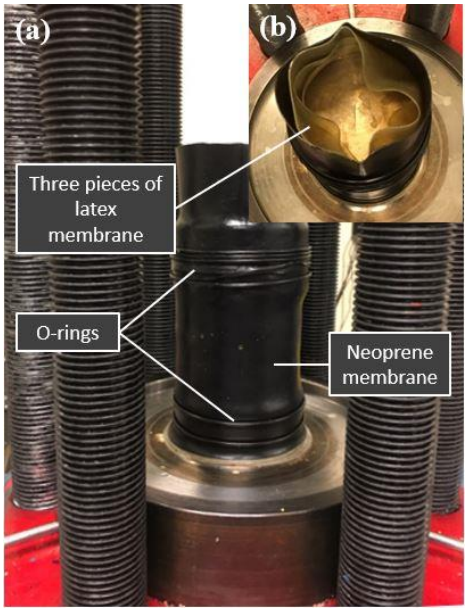

Figure 5.9: Determined setting for sample preparation: (a) View from side; (b) View from above

5.3. Troubleshooting on DPT and DAQ system for measuring water outflow

As referred in the introduction of HPIC, a differential pressure transducer (DPT) attached to the water burette is responsible for tracking the volume of water outflow from the specimen. However, it is found that although pore water comes out to the water burette, electrical output is constant as almost zero in the DAQmx program. A troubleshooting for DPT has been conducted using DC power supply (PS 280 produced by Tektronix) device, which is able to check if an electrical device has malfunctions. In a properly working device, output voltage should be almost consistent with the input voltage but have a tiny electrical current. The DPT shows a consistent value between output and input as shown in the Figure 5.10. Therefore, it is concluded the DPT is working properly.

The DAQ system is consisted of four electrical modules, SCXI 1001, SCXI 1600, SCXI 1121, and SCXI 1320 (Figure 5.11). The SCXI 1001 is the chassis where multiple modules can be installed. The SCXI-1600 is a module featuring data acquisition and providing sub-SCXI (SCXI 1121 in the system) analog input, analog output, digital I/O. The SCXI-1121 can control and separate signal input for each channel, which requires different input signals in a variety of use. The SCXI 1320 receives signal input from the DPT.

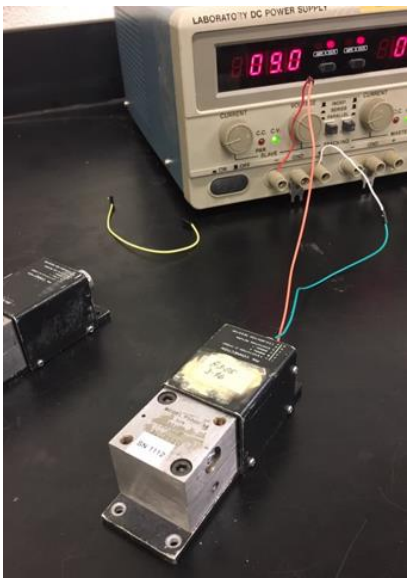

Figure 5.10: DPT debugging

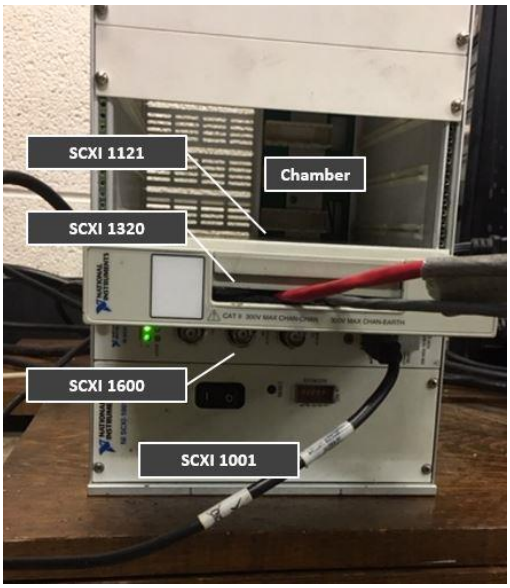

Figure 5.11: Composition of DAQ system

Troubleshooting was performed for the two modules with or without the involvement of the DPT using a multimeter. All the parts, except for SCXI 1121, has reasonable value of electric voltage output. In the case of SCXI 1121, negligible voltage output is observed when the DPT is connected, whereas it has an acceptable voltage output without the DPT (Figure 5.12). Based on this observation, it is suspected that the module is unable to send a required voltage to operate DPT, and the SCXI 1121 contains malfunctions in supplying sufficient input voltage to the DPT.

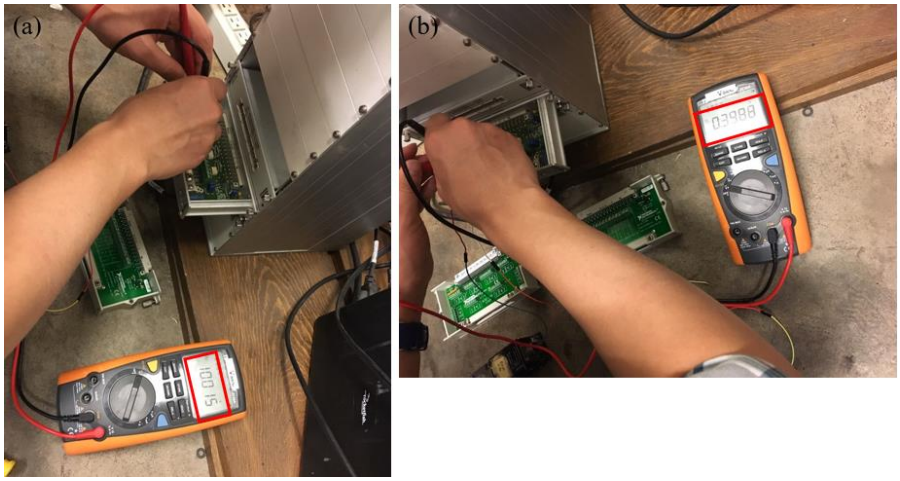

Figure 5.*12: Data acquisition system troubleshooting: (a) connected with DPT; (b) disconnected with DPT*

5.4. Failure of the bolts connecting the isotropic cell and its top plate

Disassembly after test and assembly before test of the HPIC cell requires an action of uplifting the cell with a pulley. The uplifted parts are hereafter referred to as HPIC cover for convenience. The HPIC cover consists of the load frame, the isotropic cell, and the top plate, which has a role in connecting the other parts of the HPIC cover (Figure 5.13). The parts are connected by a socket head screws in each section. The socket head screws for connecting between the top plate and the load frame are larger and made with alloy, while the screws between the cell and the top plate are smaller and made with stainless steels. Figure 5.14 shows view of each socket head screws.

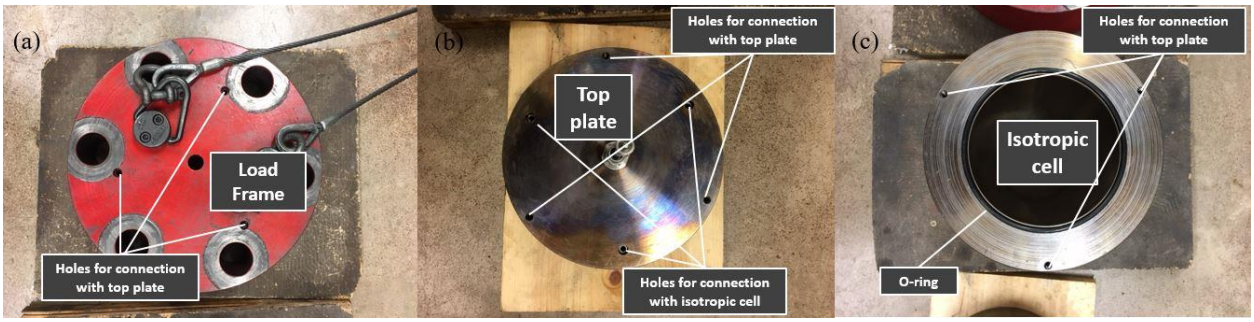

Figure 5.13: Composition of the HPIC cover: (a) Load Frame; (b) Top plate; (c) Isotropic cell

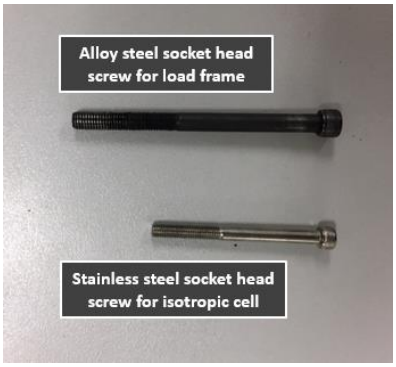

Figure 5.14: Socket head screws for load frame (above) and for isotropic cell (below)

A problem encountered in many HPIC tests is the failure of the stainless socket head screws and consequently the disconnection between the cell and the top plate. The main mechanism that causes such failure is that the cell-top plate connection is one of the weakest links of this cell design. A schematic view of the HPIC cover is shown in Figure 5.15. It can be seen that during a HPIC test, pressures transmitted to the top plate is balanced by the tensile stress carried by these three small bolts as well as the six outer rods. After the test, lifting up the entire cover also counts on the tensile stress in the bolts to carry the weight of the isotropic cell. Therefore, fatigue tensile failure of theses screws is promoted during the numerous high-pressure tests and uplifting/release of the cover. It is well known that mechanical properties of alloy are better than stainless steel in terms of shear strength and tensile strength [Machine Design, (http://www.machinedesign.com/materials/comparing-stainless-steel-and-other-metals)]. The specification of the alloy and stainless steel are detailed in Table 5.1. These screws are changed to those made with alloy steel, which has demonstrated a decreased probability of failure.

Table 5.1: Mechanical properties of the screws by composition

Material	18-8 Stainless steel	Alloy steel
Tensile strength (psi)	70,000	170,000
Shear strength (ksi)	N/A	11,000

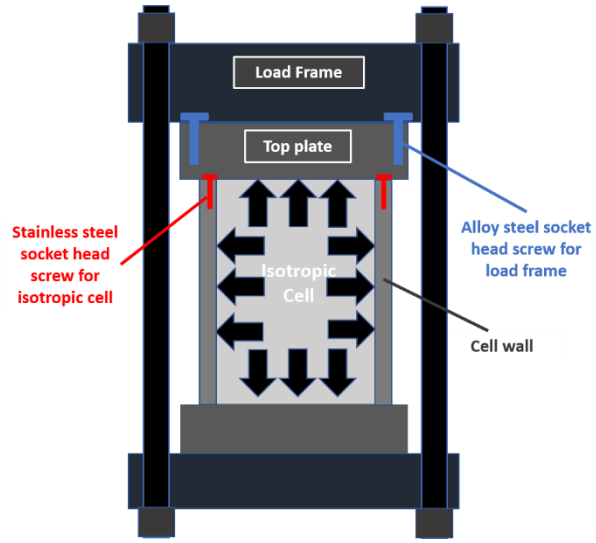

Figure 5.15: Schematic view of load transition for screw failure

CHAPTER 6: EXPERIMENTAL RESULTS

6.1. Details of specimens and experimental works

In this study, quartz sand and shale sand are crushed using the HPIC device. The quartz sand is pool filter sand produced by the Quikrete. The sand is uniformly graded and has a grain size ranging from 0.118mm to 2.00mm. Shale obtained from Boulder, Colorado has been used to produce the shale sand. To minimize grain size effect on particle breakage, the shale rock is milled and sieved to have the similar gradation with the quartz sand. The produced shale sand is also uniformly graded and most of them has a grain size ranging from 0.85mm to 2.00mm. The quartz sand is sub-rounded while the shale sand is angular. Figure 6.1 (a) and (b) present the microscopic view of their particles. Figure 6.2 (a) and (b) shows pictures of the two sands.

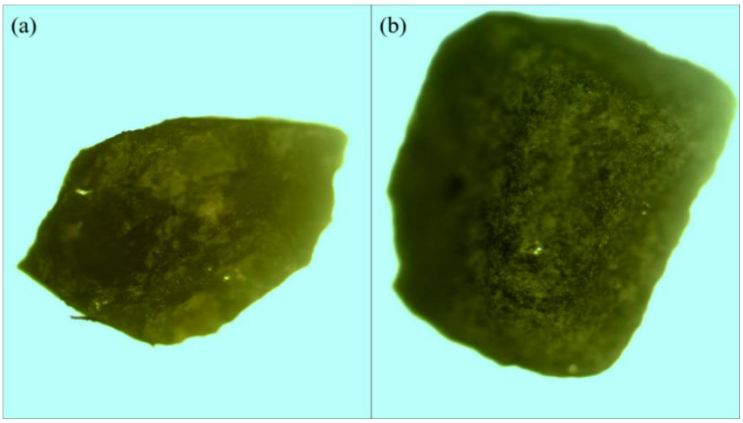

Figure 6.1: Microscopic view of the (a) quartz sand; (b) shale sand

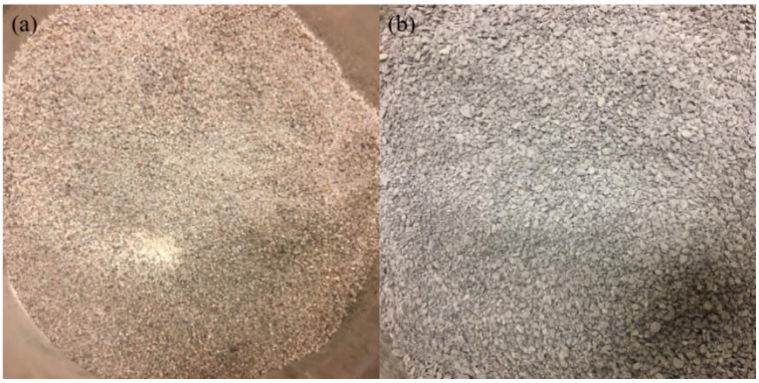

Figure 6.2: Pictures of the (a) quartz sand; (b) shale sand

Before each test, the specimens are oven dried to remove the residual moisture. The volume of soil used for each test are made identical to ensure the same initial void ratio. For test on saturated specimen of the quartz sand, the samples are prepared through wet pluviation. De-aired water is applied through the bottom of the cell driven by vacuum applied at the top of the sample using a saturation cap. For tests on saturated shale sand, the grains were submerged in water for 3 days before the wet pluviation procedure since more saturating time is needed for shale sand. Specific gravity tests are conducted to accurately calculate initial void ratio. The obtained initial void ratio is 0.63 – 0.64 for quartz sand and 0.71 for shale sand. The volume of the test sample (D: 72.8mm H: 66.05mm) is same as the aluminum specimen used for machine compliance measurement. The index properties of the specimens are detailed in Table 6.1.

Table 6.1: Index properties of specimens

Property	Quartz sand	Shale sand
D_{10} (mm)	1.07	0.9
D_{30} (mm)	1.32	1.2
D_{60} (mm)	1.61	1.7
Percent fines (%)	0.15	0.7
Coefficient of uniformity, C_u	1.55	1.89
Coefficient of curvature, C_c	0.99	1.06
Specific gravity, G_s	2.67	2.29
Liquid limit (LL)	-	24
Plastic limit (PL)	-	26
Plasticity index (PI)	-	Non-Plastic (NP)
Minimum void ratio, e_{min}	0.59	0.67
Maximum void ratio, e_{max}	0.68	0.73

Compression tests are performed on dry quartz sand terminated at four different pressure levels at 20, 40, 80 and 160 MPa. For the purpose of finding difference in compression behaviors between wet and dry state of crushable granular materials, 160 MPa compression tests are

conducted for fully-saturated and oven-dried quartz sand and shale sand. The dry and saturated specimens are pressurized by a constant flow rate of 5ml/min and 1ml/min (to minimize pore water build-up), respectively. Brake fluid is used as the pressurizing fluid for its high bulk modulus (2.068 GPa). The quartz sand specimens after compression tests are subjected to particle size analysis. Wet sieve analysis with No. #200 (0.075mm) sieve was performed to collect and detach fine particles stuck to the body of larger particles. Hydrometer analysis are conducted for the fines collected after the wet sieve analysis. The remaining particles on the No. 200 sieve are subjected to regular sieve analysis with No.10 (2mm), No.16 (0.118mm), No.20 (0.85mm), No.40 (0.425mm), No.50 (0.3mm), No.60 (0.25mm), No.80 (0.18mm), No.100 (0.15mm), and No.200 (0.075mm) sieves. The grain size distributions for all the quartz sand specimen under the different compressive stress are plotted. However, the sieve size analysis is not available for shale sand due to solidification of the specimen after the compression.

6.2. Compression curve

6.2.1. Compression curve for dry quartz sand under the different stress

The results of isotropic compression curve for dry quartz sand under 20, 80 and 160 MPa stress levels are plotted in the Figure 6.3. In each figure, except for 20 MPa, the curves have two or three of discontinuous points due to the refilling process. Since the pump has a maximum volume storage of 68mL, it needs to be refilled frequently for high-pressure tests and for highly deformable soil specimens. During refilling, it is difficult to avoid slight pressure relaxation due to material creep effect and fluid loss during valve opening/closing. Such minor unloading event does not affect the observation of the overall compression response at the post-crushing regime. The compression curve for all the stress have a similar result, justifying the repeatability of the sample preparation and loading procedure. The yielding point of the 20 MPa curve is slightly

earlier than the others, possibly due to the initial variation of the sample. The compression curves in log-linear plot exhibits two distinct slopes before and after yielding, which corresponds to the linear elastic response and the clastic hardening response. This is typical for crushable granular soils and the yielding is uniquely corresponding to the onset of grain breakage.

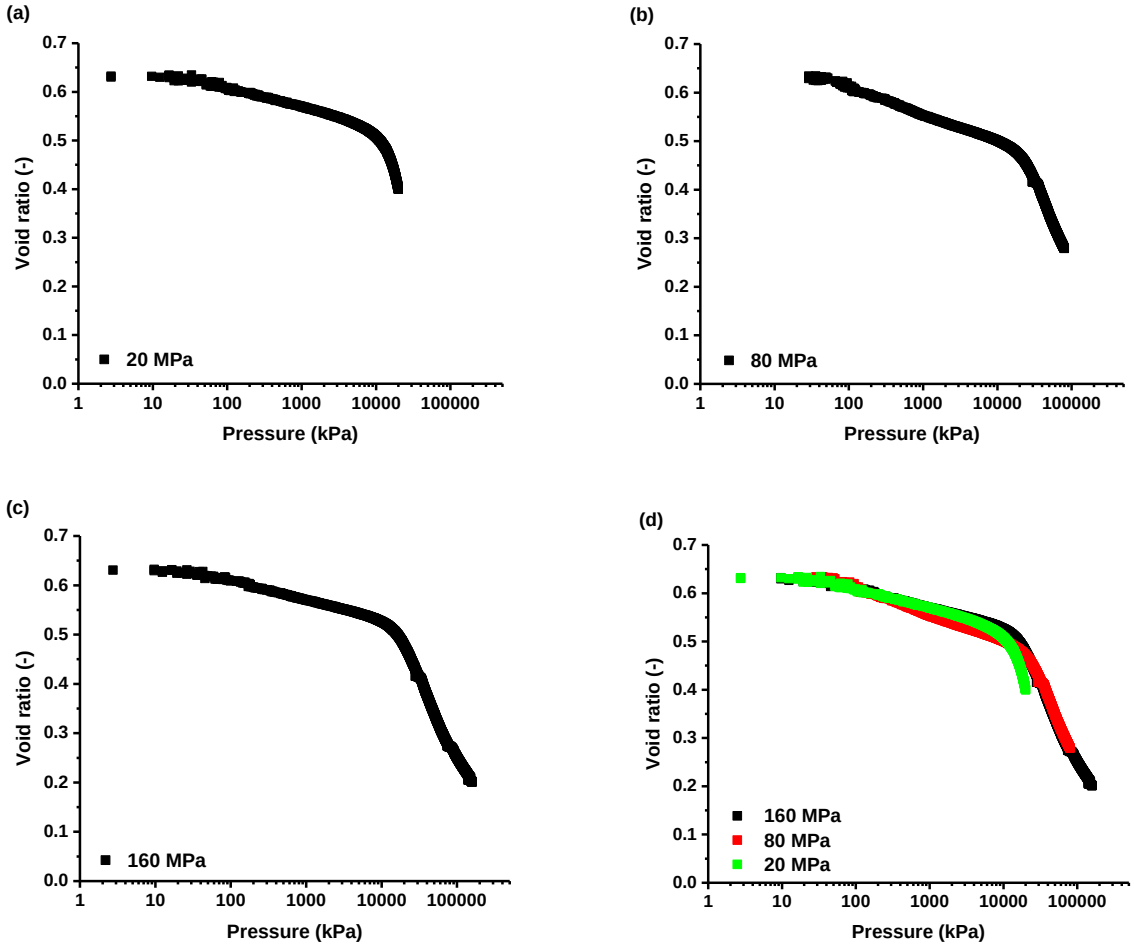

Figure 6.3: Compression curve for dry quartz sand at the different stress levels: (a) 20 MPa; (b) 80 MPa; (c) 160 MPa; (d) Integrated plot of the curves

Hereafter, the compression behavior of the quartz sand will be analyzed with reference to the 160 MPa compression curve in Figure 6.3 (c). It is observed that yielding occurs at the pressure of 16 MPa, which is higher than the yielding stress of Mason sand (Mun and McCartney, 2017). This means the crushing resistance of the quartz sand is higher than the Mason sand. High compressibility in the post-yielding is observed with the steep slope of the

normal compression line. Void closure was observed for the Mason sand, indicated by the flatten out of the compression curve at high pressures. Such phenomenon was not observed for the quartz sand tested in this study, meaning active voids still exist at 160 MPa.

6.2.2. Comparison between quartz sand and shale under dry and saturated condition

The compression curves of quartz sand and shale sand with dry and saturated condition are presented in Figure 6.4. In the Figure 6.4 (a), different initial void ratio causes slightly misalignment of the compression curves in the elastic regime. However, these curves converge to a single limiting compression curve (LCC) after yielding and it is consistent with the previous studies (Hendron, 1963; Lee and Seed, 1967; Golightly, 1989; Pestana and Whittle, 1995; Mun and McCartney, 2017). The quartz sand shows identical post-yielding compression behavior despite the different saturation condition and initial void ratio. Thus, it is concluded that the water saturation does not significantly change the compression behavior of the quartz sand.

On the other hand, it is observed that water has a significant impact to the compression behavior of shale sand. The saturated specimen is more compressible and thus void collapse and yielding occurs at much lower stress levels than the dry one. This finding is consistent with other studies that shale sand and rockfills with higher moisture content is more compressible and crushable (Oldecop and Alonso, 2001; Ovalle et al., 2013). This phenomenon can be also emphasized in terms of relative humidity. Increased relative humidity corresponds to decreased suction at the micro-fissure in particles, which further promotes the dissemination of cracks and degradation of particle strength (Oldecop and Alonso, 2007). Such water sensitivity of shale can be also attributed to the high content of clay minerals which can exhibit slaking, swelling and softening upon water saturation (Botts, 1998; Claybourn 2007). On the contrary, the quartz sand

is mainly consisted of quartz which has much less interaction with water molecules. Therefore, the water weakening effect is more pronounced on the shale sand than the quartz sand.

Further inspection of Figure 6.4 (a) shows that the compression curve of the quartz sand shows a sharp and clear transition at the yielding point, while such transition is much more gradual for shale sand. This difference can be explained in terms of the brittleness of their constituting grains. The quartz sand particles are very brittle. Once they are stressed beyond the breakage threshold, catastrophic fracturing and comminution occurs macroscopically as the sharp yielding point. On the other hand, the failure of the shale particles is gradual and involves local plastic deformations at the grain-to-grain contacts. Particle breakage does not occur immediately after yielding but rather happens after sufficient plastic strains developed. This prolongs the elastic-plastic transition as many particles undergoes different phases of failure at microscopic level in this regime.

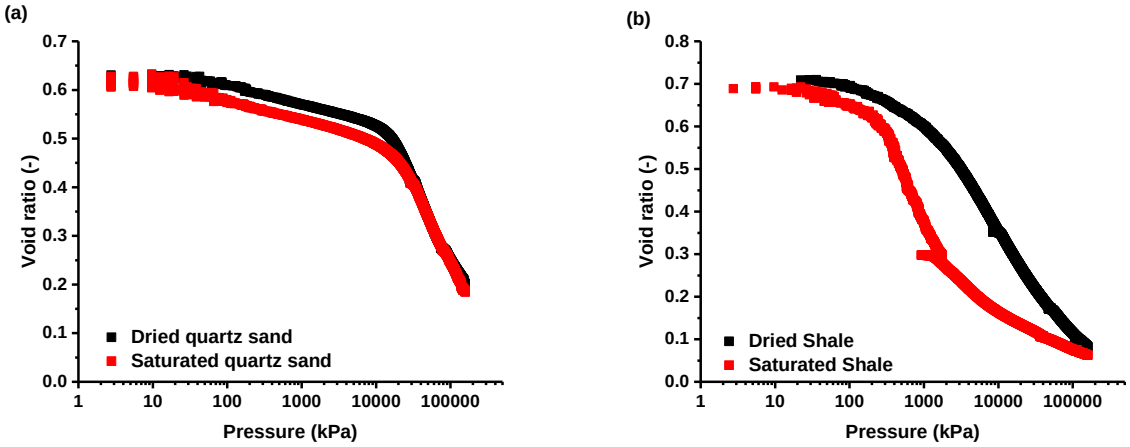

Figure 6.4: The compression curves of shale sand and quartz sand with the different saturated condition: (a) quartz sand; (b) shale sand

During testing shale sands, it is noted that there is a significant amount of stress relaxation developed during refilling of the syringe pump. To analyze an effect of saturate condition on the relaxation, the developed stress drops in each refill time for saturated shale sand

and dry shale sand are compared. Since more stress drop is developed at a refill with higher pressure, using the actual amount of stress drop does not facilitate a direct comparison for the ability of the material to relax. Thus, the relaxation stress is normalized by the stress level at which such relaxation is conducted as $N_r = \frac{dP\ (stress\ drop)}{P\ (stress\ at\ the\ refill)}$. The normalized relaxation curves of the shale sand, quartz sand and the machine compliance are compared in Figure 6.5.

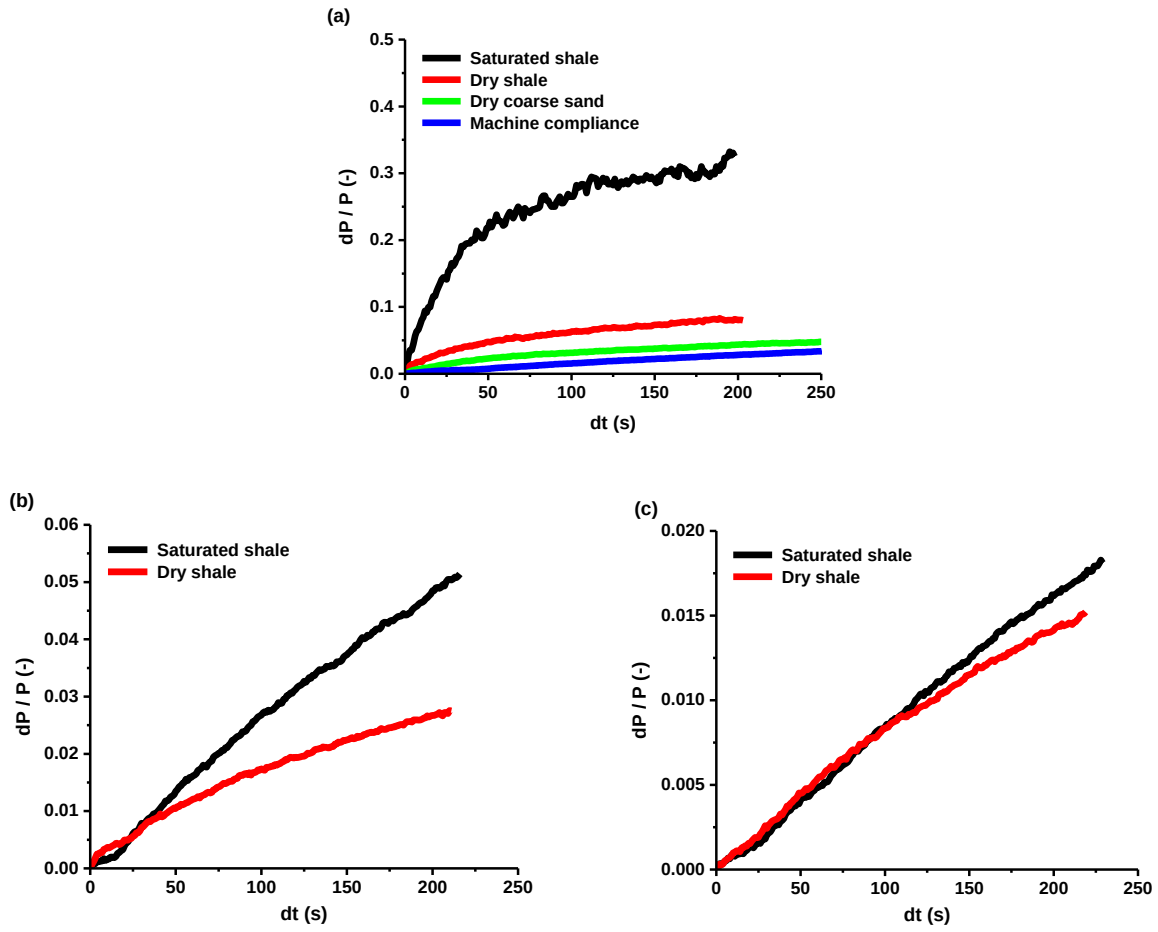

Figure 6.5: Comparison of normalized relaxation on the saturated shale sand and dry shale sand: (a) at the 1st refill time along with the one of dry quartz sand and machine compliance test; (b) at the 2nd refill time; (c) at the 3rd refill time

It is evident that more relaxation is evolved in the saturated shale sand. This can be explained by the amplified time-dependent behavior of the shale sand at high water content. Ovalle et al. (2013) conducted a series of triaxial tests were conducted to evaluate the wetting

condition effect on relaxation and creep. They have reported greater deviatoric stress dropped in the relaxation test and creep straining in the creep test for wet specimen as compared to dry specimens (Ovalle et al., 2014). These results are consistent with the finding. Moreover, it is observed that shale sands are overall more time-dependent than the quartz sand due to the rich clay content as discussed previously. Relaxation curve from the machine compliance tests is also plotted in Figure 6.5 (a) to indicate the relaxation contribution due to possible leakage at connections and valves.

In summary, comparing the compression curves between the dry sand fully saturated sand, it is found that: 1) saturated shale sand has higher compressibility before and after yielding; 2) saturated shale sand has lower yielding stress; 3) saturated shale sand exhibit void-closure effect at high pressure levels; 4) saturated shale sand has more stress relaxation than dry shale sand.

6.3. The grain size distribution of crushed specimens

The grain size distributions for quartz sand specimens after compression tests under 20, 40, 80, and 160 MPa are presented in Figure 6.6 (a). Table 6.2 summarizes the indices of each grain size distribution. As expected, the percentage of fine grains and the coefficient of uniformity increase as the stress level increases. Figure 6.6 (b) presents the GSD of dry and saturated quartz sand after crushing at 160MPa. The degree of grain breakage is slightly higher in dried quartz sand. This is likely due to the difference in the initial void ratio of the two specimens.

Based on the grain size distribution data, the Einav's breakage index for each stress can be evaluated using its definition [Eq. (2.3)]. This requires knowing the initial and ultimate grain size distribution and the Eq. (2.11) is used for the purpose. The value of fractal dimension is

fixed as 2.6 for ultimate grain size distribution and 1.2 for initial grain size distribution. With the specified ultimate and initial grain size distribution, the current grain size distribution ($F(x)$) can be found by adjusting *B* to best fit the current grain size distribution using Eq. (2.3). Figure 6.7 shows the calibrated grain size distribution and the calculated initial and ultimate grain size distribution for each crushing stress level. Figure 6.8 compiles the evolution of the GSD during isotropic compression process and the corresponding values of breakage *B*.

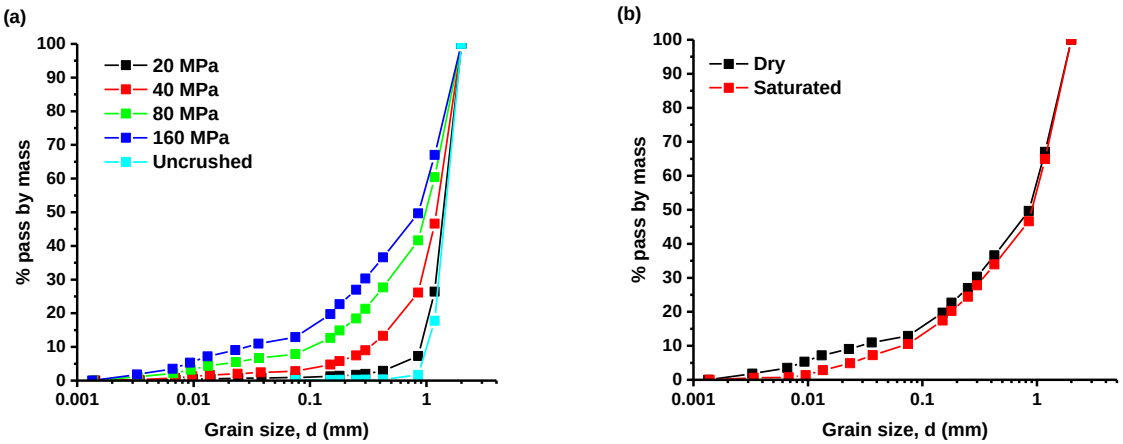

Figure 6.6: Grain size distribution of the quartz sand specimens after compression test under the different stress: (a) Dried quartz sand under 20, 40, 80, and 160 MPa; (b) Dried and saturated quartz sand under 160 MPa

Table 6.2: Parameters of grain size distribution

	Uncrushed	Dry 20 MPa	Dry 40 MPa	Dry 80 MPa	Dry 160 MPa	Saturated 160 MPa
D_{10}	1.07	0.92	0.33	0.11	0.03	0.07
D_{30}	1.32	1.22	0.93	0.5	0.3	0.34
D_{60}	1.61	1.56	1.38	1.17	1.15	1.08
Percent Fines (%)	0.15	0.91	2.79	7.86	12.88	10.88
C_u	1.50	1.7	4.18	10.64	38.33	15.43
C_c	0.99	0.96	0.53	0.51	0.38	0.65

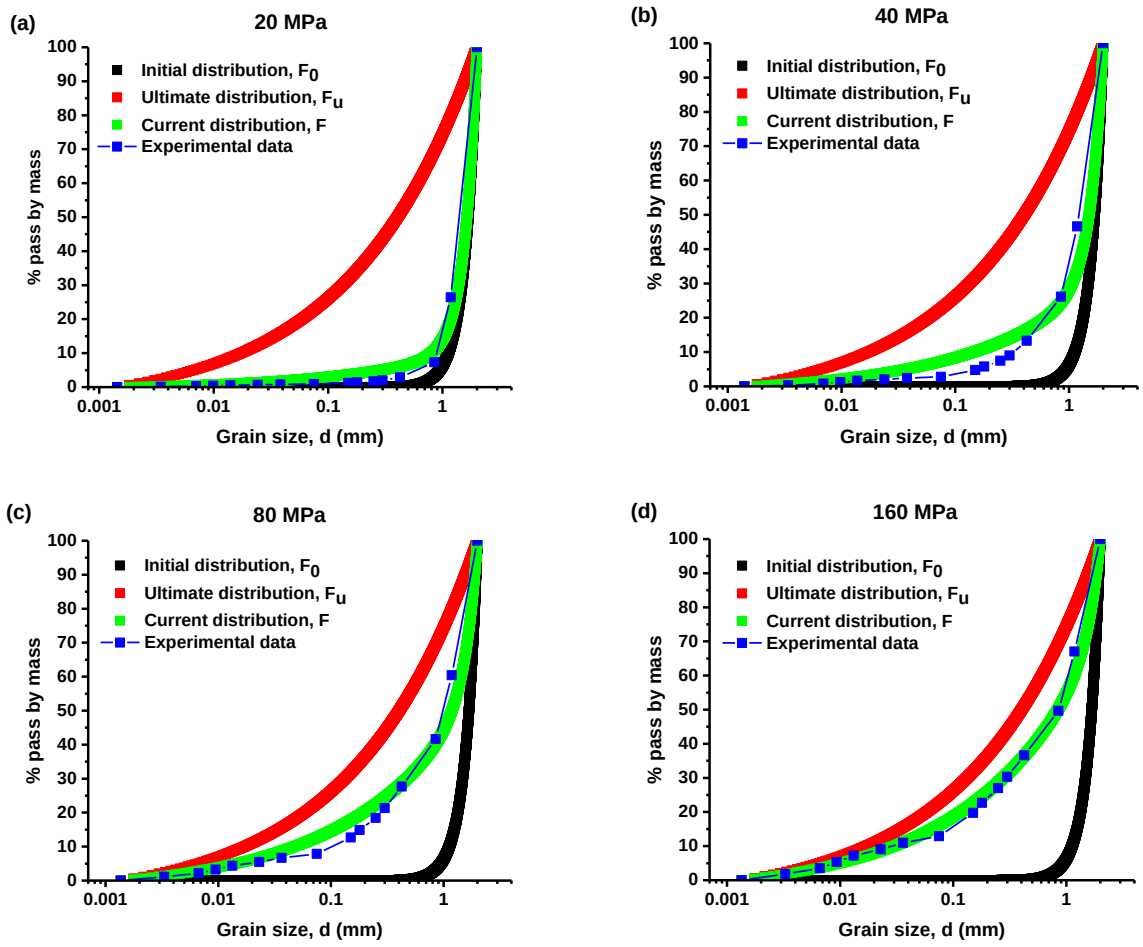

Figure 6.7: Initial, ultimate, and current grain size distribution for the specimens under different crushing stress: (a) 20 MPa; (b) 40 MPa; (c) 80 MPa; (d) 160 MPa

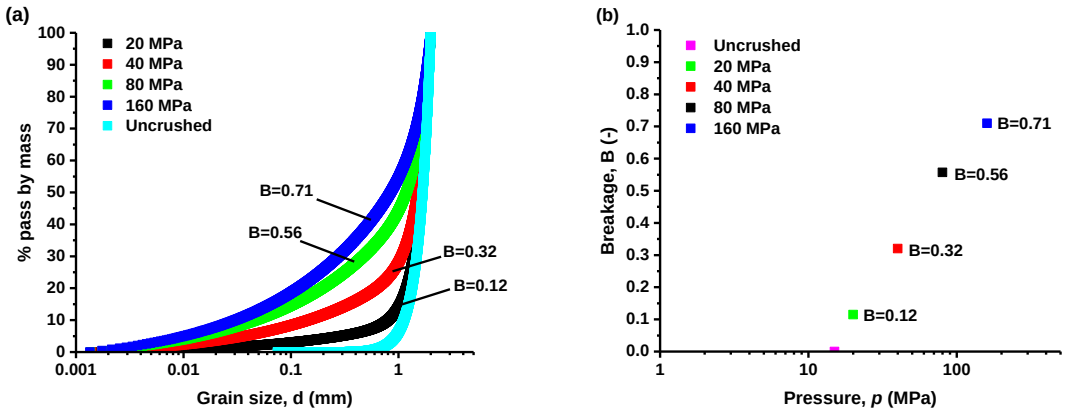

Figure 6.8: (a) GSD by calibration; (b) Breakage evolution curve by experiment

On the other hand, the shale sand specimens after compression are solidified as the finer grains generated by comminutions are adhered to the coarser grains. Such phenomenon is found for both saturated and dried shale sands as shown in Figure 6.9. For this reason, sieve analysis is not available for the shale sands.

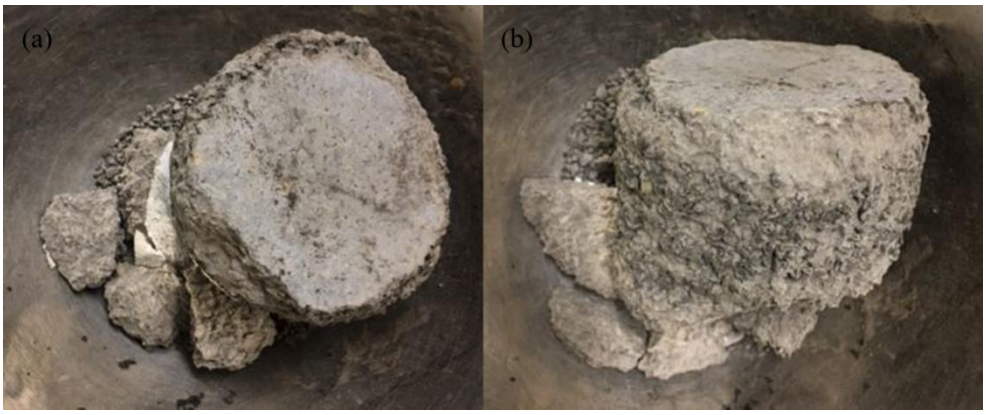

Figure 6.9: Picture of shale sand specimen after high pressure compression under 160 MPa: (a) Dried specimen; (b) Saturated specimen

CHAPTER 7: 1D BREAKAGE MODEL USING THE NEW BREAKAGE EVOLUTION LAW

A new breakage evolution law and the associated derivations are presented in this chapter. This breakage evolution law leads to two compression models by assuming either linear elasticity or pressure dependent elasticity model. These models are strictly developed for isotropic compression conditions where effect of deviatoric stress and shear strain on breakage are not considered. The efficiency of the models is tested against the data obtained from the previous chapter.

7.1. The modified breakage evolution law

The breakage evolution law for the original breakage mechanics is defined based on the breakage energy and *B*. It is expressed as

$$E_B = \frac{E_c}{(1-B)^2} \tag{7.1}$$

for isotropic compression. Recalling $E_B = -\frac{\partial \Psi}{\partial \mathrm{B}}$ which can be uniquely expressed in terms of *p*, this equation dictates a unique *p*-*B* relation for all granular materials, with E_c controlling the onset of breakage growth. The only parameter E_c apparently cannot account for the various shapes of such curve observed in different experiments (MIURA & O-HARA, 1979; Ovalle et al., 2013). To add additional flexibility of the breakage evolution law, we propose the following phenomenological curve, inspired by the well-known Van Genuchten SWRC equation.

$$E_B = \frac{E_c}{\left(1-B^{\left(1-\frac{1}{n}\right)}\right)^n} \tag{7.2}$$

where n is a shape factor. In the following, this equation will be subjected to parametric studies to demonstrate its features.

7.2. Parametric study

To convert Eq. (7.2) into a *p*-*B* relation, it is necessary to specify the Helmholtz free energy and hence the elastic model first. For a first-order assessment, let us consider linear elasticity in isotropic state:

$$\Psi = \frac{1}{2}(1 - \vartheta_M B)K{\varepsilon_v^e}^2 \tag{7.3}$$

one can obtain

$$p = \frac{\partial \Psi}{\partial \varepsilon_v^e} = (1 - \vartheta_M B)K\varepsilon_v^e \qquad \text{(cf. 2.21a)}$$

$$E_B = -\frac{\partial \Psi}{\partial \mathrm{B}} = \frac{1}{2}\vartheta_M K{\varepsilon_v^e}^2 \tag{7.4}$$

Substituting (2.21a) into (7.4), the breakage energy can be further expressed in terms of *p* as:

$$E_B = \frac{1}{2}\vartheta_M \frac{p^2}{(1-\vartheta_M B)^2 K} \tag{7.5}$$

Substituting Eq. (7.2) into (7.5) gives

$$p^2 = \frac{KE_c}{\vartheta_M}\frac{2(1-\vartheta_M B)^2}{\left(1-B^{\left(1-\frac{1}{n}\right)}\right)^n} \tag{7.6}$$

This is a *p*-*B* relation and can be plotted using MATLAB. Its performance is shown in Figure 7.1 using fixed values of ϑ_M = 0.52 and *K* = 700. As expected, the parameter *n* controls the slope of the breakage curve and E_c controls the onset of breakage growth. The experimental data is also plotted for comparison.

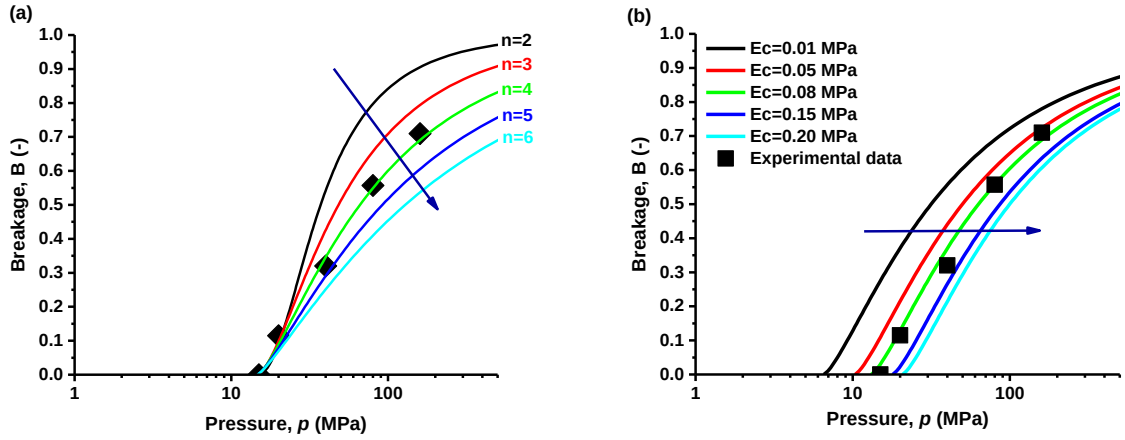

Figure 7.1: Parametric study: (a) shape factor n; (b) critical breakage energy E_c

7.3. A linear elastic 1D compression model based on the new breakage law

We propose the following yield criteria in true and dissipative stress space for 1D breakage models:

$$y = \frac{E_B}{E_c^*} - 1 = 0 \tag{7.7a}$$

$$\bar{y} = \left(\frac{\bar{E}_B}{\frac{\sqrt{E_B E_c^*}}{cos\omega}} \right)^2 + \left(\frac{\bar{p}}{\frac{p}{sin\omega\sqrt{\frac{E_c^*}{E_B}}}} \right)^2 - 1 = 0 \tag{7.7b}$$

By specifying

$$E_c^* = \frac{E_c}{(1-B)^2} \tag{7.8}$$

one recovers the original breakage model and

$$E_c^* = \frac{E_c}{\left(1-B^{\left(1-\frac{1}{n}\right)}\right)^n} \tag{7.9}$$

give the new breakage evolution Eq. (7.2). Now the focus is on deriving the incremental constitutive equation for stress-strain curves. The consistency condition can be expressed as:

$$dy = \frac{\partial y}{\partial p} dp + \frac{\partial y}{\partial B} dB \tag{7.10}$$

Applying chain rule:

$$dp = \frac{\partial p}{\partial \varepsilon^e} d\varepsilon_v^e + \frac{\partial p}{\partial B} dB = \frac{\partial p}{\partial \varepsilon_v^e} (d\varepsilon_v - d\varepsilon_v^p) + \frac{\partial p}{\partial B} dB \tag{7.11}$$

and substituting the flow rules

$$d\varepsilon_v^p = \lambda \frac{\partial \bar{y}}{\partial p}; dB = \lambda \frac{\partial \bar{y}}{\partial E_B} \tag{7.12}$$

, the expression of λ can be found:

$$\lambda = \frac{\frac{\partial y}{\partial p \partial \varepsilon_v^e} d\varepsilon_v}{\frac{\partial y}{\partial p \partial \varepsilon_v^e} \frac{\partial p}{\partial \bar{y}} - \left(\frac{\partial y}{\partial p \partial B} + \frac{\partial y}{\partial B}\right) \frac{\partial \bar{y}}{\partial E_B}} \tag{7.13}$$

For linear elasticity and the newly proposed breakage law, the following expressions of the derivatives can be obtained:

$$\frac{\partial p}{\partial \varepsilon_v^e} = (1 - \vartheta_M B) K; \ \frac{\partial p}{\partial B} = -\vartheta_M K \varepsilon_v^e \tag{7.14a}$$

$$\frac{\partial y}{\partial p} = \frac{1}{E c^*} \frac{\partial E_B}{\partial p}; \frac{\partial y}{\partial B} = \frac{1}{E_c^*} \frac{\partial E_B}{\partial B} - \frac{E_B}{E_c^{*2}} \frac{\partial E_c^*}{\partial B} \tag{7.14b}$$

$$\frac{\partial \bar{y}}{\partial p} = 2 \frac{E_B \sin^2 \omega}{p E_c^*}; \frac{\partial \bar{y}}{\partial E_B} = 2 \frac{\cos^2 \omega}{E_c^*} \tag{7.14c}$$

$$E_B = \frac{1}{2} \frac{\vartheta_M p^2}{(1 - \vartheta_M B)^2 K}; \frac{\partial E_B}{\partial p} = \frac{\vartheta_M p}{(1 - \vartheta_M B)^2 K}; \frac{\partial E_B}{\partial B} = \frac{\vartheta_M^2 p^2}{K (1 - \vartheta_M B)^3} \tag{7.14d}$$

$$\frac{\partial E_c^*}{\partial B} = \frac{E_c (n-1) \left(1 - B^{1 - \frac{1}{n}}\right)^{-n}}{B^{1/n} - B} \tag{7.14e}$$

Combining (7.14) to (7.13) and substituting (7.11) to (7.12), the plastic strain increment $d\varepsilon_v^p$ and the breakage increment dB can be expressed in terms of the total strain increment as:

$$d\varepsilon_v^p = \frac{\frac{2\vartheta_M E_B \sin^2\omega}{E_c^{*2}(1-\vartheta_M B)}}{\frac{2\vartheta_M E_B \sin^2\omega}{E_c^*(1-\vartheta_M B)} - \frac{2\cos^2\omega}{E_c^{*2}}\left(\frac{\vartheta_M^2 p}{K(1-\vartheta_M B)^3} - \frac{\vartheta_M^2 p\varepsilon_v^e}{(1-\vartheta_M B)^2} - \frac{E_B}{E_c^*}\left(\frac{E_c(n-1)\left(1-B^{1-\frac{1}{n}}\right)^{-n}}{B^{\frac{1}{n}-B}}\right)\right)} d\varepsilon_v \qquad (7.15a)$$

$$dB = \frac{\frac{2\vartheta_M p\cos^2\omega}{E_c^*(1-\vartheta_M)B}}{\frac{2\vartheta_M E_B \sin^2\omega}{E_c^*(1-\vartheta_M B)} - \frac{2\cos^2\omega}{E_c^{*2}}\left(\frac{\vartheta_M p}{K(1-\vartheta_M B)^3} - \frac{\vartheta_M^2 p\varepsilon_v^e}{(1-\vartheta_M B)^2} - \frac{E_B}{E_c^*}\left(\frac{E_c(n-1)\left(1-B^{1-\frac{1}{n}}\right)^{-n}}{B^{\frac{1}{n}-B}}\right)\right)} d\varepsilon_v \qquad (7.15b)$$

The above relations have been implemented and integrated numerically to obtain the $p - \varepsilon_v - B$ curves during an isotropic compression test. The new model is calibrated against the HPIC data of quartz sand. The determined parameters are presented in Table 7.1 and the results are presented in Figure 7.2. As shown in the figure, even though the breakage evolution curve is well captured based on calibration, the simple linear elastic model cannot represent well the pre-yielding behavior of granular soil. This is due to the pressure-dependent nature of their elastic responses. Linear elasticity model cannot reflect such dependency and thus drastically simplified the compressive behavior. The evolution of breakage with respect to total strain and the accumulation of elastic and plastic strains during loading shows qualitatively reasonable trends. As expected, for this coupled plastic-breakage model, plastic strain starts to develop after the point of clastic yielding.

For further investigation of the model performance, a parametric study is conducted as shown in the Figure 7.3. The compression curves with three different values of E_c and K are plotted, keeping all the other parameter fixed. It is observed that E_c controls the yielding stress

[Figure 7.3 (a)] and the increasing stiffness K enhances both yielding stress and the elastic stiffness. However, the adjustment of these parameters cannot fix the poor performance of the model at the pre-yielding regime. Thus, the linear elasticity is not suitable for describing granular materials.

Table 7.1 Parameters for best-matched prediction with linear elasticity model

Parameters for grading indices ϑ_M					Mechanical parameters			Shape factor
β	α	D_m	D_M	ϑ_M	K	E_c (MPa)	ω	n
1.18	2.6	0.075	2.0	0.5229	320	0.15	70	4.5

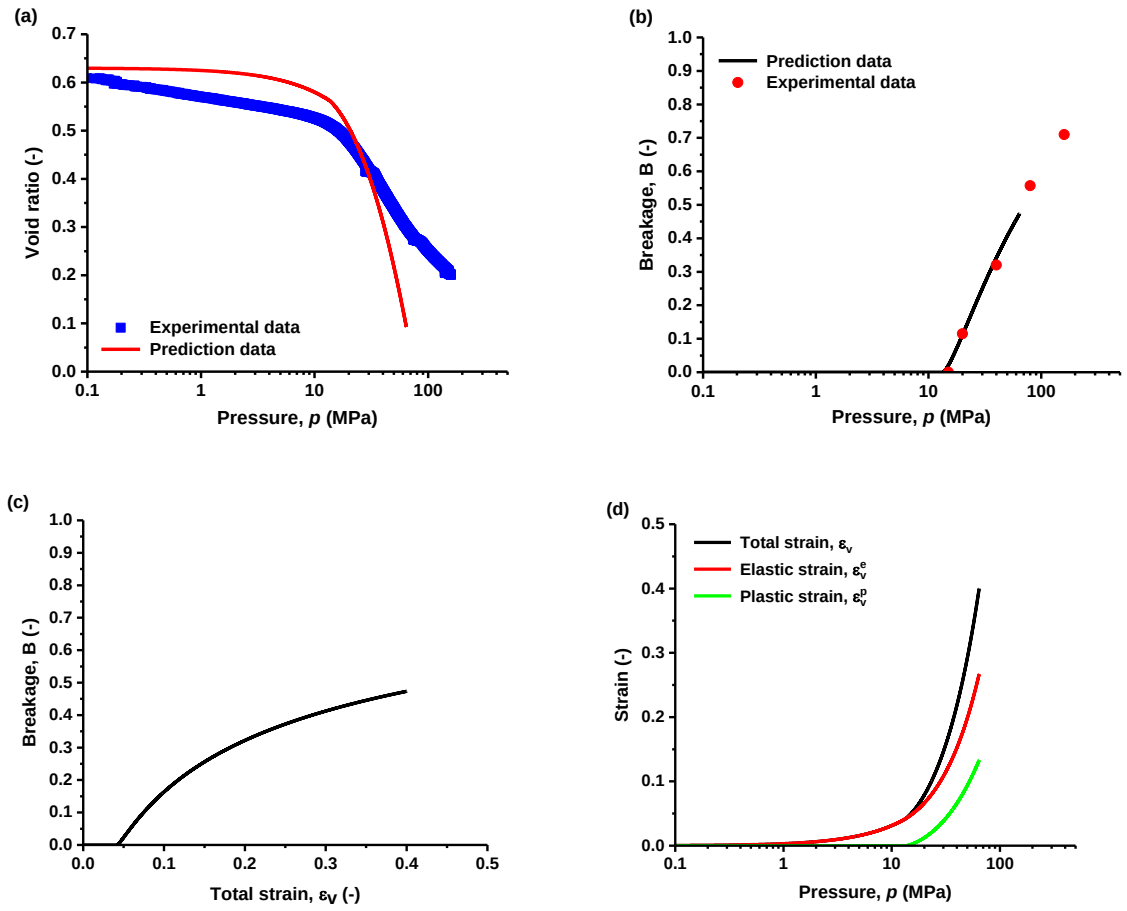

Figure 7.2: Prediction by linear elasticity model: (a) Compression curve; (b) Breakage evolution curve; (c) Total strain – Breakage degree; (d) Stress – strain (Total, Elastic and plastic strain)

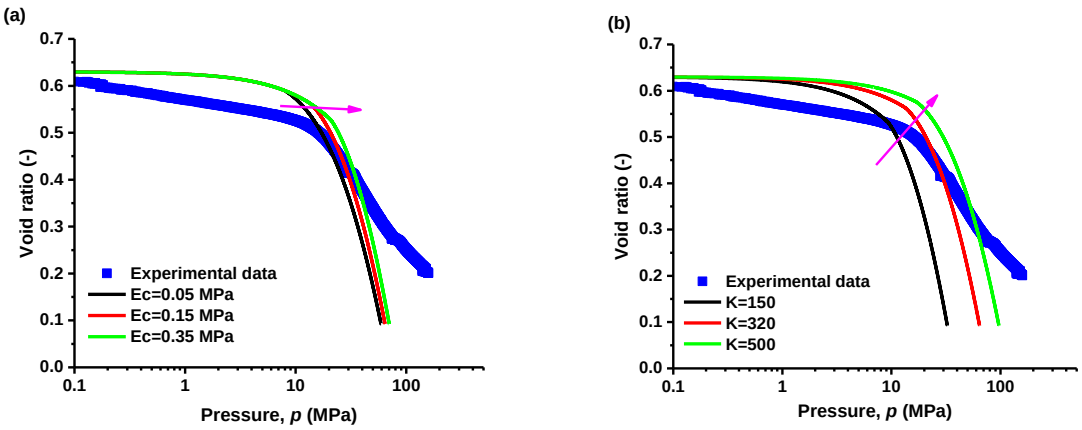

Figure 7.3: Parametric study of linear elasticity model:(a) for critical breakage energy; (b) for stiffness

7.4. Breakage evolution law in pressure-dependent (PD) elasticity

For more apparent description of the compressive behavior of granular materials, another breakage model based on pressure dependent elasticity (Einav and Puzrin, 2004) is developed. The model is, hereafter, called as PD model. Recalling [Eq. 2.23 (a)] $p = (1 - \vartheta_M B) p_r \bar{K} A^{\frac{1}{m-1}} \left(\frac{1}{\bar{K}} + \frac{3}{2} m \bar{G} A^{-2} \varepsilon_s^{e\,2} \right)$ and considering only isotropic case, it can be expressed as:

$$p = (1 - \vartheta_M B) p_r A^{\frac{1}{m-1}} \tag{7.16}$$

recalling $A = \bar{K}(1 - m)\varepsilon_v^e + 1$, p_r is a reference pressure, $m = 0.5$ for typic granular material, $\bar{K}$ is a dimensionless elastic constant. The associated derivatives can be expressed as:

$$\frac{\partial p}{\partial \varepsilon_v^e} = (1 - \vartheta_M B) p_r A^{\frac{m}{1-m}} \bar{K} \tag{7.17a}$$

$$\frac{\partial p}{\partial B} = -\vartheta_M p_r A^{\frac{1}{1-m}} \tag{7.17b}$$

The breakage energy and its derivatives for PD elasticity can be derived as:

$$E_B = \vartheta_M \frac{p_r}{\bar{K}(2-m)} A^{\frac{2-m}{1-m}} \tag{7.18a}$$

$$\frac{\partial E_B}{\partial p} = \vartheta_M \frac{p_r}{\overline{K}} \left(\frac{1}{p_r(1-\vartheta_M B)} \right)^{2-m} p^{1-m} \tag{7.18b}$$

$$\frac{\partial E_B}{\partial B} = \vartheta_M^2 \frac{p_r}{\overline{K}} \left(\frac{p}{p_r} \right)^{2-m} \left(\frac{1}{1-\vartheta_M B} \right)^{3-m} \tag{7.18c}$$

Substituting these new terms in the expression of λ, one can derive the incremental flow rules in the case of PD elasticity:

$$d\varepsilon_v^p = \frac{2\frac{\vartheta_M^2 p_r^2 E_B \sin^2\omega}{E_c^{*2}\overline{K}} \frac{1}{p} A^{\frac{1}{1-m}}}{\frac{\vartheta_M^2 p_r E_B sin^2\omega}{E_c^{*2}\overline{K}} \frac{1}{p} A^{\frac{1}{1-m}} \left(\frac{p'}{p_r(1-\vartheta_M B)} \right) + \frac{2\cos^2\omega}{E_c^*} \left[\frac{\vartheta_M^2 p_r}{E_c^*\overline{K}} \left(\frac{p}{p_r} \right)^{2-m} \left(\frac{1}{1-\vartheta_M B} \right)^{3-m} - \frac{\vartheta_M K \varepsilon_v^e p_r}{E_c^* \overline{K}} \left(\frac{p}{p_r} \right)^{2-m} \left(\frac{1}{1-\vartheta_M B} \right)^{3-m} - \frac{E_B}{E_c^{*2}} \left(\frac{E_C(n-1)\left(1-B^{1-\frac{1}{n}}\right)^{-n}}{B^{\frac{1}{n}}-B} \right) \right]} d\varepsilon_v \tag{7.19a}$$

$$d\varepsilon_v^p = \frac{2\frac{\vartheta_M^2 p_r^2}{E_c^{*2}\overline{K}} \frac{\cos^2\omega}{E_c^*} A^{\frac{1}{1-m}}}{\frac{\vartheta_M^2 p_r E_B sin^2\omega}{E_c^{*2}\overline{K}} \frac{1}{p} A^{\frac{1}{1-m}} \left(\frac{p}{p_r(1-\vartheta_M B)} \right) + \frac{2\cos^2\omega}{E_c^*} \left[\frac{\vartheta_M^2 p_r}{E_c^*\overline{K}} \left(\frac{p'}{p_r} \right)^{2-m} \left(\frac{1}{1-\vartheta_M B} \right)^{3-m} - \frac{\vartheta_M K \varepsilon_v^e p_r}{E_c^* \overline{K}} \left(\frac{p}{p_r} \right)^{2-m} \left(\frac{1}{1-\vartheta_M B} \right)^{3-m} - \frac{E_B}{E_c^{*2}} \left(\frac{E_C(n-1)\left(1-B^{1-\frac{1}{n}}\right)^{-n}}{B^{\frac{1}{n}}-B} \right) \right]} d\varepsilon_v \tag{7.19b}$$

The model is again implemented in MATLAB and calibrated against the quartz sand data. The determined parameters are shown in Table 7.2 and the results are presented in Figure 7.4. The prediction satisfactorily captures the experimental data. The yielding and hardening are well-captured and the pre-yielding response is much better represented than the linear elastic model. It is also noted that the model cannot capture the reduced compressibility at elevated stress levels due to void closure effect. Such effect can in principle be incorporated by introducing pressure-dependent coupling angle ω. This non-trivial task will be pursued in the future studies. Figures 7.4 (b), (c) and (d) show similar traits as the ones for linear elasticity. The breakage data is again well represented by the newly proposed breakage law.

Table 7.2: Parameters for best-matched prediction with PD model

Parameters for grading indices ϑ_M					Mechanical parameters					Shape factor
β	α	D_m	D_M	ϑ_M	$\bar{K}$	E_c (MPa)	ω	p_r (MPa)	m	n
2.6	1.18	0.075	2.0	0.5229	3500	0.15	70	0.001	0.5	4.5

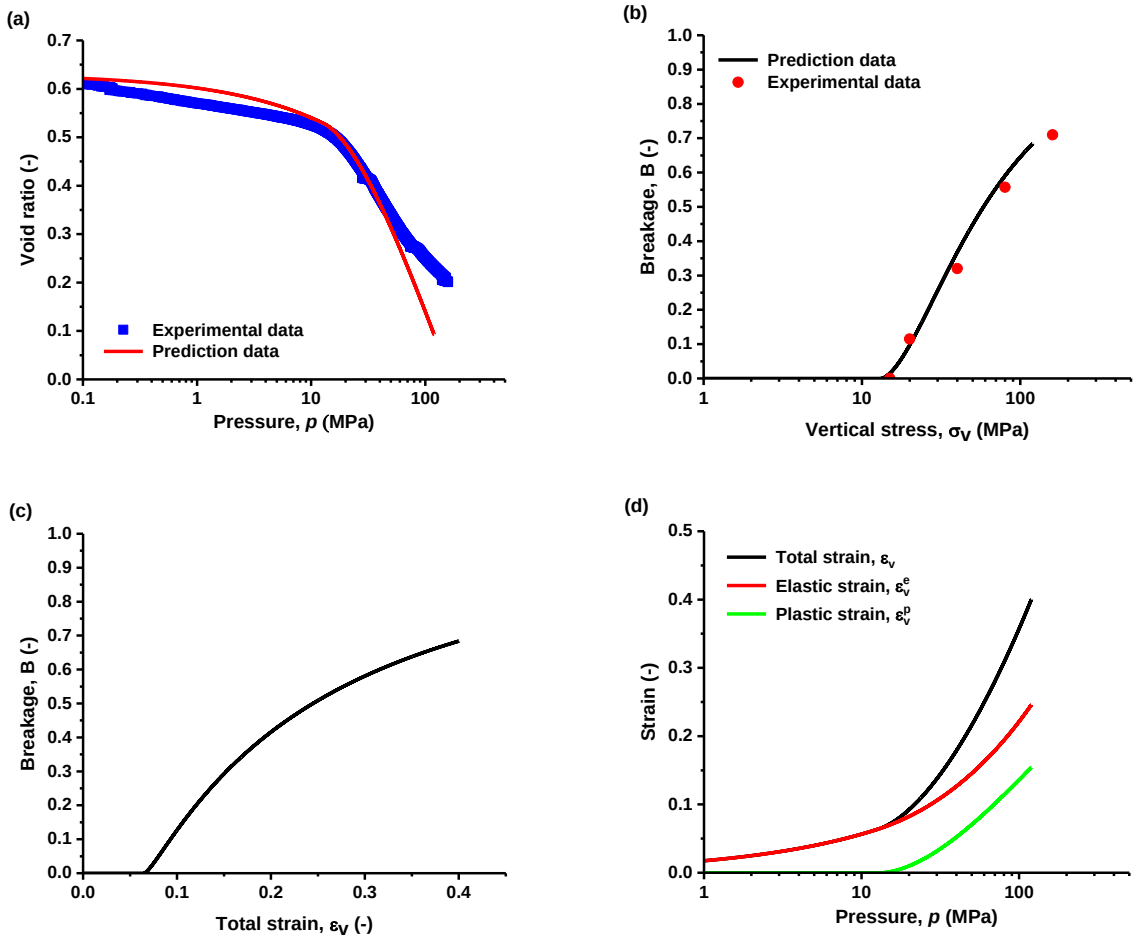

Figure 7.4: Prediction results by PD model: (a) compression curve; (b) Breakage evolution curve; (c) Total strain – Breakage degree; (d) Stress – strain (Total, Elastic and plastic strain)

CHAPTER 8: CONCLUSION

The alternation of hydromechanical properties of granular materials during grain crushing is studied in the framework of Unsaturated Breakage Mechanics. The model performance is examined by experimental data from four granular materials distinguished by initial grain size and shapes. The predicted results by the UBM largely agrees with experimental data, which is consistent with the previous findings. It is predicted that the hydromechanical coupling effect is not significant on the tested granular materials due to their low water retention capability and high crushing resistance. One limitation of the UBM model is identified: it cannot capture the apparent yielding caused by particle rearrangement and asperity breakage prior to the massive bulk crushing.

The High Pressure Isotropic Compression device is used in this study with an initial motivation to capture the co-evolution of grain crushing, soil water retention and compression simultaneously. After fully examining the device configuration, benchmarking the test results with other devices, and troubleshooting the data acquisition system, it is concluded that the HPIC device is not suitable for suction controlled experiments. For this reason, the device is re-configured for mechanical testing only. Protocols for sample preparation for high pressure grain crushing tests are developed.

The compression tests are conducted in drainage condition for dried and saturated quartz sand under 20, 40, 80, and 160 MPa and shale sand under 160 MPa. It is found that the difference on the compression response is negligible for dry and saturated quartz sands, while significant for shale sands. Specifically, saturated shale sand exhibits higher compressibility, lower yielding stress and earlier void closure as compared to the dry one. Significant stress relaxation is observed in the saturated shale sand test due to the same water weakening effect. In

conclusion, the interplay between hydraulic and mechanical properties of the granular assemblies is strongly affected by the mineralogy of the constituting grains.

The particle size analysis is conducted for quartz sand specimens after compression to different stress levels. The produced grain size distributions show a monotonic increasing trend between stress and degree of crushing. The effect of saturation is negligible for quartz sand in terms of the grain size distributions. A new breakage law is developed to capture the observed GSDs. This law is used in combination with linear elasticity and pressure dependent elasticity to formulate new 1D compression models. Both models well capture the evolution of GSD during isotropic loading. The linear elasticity model oversimplifies the elastic response of granular soils while the pressure dependent elasticity well captures the entire compression curve.

Future works will be focusing on testing a variety of granular soils with varying initial GSDs and angularities to document a database for the development of constitutive models for crushable geomaterials. The potential for the HPIC device for suction-controlled testing will be further explored. The proposed 1D breakage law will be generalized to triaxial space as part of a critical-state breakage-mechanics theory.

REFERENCE

Alonso, E., Gens, A. & Josa, A. (1990). A constitutive model for partially saturated soils. *Geotechnique* **40(3)**:405-430.

Andò, E., Viggiani, G., Hall, S. A., & Desrues, J. (2013). Experimental micro-mechanics of granular media studied by x-ray tomography: recent results and challenges. *Géotechnique Letters* **3(3)**:142–146.

Arya, L. M., & Paris, J. F. (1981). A Physicoempirical Model to Predict the Soil Moisture Characteristic from Particle-Size Distribution and Bulk Density Data1. *Soil Science Society of America Journal* **45(6)**:1023-1030.

Aubertin, M., Mbonimpa, M., Bussière, B., & Chapuis, R. P. (2003). A model to predict the water retention curve from basic geotechnical properties. *Canadian Geotechnical Journal* **40(6)**:1104–1122.

Ben-Nun, O., & Einav, I. (2010). The role of self-organization during confined comminution of granular materials. *Philosophical Transactions. Series A, Mathematical, Physical, and Engineering Sciences* **368(1910)**:231–247

Botts, M. (1998). Effects of slaking on the strength of clay shales: A critical state approach. In *the Geotechnics of Hard Soils--soft Rocks: Proceedings of the Second International Symposium on Hard Soils, Soft Rocks: Naples, Italy, 12-14 October 1998*. Taylor & Francis US, vol. 1, pp. 447

Bremer, J., Mibeck, B., Huffman, B. L., Gorecki, C. D., Sorensen, J. A., SSchmidt, D. D. & Harju, J. A. (2010). Mechanical and geochemical assessment of hydraulic fracturing proppants exposed to carbon dioxide and hydrogen sulfide. In *Canadian Unconventional Resources and International Petroleum Conference.* Society of Petroleum Engineers

Buscarnera, G., & EINAV, I. (2012). The yielding of brittle unsaturated granular soils. *Géotechnique* **62(2)**:147–160.

Buscarnera, G., & Nova, R. (2009) An elastoplastic strainhardening model for soil allowing for hydraulic bonding-debonding effects. *International Journal for Numerical and Analytical Methods in Geomechanics* **33(8)**:1055–1086.

Cil, M. B., & Alshibli, K. A. (2014). 3D evolution of sand fracture under 1D compression. *Geotechnique* **64(5)**:351-364.

Claybourn, A. F. (2007). Failure of Drilled Piers in Denver Due to Formation of Softened Claystone. In *Contemporary Issues In Deep Foundations* (pp. 1–11).

Colliat-Dangus, J.L, Desrues, J., & Foray, P. (1988). Triaxial Testing of Granular Soil Under Elevated Cell Pressure. In *Advanced Triaxial Testing of Soil and Rock*, ASTM (pp. 290-290–21).

Coop, M. R., Sorensen, K. K., Bodas Freitas, T., & Georgoutsos, G. (2004). Particle breakage during shearing of a carbonate sand. *Géotechnique* **54(3)**:157–163.

Einav, I. (2007). Breakage mechanics—Part I: Theory. *Journal of the Mechanics and Physics of Solids* **55(6):**1274–1297.

Einav, I., & Puzrin, A. M. (2004). Pressure-Dependent Elasticity and Energy Conservation in Elastoplastic Models for Soils. *Journal of Geotechnical and Geoenvironmental Engineering* **130(1):**81–92.

Esna Ashari, S., Das, A., & Buscarnera, G. (2018). Model-Based Assessment of the Effect of Surface Area Growth on the Permeability of Granular Rocks. *Journal of Engineering Mechanics* **144(5)**: 04018023.

Fredlund, D. G. & Rahardjo, H. (1993). *Soil mechanics for unsaturated soils*. New York, NY: John Wiley & Sons.

Gallipoli, D., Gens, A., Sharma, R., & Vaunat, J. (2003). An elasto-plastic model for unsaturated soil incorporating the effects of suction and degree of saturation on mechanical behaviour. *Géotechnique, 2003* **53(2):***123-136*.

Gao, S., Zhang, Y. Da, Sonta, A., & Buscarnera, G. (2016). Evolution of the Water Retention Characteristics of Granular Materials Subjected to Grain Crushing. *Journal of Geotechnical and Geoenvironmental Engineering* **142(9):**6016006.

Gaurav, A., Dao, E. K., & Mohanty, K. K. (2012). Evaluation of ultra-light-weight proppants for shale fracturing. *Journal of Petroleum Science and Engineering* **92**:82–88.

GENS, A. (2010). Soil–environment interactions in geotechnical engineering. *Géotechnique* **60(1)**: 3–74.

Ghosh, S., Rai, C.S., Sondergeld, C. H. & Larese, R. E. (2014). Experimental Investigation of Proppant Diagenesis. In *SPE/CUSR Unconventional Resources Conference-Canada.* Society of Petroleum Engineers.

Golightly, C. R. (1989). Engineering properties of carbonate sands : the geological origins, classification, engineering, shear and triaxial stress path properties of four carbonate sands. The analysis of the transfer function for pile skin friction. Ph.D. dissertation, Univ. Bradford, West Yorkshire

Hall, S., Bornert, M., Desrues, J., Pannier, Y., Lenori, N., Viggiani, G., & Besuelle, P. (2010). Discrete and continuum analysis of localised deformation in sand using X-ray ìCT and volumetric digital image correlation. *Geotechnique* **60(5):**315–322.

Ham, A., Wang, J. & Stammer, J. G. (2011) Relationships between particle shape characteristics and macroscopic damping in dry sands. *Journal of Geotechnical and Geoenvironmental Engineering* **138(8)**:1002-1011.

Hardin, B. O. (1985). Crushing of Soil Particles. *Journal of Geotechnical Engineering* **111(10):** 1177–1192.

Hendron, A. (1963). The behavior of sand in one-dimensional compreession. Ph.D. dissertation, Univ. of Illinois at Urbana-Champaign, Champaign, IL.

Houlsby, G. T. & Puzrin, A. M. (2007) *Principles of hyperplasticity: an approach to plasticity theory based on thermodynamic principles.* Springer Science & Business Media.

Indraratna, B., Lackenby, J., & Christie, D. (2005). Effect of confining pressure on the degradation of ballast under cyclic loading. *Géotechnique* **55(4):**325–328.

Indraratna, B., Nimbalkar, S. S., & Tennakoon, N. (2010). The Behaviour of Ballasted Track Foundations: Track Drainage and Geosynthetic Reinforcement. In *GeoFlorida 2010* (pp. 2378–2387). Reston, VA: American Society of Civil Engineers.

Ingraham, M., Bauer, S., Quintana, E., Bolintineau, D., Rao, R. & Lechman, J. (2015). Proppant and host rock deformation in fractured shale flow through experiments. In *49th US Rock Mechanics/Geomechanics Symposium.* American Rock Mechanics Association.

Kuwajima, K., Hyodo, M., & Hyde, A. F. (2009). Pile Bearing Capacity Factors and Soil Crushabiity. *Journal of Geotechnical and Geoenvironmental Engineering* **135(7):**901–913.

Lackenby, J., Indraratna, B., McDowell, G., & Christie, D. (2007). Effect of confining pressure on ballast degradation and deformation under cyclic triaxial loading. *Géotechnique* **57(6):** 527–536.

Lade, P. V., Yamamuro, J. A., & Bopp, P. A. (1996). Significance of Particle Crushing in Granular Materials. *Journal of Geotechnical Engineering* **122(4):**309–316.

Lee, K. L., & Farhoomand, I. (1967). Compressibility And Crushing Of Granular Soil In Anisotropic Triaxial Compression. *Canadian Geotechnical Journal* **4(1)**:68–86.

Lee, K. L., & Seed, H. B. (1967). Drained Strength Characteristics of Sands. *Journal of Soil Mechanics & Foundations Div*. **93(SM6)**:117-141

Marsal, R. J. (1973). Mechanical Properties of Rockfill. *Casagrand Volume, Wiley, New York*:109-200

Mcdowell, G. R., & Arireche, O. H. (2002). Discrete element modelling of yielding and normal compression of sand. *Geotechnique* **52(4)**:299-304

McDowell, G. R., & Bolton, M. D. (2000). Effect of particle size distribution on pile tip resistance in calcareous sand in the geotechnical centrifuge. *Granular Matter **2*(4)**:179–187.

Miura, N., & O-hara, S. (1979). Particle-crushing of a decomposed granite soil under shear stresses. *Soils and Foundations* **19(3):**1–14.

Mun, W., & McCartney, J. S. (2015). Compression mechanisms of unsaturated clay under high stresses. *Canadian Geotechnical Journal* **52(12):**2099–2112.

Mun, W., & McCartney, J. S. (2017). Roles of Particle Breakage and Drainage in the Isotropic Compression of Sand to High Pressures. *Journal of Geotechnical and Geoenvironmental Engineering **143*(10)**:4017071.

Nakata, Y., Kato, Y., Hyodo, M., Hyde, A. F. L., & Murata, H. (2001). One-Dimensional Compression Behaviour of Unuformly Granded Sand Related to Single Particle Crushing Strength. *Soils and Foundations* **41(2)**:39–51.

Oldecop, L. A., & Alonso, E. E. (2001). A model for rockfill compressibility. *Géotechnique* **51(2)**:127–139.

Oldecop, L. A., & Alonso, E. E. (2007). Theoretical investigation of the time-dependent behaviour of rockfill. *Géotechnique* **57(3)**:289–301.

Ovalle, C., Dano, C., & Hicher, P.-Y. (2013). Experimental Data Highlighting the Role of Surface Fracture Energy in Quasi-Static Confined Comminution. *International Journal of Fracture* **182(1)**:123–130.

Ovalle, C., Frossard, E., Dano, C., Hu, W., Maiolino, S., & Hicher, P.-Y. (2014). The effect of size on the strength of coarse rock aggregates and large rockfill samples through experimental data. *Acta Mechanica* **225(8)**: 2199–2216.

Pestana, J. M., & Whittle, A. J. (1995). Compression model for cohesionless soils. *Geotechnique* **45(4)**:611–631.

Raysoni, N. & Weaver, J. (2013). Long-term hydrothermal proppant performance. *SPE Production & Operations* **28(04)**:414-426.

Sadrekarimi, A., & Olson, S. M. (2010). Particle damage observed in ring shear tests on sands. *Canadian Geotechnical Journal* **47(5)**:497–515.

Sammis, C., King, G., & Biegel, R. (1987). The kinematics of gouge deformation. *Pure and Applied Geophysics PAGEOPH* **125(5)**:777–812.

Sohn, C., Zhang, Y. D., Cil, M., & Buscarnera, G. (2017). Experimental assessment of continuum breakage models accounting for mechanical interactions at particle contacts. *Granular Matter* **19(4)**:67.

Sun, D., Sheng, D., & Sloan, S. W. (2007). Elastoplastic modelling of hydraulic and stress–strain behaviour of unsaturated soils. *Mechanics of Materials* **39(3)**:212–221.

Tapias, M., Alonso, E. & Gili, J. (2015) A particle model for rockfill behaviour. *Géotechnique* **65(12)**:975-994.

Tsoungui, O., Vallet, D., & Charmet, J.-C. (1999). Numerical model of crushing of grains inside two-dimensional granular materials. *Powder Technology* **105(1)**:190–198.

Vesic, A. S., & Clough, G. W. (1968). BEHAVIOR OF GRANULAR MATERIALS UNDER HIGH STRESSES. *Journal of Soil Mechanics & Foundations Div*. **94(SM3)**:661-688

Wang, G., Sassa, K., & Fukuoka, H. (2003). Downslope volume enlargement of a debris slide–debris flow in the 1999 Hiroshima, Japan, rainstorm. *Engineering Geology* **69(3)**:309–330.

Wheeler, S. J., Sharma, R. S., & Buisson, M. S. R. (2003). Coupling of hydraulic hysteresis and stress–strain behaviour in unsaturated soils. *Géotechnique* **53(1)**:41–54.

Wheeler, S. J., & Sivakumar, V. (1995). An elasto-plastic critical state framework for unsaturated soil. *Géotechnique* **45(1)**:35–53.

Yang, Z. X., Ja Rdin, R. J., Zh, B. T., Oray, P. F., & Tsuha, C. H. C. (2010). Sand grain crushing and interface shearing during displacement pile installation in sand, *Geotechnique*

60(6):469-482.

Zhang, Y. D., & Buscarnera, G. (2014). Grainsize dependence of clastic yielding in unsaturated granular soils. *Granular Matter* **16(4)**:469–483.

Zhang, Y. D., & Buscarnera, G. (2015). Prediction of breakage-induced couplings in unsaturated granular soils. *Géotechnique* **65(2)**:135–140.

Zhang, Y. D., Buscarnera, G., & Einav, I. (2016). Grain size dependence of yielding in granular soils interpreted using fracture mechanics, breakage mechanics and Weibull statistics. *Géotechnique* **66(2)**:149–160.

Zhang, Y. D., Park, J. S., Gao, S., Sonta, A., Horin, B. & Buscarnera, G. (2017). Effect of grain crushing and grain size on the evolution of water retention curves. *Geotechnical Special Publication*. Paper presented at PanAm-UNSAT 2017, Dallas, TX.